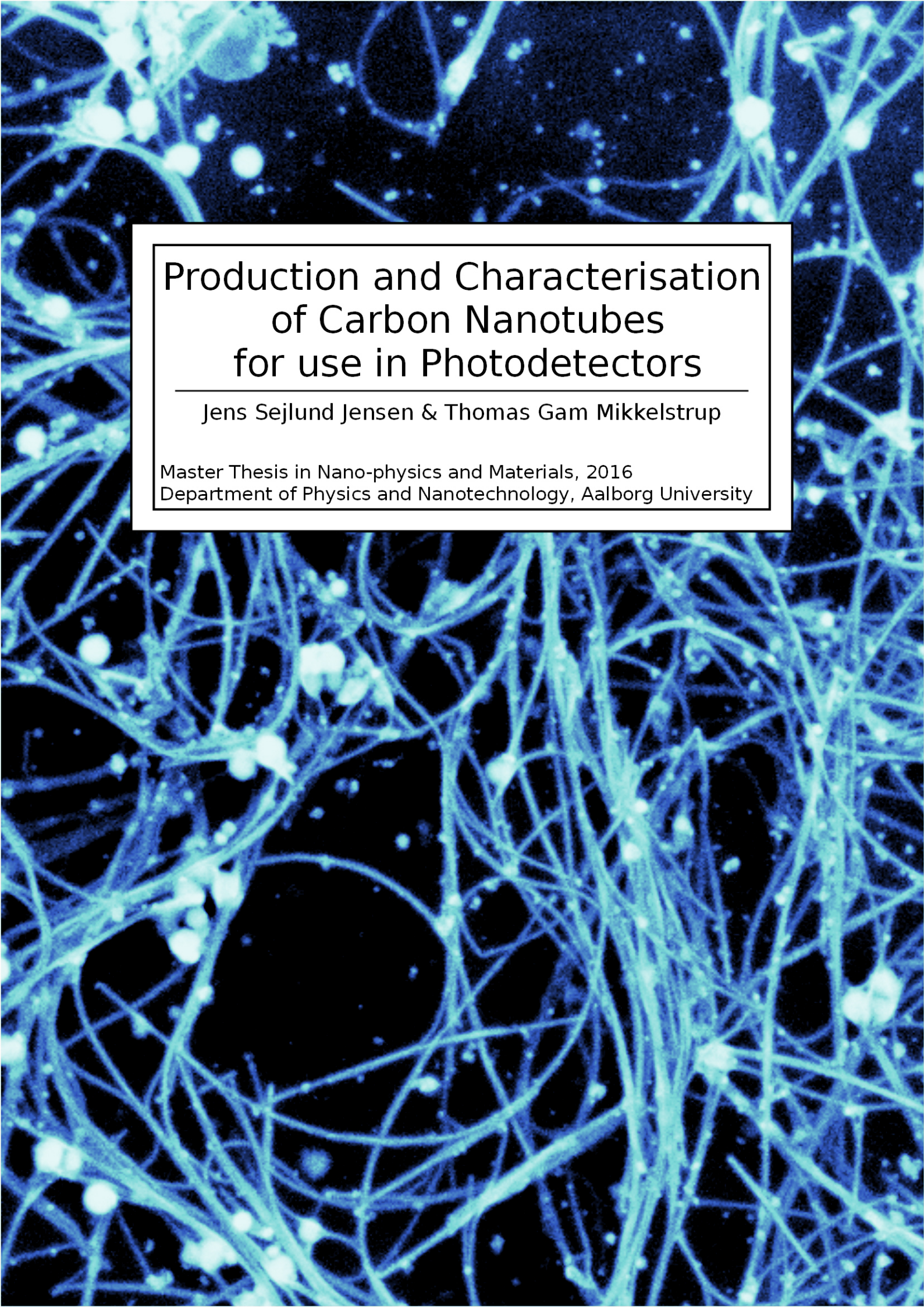

Production and Characterisation of Carbon Nanotubes for use in Photodetectors

Jens Sejlund Jensen & Thomas Gam Mikkelstrup

Master Thesis in Nano-physics and Materials, 2016
Department of Physics and Nanotechnology, Aalborg University

AALBORG UNIVERSITY
STUDENT REPORT

Department of Physics and Nanotechnology
The Faculty of Engineering and Science
Aalborg University
Skjernvej 4A
DK-9220 Aalborg Ø, Denmark
Telephone: 9940 9215
Fax: 9940 9235
www.nano.aau.dk

Title: Production and characterisation of carbon nanotubes for use in photodetectors
Project period: September 2015 to June 2016

Authors:

Jens Sejlund Jensen

Thomas Gam Mikkelstrup

Supervisor:
Kjeld Pedersen

Copies: 4
Page count: 101
Completed: 14th of June, 2016

Abstract:

This project examines the most common methods of growing carbon nanotubes, with focus on their use in photodetectors. It mainly deals with the chemical vapour deposition method of nanotube growth, but other methods are described as well. The theory behind the geometry and band structure of carbon nanotubes is discussed, along with the basic theory behind metal-semiconductor-metal photodiodes. The photocurrent mechanisms for carbon nanotubes is investigated. Furthermore the theory behind characterization of carbon nanotubes using Raman spectroscopy is also included.
Carbon nanotubes are grown through chemical vapour deposition and are then characterised using scanning electron microscopy, atomic force microscopy, absorbance spectroscopy and Raman spectroscopy. While nanotubes were produced during experiments, no samples were ever of high enough quality for use in photodetectors, so samples were produced with nanotubes bought from mk-NANO instead. The bought nanotubes were exfoliated and deposited on various samples and electrical contacts were created with a direct-write UV-lithography system, followed by current-voltage characteristics and photocurrent measurements.

Dansk abstract

Dette projekt inkluderer nogle af de mest bruge metoder til at gro kulstof nanorør, med fokus på deres brug i fotodetektorer. Der arbejdes hovedsageligt med nanorør groet via chemical vapour deposition, men andre metoder bliver også beskrevet. Teorien bag nanorørenes geometri og elektroniske båndstruktur fremlægges sammen med den basale teori bag metal-halvleder-metal fotodetektorer. Fotostrømsmekanismerne for kulstof nanorør gennemgås. Teorien bag karakterisering af nanorør via Raman spektroskopi er også inkluderet.

Kulstof nanorør blev groet via chemical vapour deposition og blev karakteriseret med skanning elektron mikroskopi, atomar kraft mikroskopi, absorbans spektroskopi og Raman spektroskopi. Selvom nanorør blev produceret gennem forsøgene i denne rapport, var ingen af dem af god nok kvalitet til at blive brugt til fotodetektorer. Disse blev derfor produceret via nanorør indkøbt fra mkNANO i stedet. De købte nanorør blev separeret og deponeret på forskellige prøver, og elektriske kontakter blev lavet med et direct-write UV-litografi system. De blev efterfølgende undersøgt med strøm-spænding's kurver og fotostrøms målinger.

Preface

After a short introduction to the properties and applications of carbon nanotubes, the thesis contains a chapter on geometry of carbon nanotubes leading to a tight-binding model. Then the basics of photodetectors are covered and a more detailed analysis of carbon nanotube based photodetectors is included. The experiments consist of a unique method to grow carbon nanotubes at specific locations, debundeling of purchased carbon nanotubes and two different configurations of photodetectors. Raman spectroscopy, an electron microscope, optical microscope, atomic force microscope and a four point probe system have all been used to characterise the carbon nanotubes and document their effectiveness.

Citations in this report are made using the American Institute of Physics (AIP) style, with references numbered in order of appearance and listed in this order in the bibliography. A reference placed before a full stop refers to that sentence alone, whereas a reference placed after a full stop refers to the entire paragraph. Figures and formulas are numbered according to the chapter in which they appear, with the first figure in chapter two being called 2.1, the second 2.2 etc. All graphs and images are referred to as figures, and figures without direct citation are the work of the authors. Vectors are denoted as $\vec{A}$ and matrices are denoted as $\overleftrightarrow{A}$. Complex conjugation is denoted by the superscript *.

The front page image is a mat of carbon nanotubes incapsulated by Triton X-100 on a silicon wafer taken with an electron microscope and recoloured.

Carbon nanotube, nanotube and single-walled carbon nanotube are used interchangeably. If it is multi-walled carbon nanotubes or another type of nanotubes it is stated explicitly.

The authors wish to thank Kim Houtved Jensen, Deyong Wang, Peter Kjær Kristensen and Vladimir Popok from the Department of Physics and Nanotechnology at Aalborg University for their help with the experimental part and characterisation.

Aalborg University, 14-06-2016.

Contents

1 Introduction

Twenty five years ago a scientist named Ijima attempted to grow fullerenes through the use of arc-discharge [1]. After examining the carbon dust he found traces of small cylindrical carbon structures with dimensions on the nanoscale. These "carbon nanotubes" have since been a promising area of study up until today. This is mostly due to not only their mechanical stability and strength [2], but also due to their versatile electrical abilities [3, 4] and highly variable band gap. Other properties include high thermal conductivity [5], optoelectronic properties [6], and superior chemical stability [7].

All of this combined have caused researchers around the world to dwell into these small carbon structures in search of potential applications and patents, along with fundamental growth mechanisms. These applications include new composite materials for airplanes, portable X-ray machines and some even proposed a space-elevator made with carbon nanotubes. However, while the hopes for this new material is great, there are still some problems on the production side. While it is possible to produce large quantities of carbon nanotubes, these methods often result in highly bundled nanotubes, which subsequently has to be separated from each other. This coupled with the fact that it is difficult to produce many identical nanotubes due to the sheer amount of possible geometries, means that in situation where few, well-defined nanotubes are needed, such as in many electrical components, there is still a long ways to go. Certain composite materials utilising the tensile strength of carbon nanotubes have however already been produced, and were used in products like a sports-grade bicycle and shielding for a small spacecraft. [8]

This report focuses more on the electrical properties of carbon nanotubes, rather than the mechanical ones. They have a tunable bandgap which lies in the infra-red area and a high electron mobility at 10000-100000 $cm^2/(V \cdot s)$ [3, 4].Their resistance is furthermore low at less than 100 $\Omega/\mu m$, and shorter nanotubes exhibit ballistic transport as a result of this. This property was discovered by Frank et al in 1998 [9], and it has since been shown that carbon nanotubes exhibit ballistic transport on the scale of a few hundred nm. Theoretically with the low resistance, the mean free path should be more than 100 μm leading to ballistic transport in longer nanotubes, however this has yet to be confirmed experimentally [10]. All of this combined makes carbon nanotubes an excellent candidate for high-frequency photodetectors for optical communication.

1.1 Problem statement

The goal of this report is to produce aligned arrays of carbon nanotubes, and use them in the production of a photodetector. To achieve this, the nanotubes will be grown catalytically using chemical vapour deposition. Furthermore produced carbon nanotubes will be compared to bought carbon nanotubes and both will be used for the production of photodetectors.

Modelling of carbon nanotubes

2

2.1 Geometry of carbon nanotubes

Carbon nanotubes are nanoscale cylindrical carbon structures, usually called 1-dimensional (1D) because they have an aspect ratio of 10^4-10^5, with diameters on the scale of a few nanometres and lengths ranging from micro- to millimetres. The simplest configuration known is the single-walled carbon nanotube, which is effectively a rolled up sheet of graphene. Alternatively they can be multi-walled, which is simply several single-walled nanotubes inside one another.

Graphene consists of a monatomic layer of carbon, where each carbon atom is covalently bound with 3 neighbouring carbon atoms. The last valence electron is bound into de-localised π-orbitals with the other neighbouring atoms, called sp^2 hybridization. This results in an extremely strong material. As such the carbon is structured into a hexagonal honeycomb lattice, as can be seen on figure 2.1. When rolled into a nanotube, the interatomic distance changes compared to that of graphene, from 1.42 Å in graphene to 1.44 Å in nanotubes. The ends of these nanotubes are then terminated with a combination of hexagon and pentagon structures, similar to a fullerene. The unit cell of graphene consists of two atoms, and the position of all other unit cells can be described from a linear combination of two real-space unit vectors, $\vec{a_1}$ and $\vec{a_2}$ defined in equation (2.1) and seen in figure 2.1.

$$\vec{a_1} = \begin{pmatrix} \sqrt{3}a/2 \\ a/2 \end{pmatrix}, \quad \vec{a_2} = \begin{pmatrix} \sqrt{3}a/2 \\ -a/2 \end{pmatrix} \tag{2.1}$$

Where a is the lattice constant of graphene. These can also be used to define the unit cell of the carbon nanotube instead. Here two additional vectors will be defined: the chiral vector $\vec{C_h}$ and the translational vector $\vec{T}$. This unit cell is made up of 4 points: 0, A, B and C, which are shown in figure 2.1. The chiral vector goes from point 0 to A and the translational vector goes from 0 to B. By joining points 0-A and B-C a cylinder is formed with the chiral vector being the circumference and the translation vector being the length of the nanotube unit cell. The chiral vector can be defined by the integers n and m, called the chiral indices, as seen in equation (2.2).

$$\vec{C_h} = n\vec{a_1} + m\vec{a_2} \tag{2.2}$$

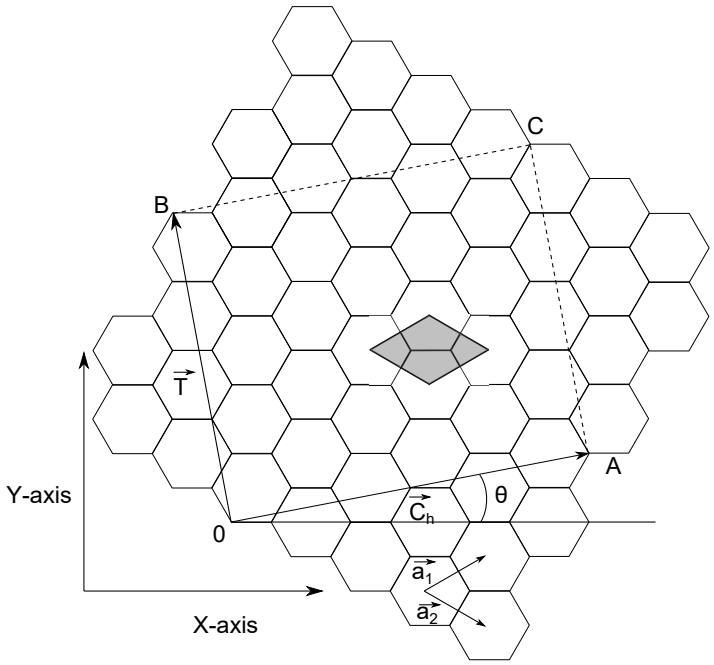

Figure 2.1: *The unrolled unit cell of a (4,2) nanotube, as indicated by the vectors $\vec{C_h}$ and $\vec{T}$ and the dashed lines, with the basis vectors $\vec{a_1}$ and $\vec{a_2}$. The shaded area in the middle shows the unit cell of graphene.*

Depending on how the hexagons align in the rolled up nanotubes, it can either be achiral (symmetric along the center) or chiral (asymmetric along the center). Achiral nanotubes are further classified into two types, zigzag and armchair. Zigzag has a zigzag pattern along its cross-sectional ring and armchair has an armchair pattern as seen on figure 2.2. These configurations can also be defined from the chiral indices n and m: zigzag nanotubes are all nanotubes where m=0, armchair are all nanotubes where n=m, and chiral nanotubes are the ones where $0 \leq m \leq n$. Due to symmetry, m is always considered smaller than or equal to n.

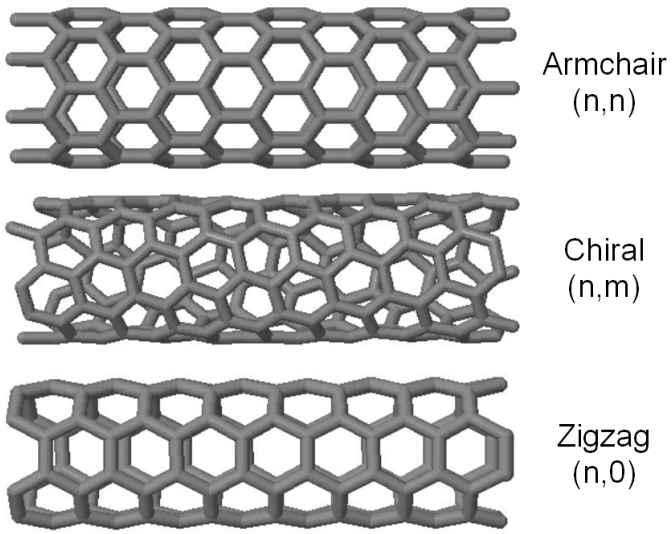

Figure 2.2: *Structure of armchair, chiral and zigzag carbon nanotubes. Modelled in Matlab, and plotted in Molviewer.*

The nanotube circumference is given as the length of the chiral vector as seen in equation (2.3), but it can also be related to the integers n and m. The diameter of a nanotube can then be calculated from the circumferential length as $d_t = L/\pi$.

$$L = \sqrt{\vec{C_h} \cdot \vec{C_h}} = \sqrt{a^2(n^2 + m^2 + nm)} \tag{2.3}$$

The chiral angle as seen in figure 2.1, and ranges from $0 \leq |\theta| \leq 30°$ due to the hexagonal symmetry. The zigzag pattern will have an angle of $\theta = 0°$ and armchair has a angle of $\theta = 30°$. θ can be calculated from n and m, as seen in equation (2.4).

$$\theta = \arctan(\frac{\sqrt{3}m}{2n + m}) \tag{2.4}$$

The translational vector $\vec{T}$ is along the length of the nanotube and perpendicular to the chiral vector. The vector and its length are defined in equation (2.5), where t_1 and t_2 are integers related to m and n as $t_1 = (2m + n)/G$ and $t_2 = -(2n + m)/G$ where G is the greatest common divisor. If there is some symmetry between n and m, meaning that $G > 1$, the size of the nanotube unit cell is greatly reduced as the translational vector will be shorter.

$$\vec{T} = t_1\vec{a_1} + t_2\vec{a_2} \tag{2.5}$$

The length of $\vec{T}$ can be derived by inserting the expressions of n and m into t_1 and t_2.

$$\vec{T}^2 = t_1^2 + t_2^2 + t_1t_2 = \frac{3m^2 + 3n^2 + 3nm}{G^2} = \frac{3L^2}{G^2} \tag{2.6}$$

Finally the number of atoms per unit cell can be found by dividing the area of the nanotube unit cell ($|\vec{C_h} \times \vec{T}|$) with the area of the graphene unit cell ($|\vec{a_1} \times \vec{a_2}|$), as seen in equation (2.7). However, as graphene has two atoms per unit cell, the total number of atoms in the nanotube unit cell is $2N$.

$$N = \frac{|\vec{C_h} \times \vec{T}|}{|\vec{a_1} \times \vec{a_2}|} = \frac{2(m^2 + n^2 + nm)}{G} = \frac{2L^2}{Ga^2} \tag{2.7}$$

2.2 The tight-binding model

In chapter 2.1 it was seen that, depending on the folding, nanotubes of many different chiralities can be created of varying size. This nanotube chirality furthermore has a huge impact on their optical properties, and can determine whether they function as semiconductors or metals, which react very differently when exposed to light. To accurately gauge the optical properties of carbon nanotubes, a model of the band structure must be created. Since they have a relatively simple periodic crystal structure, it is favourable to use the tight-binding model to describe the electronic interactions.

The tight binding-model uses an approximation of the wave functions of single atoms to obtain the band structure of a crystal. The first approximation and where the name stems from, is the fact that the electronic orbitals are tightly bound to their respective ionic core. It has similarities to the method of linear combination of atomic orbitals, because they both consider atomic orbitals in linear combination to obtain an approximation of the real wavefunction. In order for this to be an adequate approximation, it is assumed the electrons have bound solutions, as seen in figure 2.3. The electron will spend most of its time tightly bound to a single atom and not be influenced substantially by neighbouring atoms. [11, 12]

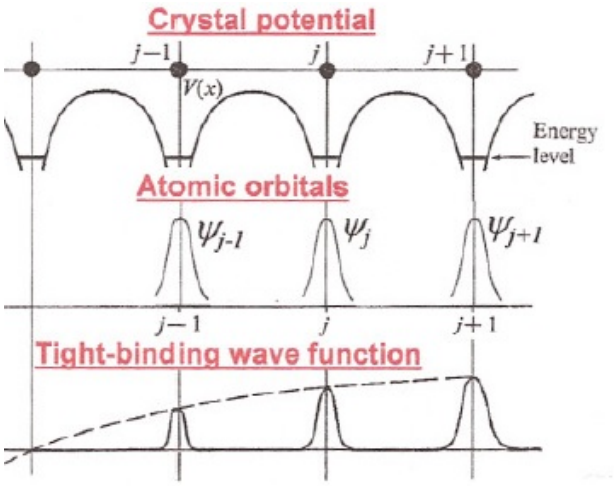

Figure 2.3: *Periodic crystal potential, atomic orbitals and the tight-binding wave-function, with single atom wavefunctions and an envelope Bloch function. Reprinted from M. A. Omar [12].*

The following derivation of the tight-binding model for graphene and carbon nanotubes primarily follows some lectures by Thomas Garm Pedersen [13, 14] with supplementary information from Saito et al. [11]. The basis of the tight-binding model is to model the electrons in an entire crystal structure or molecule as a linear combination of single atomic electron orbitals:

$$\Phi = \sum_{n}^{N} c_n \phi_n \tag{2.8}$$

Here N is the number of atoms and c_n is a normalisation constant. The Hamiltonian of the system can be likewise written as a linear combination. As an example, consider a two-atomic molecule (N=2). The time independent Schrödinger equation for this molecule can be written as:

$$\hat{H}(c_1\phi_1 + c_2\phi_2) = E(c_1\phi_1 + c_2\phi_2) \tag{2.9}$$

From here, the following overlap integrals can be written:

$$H_{nm} = \langle \phi_n | \hat{H} | \phi_m \rangle = \int_{-\infty}^{\infty} \phi_n^*(\vec{r}) \left(\frac{-\hbar^2}{2\mu} \nabla^2 + V(\vec{r}) \right) \phi_m(\vec{r}) \, \mathrm{d}^4 x \tag{2.10}$$

$$S_{nm} = \langle \phi_n | \phi_m \rangle \tag{2.11}$$

Where H_{nm} is the energy overlap between the two orbitals, μ is the mass and n, m are integers denoting specific electrons. Note that the Hamiltonian will incorporate kinetic energy of the electron and the potential of not only the ionic core where it is located, but also the neighbouring potentials, though these are much lower due to the increased distance in the coulomb potential. S_{nm} is the physical overlap between two orbitals. From this, equation (2.9) can be rewritten to the following equations:

$$c_1 H_{11} + c_2 H_{12} = E(c_1 S_{11} + c_2 S_{12})$$
$$c_1 H_{21} + c_2 H_{22} = E(c_1 S_{21} + c_2 S_{22})$$

To simplify these equations, it is first assumed that the overlap between the orbitals is small, meaning that $S_{nm} = 1$ if n=m, and 0 otherwise, which is the key assumption in tight-binding. Furthermore the two atoms in the molecule are assumed identical, so $H_{11} = H_{22} \equiv \alpha$ and $H_{12} = H_{21} \equiv \beta$. The two equations can then be combined into the following matrix equation:

$$\begin{bmatrix} \alpha - E & \beta \\ \beta & \alpha - E \end{bmatrix} \cdot \begin{bmatrix} c_1 \\ c_2 \end{bmatrix} = 0 \tag{2.12}$$

For this equation to have a non-trivial solution, the determinant of the matrix must be zero.

$$(\alpha - E)^2 - \beta^2 = 0$$
$$E = \alpha \pm \beta \tag{2.13}$$

This result gives us two different solutions for the wave function; one where $c_1 = c_2$ (equally likely to find an electron around either core) and $c_1 = -c_2$ (electrons are restricted to only one core). These are denoted the bonding and anti-bonding solutions, where the former can be interpreted as a chemical bond between the two atoms, which normally has the lowest energy. This solution is fairly simple, and can be easily expanded for larger molecules.

2.3 Band structure of graphene

Since graphene is a large sheet of ordered carbon atoms, where each carbon atom is connected to 3 others, trying to solve equation (2.12) systematically for the entire structure would be an enormous task by itself. As such the problem is simplified by considering the periodicity of the graphene structure. Graphene can be reduced to a two-atomic unit cell, as seen in figure 2.4 where A and B denote the atoms.

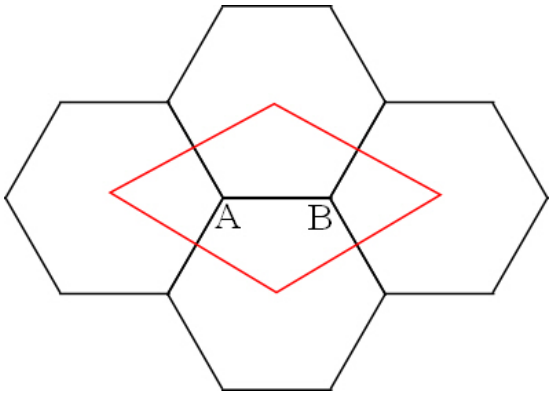

Figure 2.4: *Graphene structure with unit cell outlined in red.*

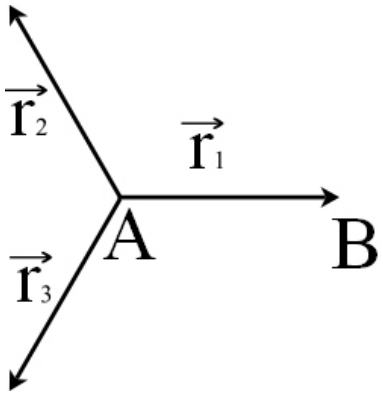

Figure 2.5: *Relevant vectors between atoms in the graphene lattice.*

Since graphene is periodic by nature, any wave function in the lattice must satisfy the Bloch condition:

$$\phi(x+a) = \phi(x)e^{ika} \tag{2.14}$$

Where $a = 2.46$ Å is the lattice constant of graphene, and k is the Bloch wave vector which is periodic with the crystal. From this it is possible to calculate the contribution from all other parts of graphene by multiplying with a corresponding phase factor. As such, the wave function of the entire lattice can be expressed as a Bloch sum:

$$\chi_A = \frac{1}{\sqrt{N}} \sum_n e^{inka} \phi_A(x+na) \tag{2.15}$$

Where N is the total number of unit cells and n is an integer which refers to a particular unit cell. These will be substituted into equation (2.8), to give the wave equation for electrons in graphene:

$$\Phi = c_A\chi_A + c_B\chi_B \tag{2.16}$$

Once again the overlap integrals can be defined. Only the contributions from the nearest neighbour atoms will be considered, since the rest are nearly zero. It is still valid that $H_{AA} = H_{BB} \equiv \alpha$, however since there are now three neighbours for atom A or B to bind to, H_{AB} and H_{BA} must be otherwise defined. Taken atom A as an example, the vectors between it and the nearest neighbour (see figure 2.4) can be defined as:

$$\vec{r_1} = \frac{a}{\sqrt{3}}\begin{bmatrix}1\\0\end{bmatrix} \qquad \vec{r_2} = \frac{a}{\sqrt{3}}\begin{bmatrix}-1/2\\\sqrt{3}/2\end{bmatrix} \qquad \vec{r_3} = \frac{a}{\sqrt{3}}\begin{bmatrix}-1/2\\-\sqrt{3}/2\end{bmatrix} \tag{2.17}$$

From these H_{AB} can be defined as:

$$H_{AB} = \beta' \left(1 + e^{i(\vec{k}\cdot(\vec{r_2}-\vec{r_1})} + e^{i(\vec{k}\cdot(\vec{r_3}-\vec{r_1})}\right) = \beta' e^{-i\vec{k}\cdot\vec{r_1}} \left(e^{i\vec{k}\cdot\vec{r_1}} + e^{i\vec{k}\cdot\vec{r_2}} + e^{i\vec{k}\cdot\vec{r_3}}\right)$$
$$= \beta' e^{-i\vec{k}\cdot\vec{r_1}} \left(e^{ik_x \frac{a}{\sqrt{(3)}}} + 2e^{-ik_x \frac{a}{2\sqrt{3}}} \cos\left(\frac{k_y a}{2}\right)\right) = \beta h(k)$$

Where $\beta = \beta' \exp(-i\vec{k}\cdot\vec{r_1})$ and the parenthesis is shortened into $h(k)$. Once again assuming the $\overleftrightarrow{S}$ matrix to be unity or zero, the following matrix equation can be written:

$$\begin{bmatrix} \alpha - E & \beta h \\ \beta h^* & \alpha - E \end{bmatrix} \cdot \begin{bmatrix} c_A \\ c_B \end{bmatrix} = 0 \tag{2.18}$$

This finally leads to the following equation for the energy of π-electrons in graphene:

$$E = \alpha \pm \beta \left[1 + 4\cos^2\left(\frac{k_y a}{2}\right) + 4\cos\left(k_x \frac{\sqrt{3}a}{2}\right)\cos\left(k_y \frac{a}{2}\right)\right]^{1/2} \tag{2.19}$$

This once again gives rise to two separate solutions, bonding and anti-bonding. By integrating around the edge of the reduced Brillouin zone as seen in figure 2.6, it is possible to plot the band structure of graphene, as can be seen in figure 2.7. Here β is 3 eV and α is set to 0 because it is independent of $\vec{k}$ and is seen as an off-set value.

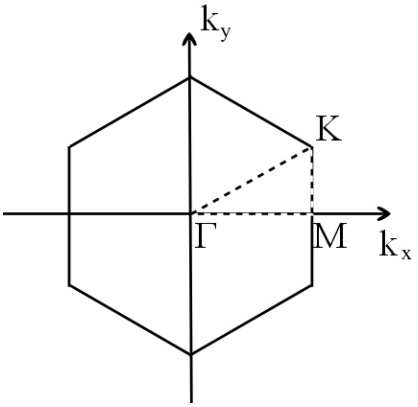

FIGURE 2.6: *Irreducible brillouin zone of graphene*

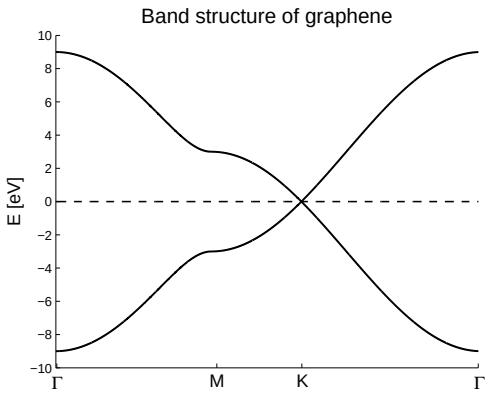

FIGURE 2.7: *Graphene band structure.*

The upper band represents the antibonding solution for the π-electrons, whereas the lower band is the bonding solution. Both solutions are degenerate exactly in the K or Dirac point $(k_x = 1/(\sqrt{3}),\ k_y = 1/3)$. Since the two energy bands are touching, and the density of states at the Fermi level is zero, graphene is effectively a zero gap semiconductor or quasi-metallic. As shown in the next section, the fact that the bands touch leads to some of the unique electronic properties observed in carbon nanotubes.

2.4 Band structure of carbon nanotubes

The calculations for graphene can be expanded to fit carbon nanotubes, by changing the unit cell using the chiral and translational vector. Figure 2.8 shows the relevant quantities needed for these calculations. The coordinate system is chosen so that k_x is parallel to the x direction and k_y to the y-direction with respect to figure 2.1.

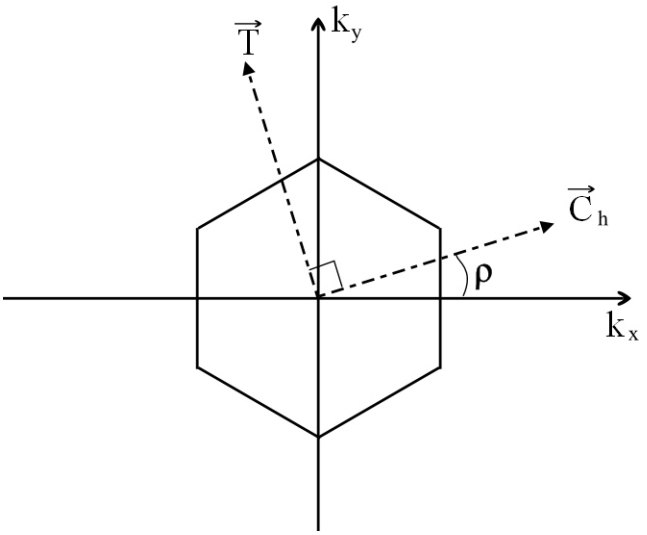

Figure 2.8: *Brillouin zone of graphene with relevant vectors for modelling the carbon nanotube band structure. Note that $\vec{C_h}$ and $\vec{T}$ are real space vectors shown in reciprocal space.*

The basis vectors to represent the reciprocal unit cell of graphene are seen in equation (2.20). $\vec{b_1}$ is perpendicular to $\vec{a_1}$ and $\vec{b_2}$ is perpendicular to $\vec{a_2}$.

$$\vec{b_1} = \begin{pmatrix} 2\pi/\sqrt{3}a \\ 2\pi/a \end{pmatrix} \quad \vec{b_2} = \begin{pmatrix} 2\pi/\sqrt{3}a \\ -2\pi/a \end{pmatrix} \tag{2.20}$$

On figure 2.8 the hexagon denotes the Brillouin zone of graphene which is found by taking reciprocal wavevectors $\vec{b_1}$ and $\vec{b_2}$ and their shortest linear combinations and cutting them in half with a perpendicular line. The eg. $(\vec{b_1}+\vec{b_2})/2$ will yield a y-cutting line intersecting the M point on the figure. This is the same method as used for finding the Wigner-Seitz cell in real space. For convenience the coordinate system is rotated to fit with the $\vec{C_h}$ and $\vec{T}$ vectors, according to the following relations:

$$k_x = k'_x \cos(\rho) - k'_y \sin(\rho) \tag{2.21}$$
$$k_y = k'_x \sin(\rho) + k'_y \cos(\rho) \tag{2.22}$$

Where the prime denotes coordinates in the rotated coordinate system. From these, k-values from the original coordinate system can be translated to the unit cell coordinate system.

Since the adjusted k_x denotes electronic states perpendicular to the nanotubes, it effectively goes around the walls of the nanotube. This however means that the value of k'_x cannot be chosen freely; it must be chosen so that the electron wave function is periodic after a full trip

around the circumference R of the nanotube, which can be written as R=2πr, with r being the nanotube radius. As such k'_x must now satisfy the following:

$$e^{i(k'_x R)} = 1 \qquad \Rightarrow \qquad k'_x R = p2\pi \tag{2.23}$$

Where p is an integer. As such k'_x is now quantified after rolling up the graphene. k'_y can however still be chosen freely, and will therefore be denoted as k. As such, equations (2.21) and (2.22) can be rewritten to:

$$k_x = \left(p\frac{2\pi}{R}\right)\cos(\beta) - k\sin(\beta) \tag{2.24}$$

$$k_y = \left(p\frac{2\pi}{R}\right)\sin(\beta) + k\cos(\beta) \tag{2.25}$$

By inserting these into equation (2.19) the band structure of a given nanotube can thus be calculated. Depending on the choice of chiral indices (n,m), different band structures can be obtained. This can be seen in the equations for the vectors $\vec{T}$ (2.5) and $\vec{C_h}$ (2.2), which in turn change the k-values used to calculate the energies. Pictured in figure 2.9 is an example for the quasi-metallic (4,1) nanotube, as well as the semiconducting (4,2) nanotube in figure 2.10.

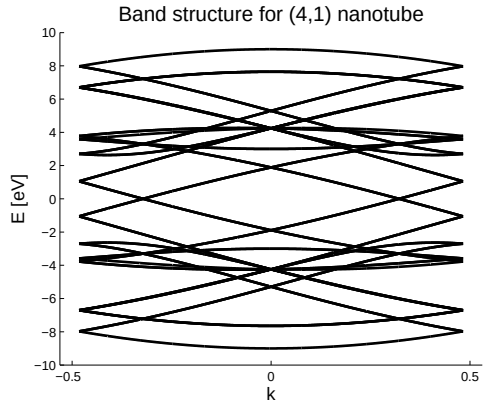

FIGURE 2.9: *Quasi-metallic (4,1) nanotube*

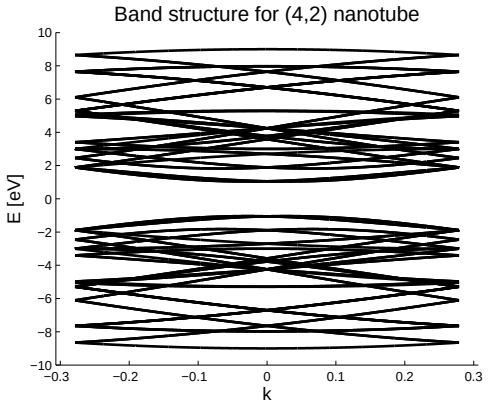

FIGURE 2.10: *Semiconductive (4,2) nanotube*

Note that the band structure is made up of multiple solutions, one for each band; each of the solutions corresponds to a specific atom in the nanotube unit cell. As can be seen from the figure, the band structure changes a lot depending on the chirality. For the quasi-metallic nanotube in figure 2.9, there is no well defined band gap, as opposed to the semiconducting nanotube in figure 2.10 which has a band gap of ≈1 eV. Note that the quasi-metallic nanotubes have k_x solutions which intersects the Dirac point of the Brillouin zone, leading to a band structure with no bandgap. The general rule for which nanotubes are quasi-metallic and which are semiconducting, is that if $(n-m) = 3q$, where q is an integer, the nanotubes will be quasi-metallic; otherwise they will be semiconducting. As such, of a random distribution of nanotubes, approximately 1/3 of the nanotubes will be metallic. For multi-walled carbon nanotubes the electrical properties will be dominated by the conducting tubes, leading to them always acting quasi-metallic.

2.5 Density of states and transition energies of carbon nanotubes

It is also possible to use this method to calculate the density of states for a given nanotube. The simple way to do this is to make a histogram of all the different energy solutions to the different k-values, where the energy interval between states is chosen to be small. The result can be seen in figures 2.11 and 2.12.

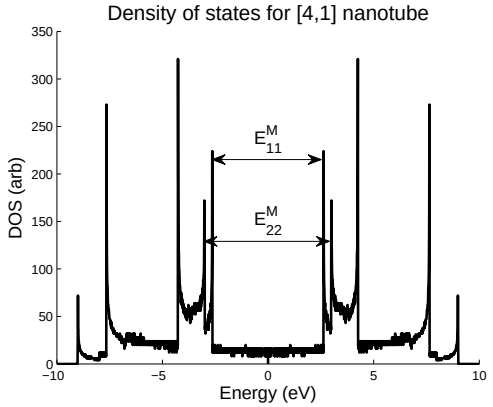

Figure 2.11: *Metallic (4,1) nanotube*

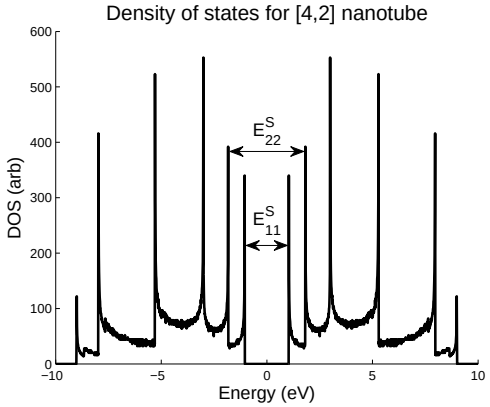

Figure 2.12: *Semiconductive (4,2) nanotube*

Once again it can be seen that for the quasi-metallic nanotube in figure 2.11 states still exist around the Fermi level ($E = 0$ in the figure), whereas no such states exist for the semiconductive nanotube. Another important property which can be seen on both semiconducting and metallic nanotubes are the very sharp peaks, commonly referred to as Van Hove singularities. The peaks follow a series of reciprocal squareroots seen in equation (2.26).

$$DOS(E) = \sum_n \frac{1}{\sqrt{E - E_n}} \tag{2.26}$$

On the figures, the transition energies E_{ii} have also been marked, with superscript S denoting semiconducting nanotubes and M denoting metallic. These are the energy differences between the first and second pairs of Van Hove singularities in the bands, with subscript i denoting the specific singularity, $i = 1$ being the one closest to the Fermi level. These are unique for each variety of nanotube, however they are shown to be highly dependant on the nanotube diameter, as seen on figure 2.13. It is furthermore clear that both the transition energies for quasi-metallic nanotubes are higher than both first and second transition energies in semiconducting nanotubes.

The Van Hove singularities are related to the 1D nature of carbon nanotubes and exist in other kinds of nanowires as well. From the density of states of the semiconducting nanotubes, the bandgap can be calculated, and by doing it for many different values of (n,m) the bandgap energies can be shown to follow equation (2.27).

$$E_g = \frac{\beta L_{C-C}}{d} \tag{2.27}$$

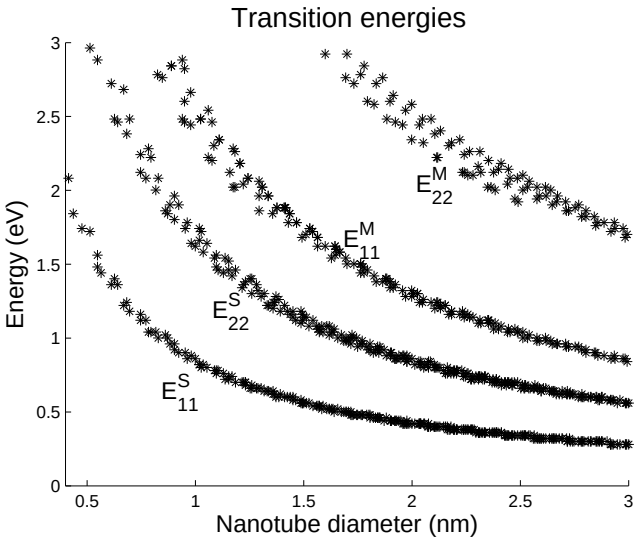

FIGURE 2.13: *Dependency of first and second order transition energies on nanotube diameter.*

Where $L_{C-C} = 1.44$ Å is the interatomic distance, d the diameter and β refers to the expectation value of the overlap energy, seen in equation (2.19). For very large nanotubes it goes towards the zero bandgap value of graphene, which makes sense as the curvature of the nanotube will be small.

Similar band structure and plot for the transition energies were done by Saito et. al. [11] while experimental scanning tunnel microscopy data on individual single-walled carbon nanotubes done by Wildöer et al. [15] has the same bandgap trend.

Principles of photodiodes

3

3.1 Introduction to Schottky barriers

When a metal and a semiconductor come in contact, the Fermi levels of the two will equalise. For this to happen, some of the electrons from the side with the highest Fermi level will travel into the other material, if states with lower energy are available. This can potentially occur for any material interface, but insulators often have no available states between their valence band and the Fermi level of the material in contact. The moved electrons will form an internal electric field which causes the valence (E_v) and conduction (E_c) bands of the semiconductor to bend at the interface.

Figures 3.1 and 3.2 show the bands before and after contact between a metal and a p-type semiconductor. On the figures, the vacuum level (E_{vac}) for the electrons also exhibits band bending due to the internal field. The bending is seen in a region of a few hundred nanometers called the depletion region. The built-in voltage (V_{bi}) corresponds to the amount of band bending. Note that the change in Fermi level of the semiconductor, with respect to the intrinsic (E_{Fi}) level, is defined as $e\phi_p$.

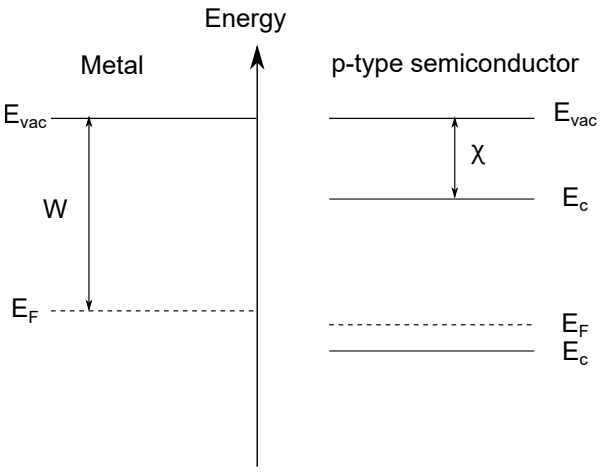

FIGURE 3.1: *Before contact*

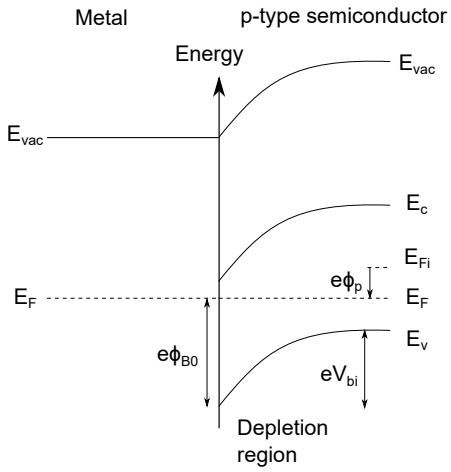

FIGURE 3.2: *In contact with bandbending*

The ideal Schottky barrier (ϕ_{b0}) is calculated from equation (3.1), with W being the work function of the metal, and χ_{sc} the electron affinity of the semiconductor.

$$\phi_{b0} = W - \chi_{sc} \tag{3.1}$$

For this example semiconducting p-type nanotubes are considered, as these are the ones most commonly grown from chemical vapour deposition [16]. For a typical p-type semiconductor where $W > \chi_{sc}$, the electrons will flow from the metal and into the semiconductor acceptor states, leaving positive charge in the metal at the interface. [17]

3.1.1 Operating principle of a Schottky barrier

The Schottky barrier behaves as a diode with rectifying behaviour, which means that the effect of any applied bias will be directionally dependant. When applying a positive bias voltage to the metallic side of a Schottky barrier with a p-type semiconductor, the Fermi level in the metal will be lowered with respect to the Fermi level of the semiconductor. This results in a heightened barrier due to the increased work function of the metal. The Schottky barrier will have the same value, but the added energy from the applied voltage is added to the effective barrier, resulting in very little current through the barrier. This effect is illustrated on figure 3.3. If a negative bias is applied to the metal, the barrier will be lowered along with the band bending, as illustrated in figure 3.4. Disturbing the equilibrium between drift and diffusion current will cause more electrons from the metal to diffuse into the semiconductor due to the internal electric field, resulting in a net current. [17]

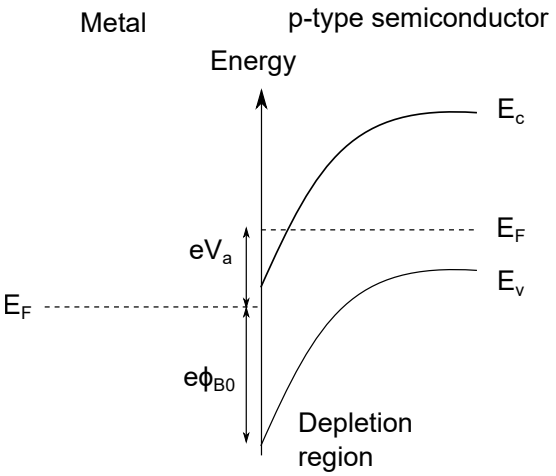

Figure 3.3: *Reverse bias*

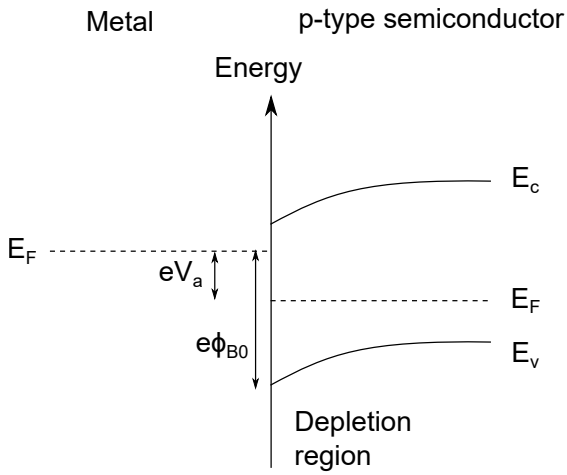

Figure 3.4: *Forward bias*

3.1.2 Schottky barrier lowering

The Schottky barrier has two major effects which cause it to deviate from that of an ideal barrier: Schottky barrier lowering and interface states. Schottky barrier lowering is due to electrostatic forces; if a charged dielectric material is placed near a metal the effective barrier is lowered. This charge either attracts or repels electrons from the metal in a distribution, which can be calculated as a dipole from the image charge method. Limiting the calculations to one dimension, the force and electric field can be found from equation (3.2):

$$F = \frac{-e^2}{4\pi\epsilon_s(2x)^2} = -eE \tag{3.2}$$

Here F is the electrostatic force, e the elementary charge and ϵ_s the permittivity of the semiconductor. The potential from the induced electric field is as seen in equation (3.3), using the image charge method. The aim is to end up with an expression for the altered barrier height, due to the effect described above. The potential is assumed to be zero at infinity, with the coordinate system defined in figure 3.5.

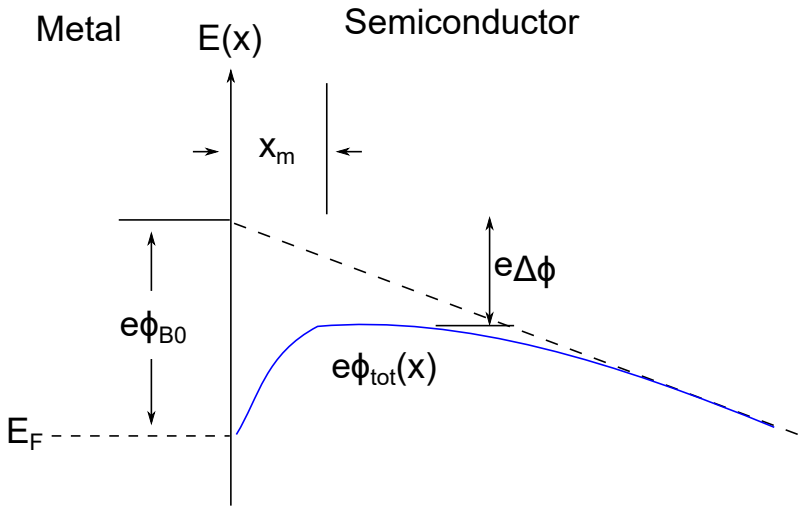

FIGURE 3.5: *Typical Schottky barrier lowering. The blue line indicates the actual Schottky barrier and the dashed line the ideal Schottky barrier.*

$$\phi(x)_{im} = \int_0^\infty \frac{e}{4\pi\epsilon_s 4(x)^2}\mathrm{d}x = \frac{e}{16\pi\epsilon_s x} \tag{3.3}$$

Considering the initial barrier height $\phi_{B0}(x)$ to decrease linearly to zero at its width and the decreasing potential to be ϕ_{im}, where the sum of the two will be denoted $\phi_{tot}(x)$. As done in equation (3.4), differentiating the total potential and setting it equal to zero, the x coordinate for the peak height of the barrier can be found. The resulting change in barrier height can be seen in equation (3.5), where x_m has been inserted into ϕ_{tot}:

$$\frac{d\phi_{tot}}{dx} = \frac{de}{16\pi\epsilon_s dx} + \frac{dEx}{dx} = 0 \rightarrow x_m = \sqrt{\frac{e}{16\pi\epsilon_s E}} \tag{3.4}$$

For a semiconducting carbon nanotube ($\chi = 2.9$ eV) Schottky barrier with an chromium electrode ($W = 4.5$ eV), with an ideal barrier height of 1.6 eV, the resulting change in barrier height will be on the scale of 0.4 eV ($\Delta\phi$) and thus this effect is considerable. [17, 18]

$$\Delta\phi = \sqrt{\frac{eE}{4\pi\epsilon_s}} \tag{3.5}$$

3.1.3 Interface states

Another impactful effect, is the generation of interface states between metal and semiconductor. When connected, the two will create covalent or dangling bonds at the interface, where the electron's states will lie in the semiconductor band gap. This causes electrons from the semiconductor valence band to fill up the interface states, and thus pin the Fermi level at a lower energy level. Similarly for heterostructures, interface states can be created and pin the Fermi level. Interface states can be donor- or acceptor-like, depending on the materials used.

For Schottky barriers this Fermi level pinning can generate their own depletion regions and thus change the Schottky barrier. In semiconductors this is the dominating effect, and the ideal Schottky barrier equation is therefore ineffective [19]. As seen in figure 3.6, only the first few monolayers of either metal or semiconductor will contribute to the interface layer, which is typically below 5 Å. The interface states below the Fermi level are filled shown as a grey area. Note that the wave function $\Psi(x)$ has a separate vertical-axis from the rest of the figure; specifically referring to the metal induced gap states, it was proposed by Heine [20] that the metal Bloch wavefunctions penetrate into the semiconductor, due to the boundary condition that the wavefunction has to be continuous over the interface. This allows for electron states at the interface. By passivating the semiconductor's surface, this effect can be avoided to some extent. Passivating can be done by exposing the semiconductor to a chemical, or with polar molecules that remove the dangling bonds before connecting it to the metal. [21]

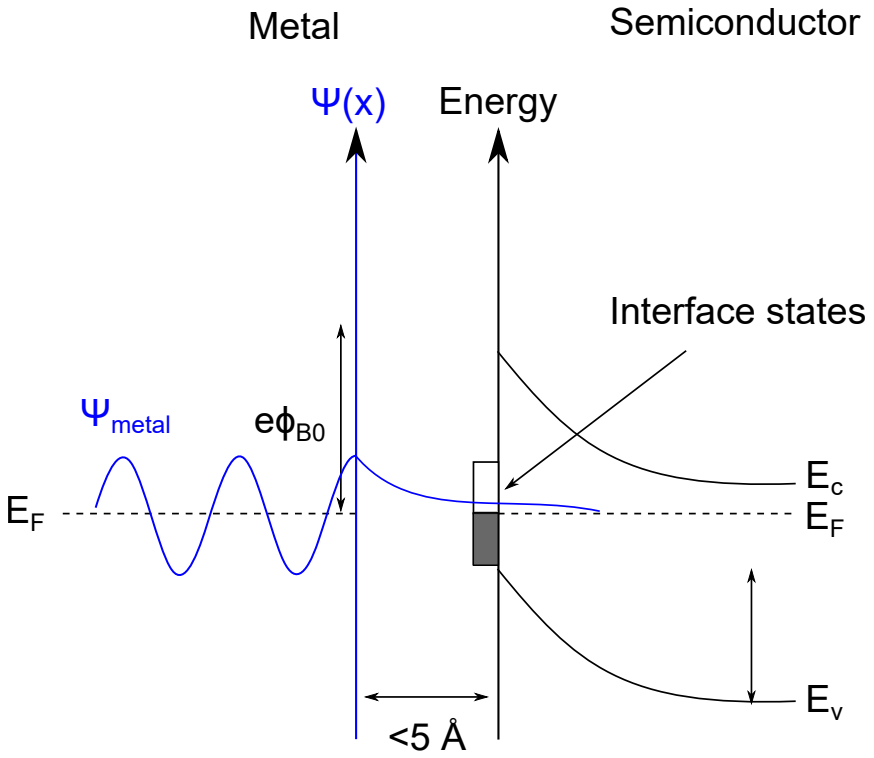

Figure 3.6: *Interface states at a metal-semiconductor interface with the wavefunction of the metal penetrating into the semiconductor, to illustrate why states change, when two materials come in contact.*

3.1.4 Current-voltage characteristics

The current is mainly described by thermionic emission theory. However, diffusion and tunnelling currents are also present, but the contribution from these are not considered. From the equation it can be seen that there is a diode characteristic, also illustrated in figure 3.7. Comparing the Schottky barrier with a pn-junction, the Schottky barrier has two major differences, the first being a higher dark current in the reverse direction and the second being the switching mechanism. For a Schottky barrier the current is carried by majority carriers, which means the diffusion current is small. The capacitance from this is thus nearly non-existent, making the RC time constant small. Additionally when switching between forward and reverse bias, there are no minority carriers stored which have to diffuse, as opposed to a pn-junction, making the Schottky barrier a device capable of high frequency. [17, 18]

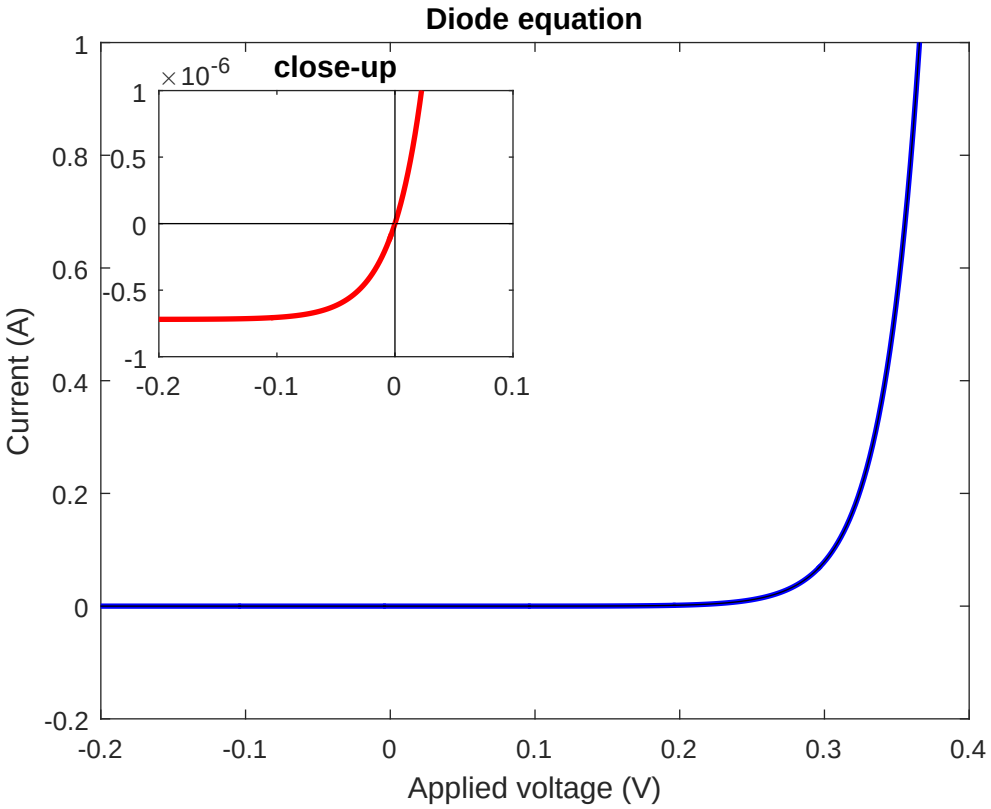

FIGURE 3.7: *I-V characteristics of a Schottky barrier using equation (3.6). Parameters:* $T = 300\ K$, $A = 1.44\ A/K^2\ m$, $\phi_b = 0.67\ eV$.

3.1.5 Thermionic emission theory

For a metal in connection with a n-type semiconductor the transport of electrons can be described by thermionic emission theory. In 1873 Frederick Guthrie released an article [22] on electricity emitted from hot bodies, sparking the first measurements on thermionic emission. However the situation of a Schottky barrier is not necessarily a 1500 K hot metal. Instead the velocity needed to overcome the potential barrier is overcome due to the applied bias (V_a).

The thermal current can be calculated from equation (3.6), the derivation of which can be seen in appendix B.

$$J = A^* T^2 \exp\left(\frac{-\phi_b}{k_b T}\right)\left[\exp\left(\frac{V_a}{k_b T}\right) - 1\right] \tag{3.6}$$

This equation is similar to the standard diode equation and varies exponentially with the applied voltage and the height of the Schottky barrier, see figure 3.7 for a typical plot. A^* is the Richardson constant and depends on the semiconductor, T is the temperature and k_b is the Boltzmann constant. The -1 term is added for the current flowing in the other direction than the applied bias.

3.2 Semiconducting photodiodes

A semiconductor p-n junction can be used as both a photovoltaic cell or as a photodiode depending on the bias voltage. A forward bias is used for a photovoltaic cell, where the positive bias is applied to the p-type semiconductor and used to generate electron-hole pairs which can recombine into photons. A reverse bias is applied by having the positive side on the n-type semiconductor. When a photon with energy matching the band gap is incident on a semiconductor, it will create an electron-hole pair, and due to the build-in electric field inside the p-n junction, the electron and hole will separate and cause a current opposite to the bias direction. The current in the reverse bias direction generates a voltage drop across the resistive load seen in figure 3.8, which in turn generates a forward-bias current. The equation for the current can be seen in equation (3.7), where the last term has been derived from the ideal diode equation. The I_s factor is dependent on the recombination in the particular p-n junction. The current will run in the forward bias direction if the applied bias is high enough. [17]

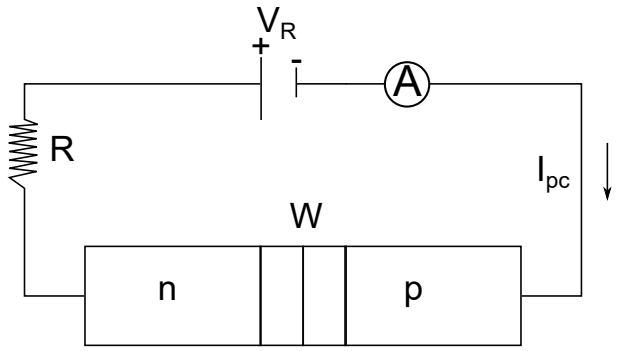

Figure 3.8: *A p-n junction photodetector operated at reverse bias with a resistive load (R) and depletion layer (W).*

$$I = I_{pc} - I_s\left(\exp\left(\frac{eV_{bias}}{k_b T}\right) - 1\right) \tag{3.7}$$

I_{pc} is the photocurrent, I_s and the exponent are the current from the applied bias. e is the elementary charge and $k_b T$ is the thermal energy. A photodiode is operated under reverse bias with respect to the junction, and the current running through can be found by integrating over

the depletion region, as shown in equation (3.8). W is the width of the depletion layer. The integral can be simplified if the generation rate (G_L) is constant through out the region. Only the 1D case is considered here.

$$J_{L1} = e \int G_L \, dx = eG_L W \tag{3.8}$$

This current is the instant response of the photodiode and the maximum frequency is on the scale of GHz, due to the small width of the barrier and the high drift velocity. However no photodiodes are this fast since they are slowed by a diffusion current. The diffusion current can be found from the ambipolar transport equation, and is derived in appendix (A). It results in a photocurrent originating from outside the depletion layer. The added distance is the diffusion length of holes and electrons in the n- and p-region respectively. The total width capable of producing photocurrent is a combination of the depletion region and the diffusion length. [17]

3.3 Schottky barrier photodiodes

The Schottky barrier photodiode works much like a semiconductor photodiode. When a photon with energy corresponding to the band gap of the semiconductor it hits, an electron is excited from the valence band and into the conduction band. A hole or empty state is generated when the electron is excited, and thus some positive charge is left behind. Normally the electron and hole pair would recombine after a given time, but if the photon is incident in the depletion region of the semiconductor, the built in electric field will separate the two because of their different charges, creating a current. An ampere meter connected in series to the circuit seen in figure 3.9 and operated in reverse bias is a photodetector. The Schottky barrier in a circuit converts a photon signal into an electrical one. [17]

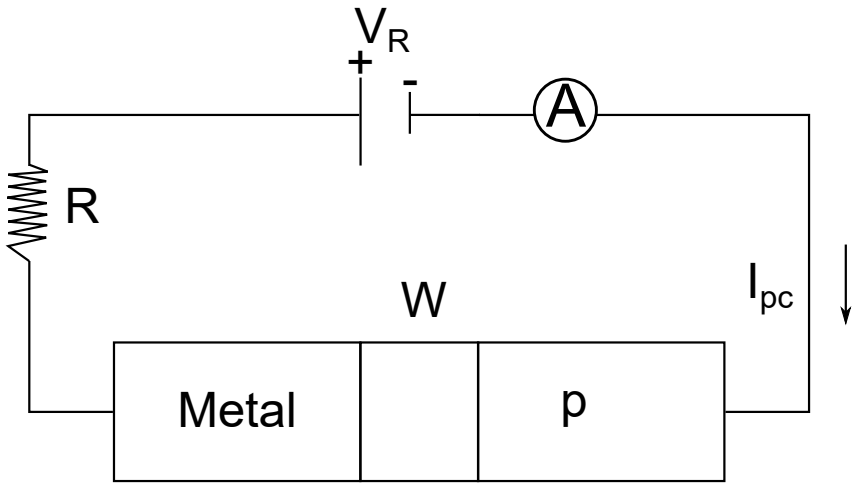

FIGURE 3.9: *A Schottky photodetector operated at reverse bias with a resistive load (R) and depletion layer (W).*

3.4 Figures of merit for photodetectors

The primary figures of merit to characterise a photodetector are external quantum efficiency, responsivity and cut-off frequency. The external quantum efficiency of photodetectors is seen in equation (3.9), which defines the percentage of incident photons that generate charge carriers. I_{pd} is the photogenerated current, P_{opt} the optical irradiance, $h\nu$ the energy of the each photon and e the elementary charge. [23]

$$\eta_{ext} = \frac{I_{pd}}{e}\frac{h\nu}{P_{opt}} \tag{3.9}$$

Optimally η should be equal to 1, which means each incident photon generates an electron-hole pair. However due to optical reflections, carrier recombination and the finite width of the depletion region, η will always be less than 1. Often the Responsivity (R_{pd}) will be listed instead. This is defined as the photocurrent to irradiance ratio and yields units of current/watt, as seen in equation (3.10).

$$R_{pd} = \frac{I_{pd}}{P_{opt}} \tag{3.10}$$

Responsivity is a parameter used to compare photodetectors to each other, since it is easier to relate to measurements.

The cut-off frequency is the maximum frequency where the photodetector signals of two different photon pulses can still be distinguished. The cut-off frequency for a Resistance-Capacitance (RC) circuit is defined in equation (3.11), where the cut-off frequency is taken when the signal has attenuated by 3dB. At a high frequency the signal will start to attenuate or be reflected due to capacitance and carrier transit time. The capacitance arises from the junction at the metal-semiconductor interface, where there is a charge build-up. [23]

$$f_{RC} = \frac{1}{2\pi R_{eff} C_{pd}} \tag{3.11}$$

Transit time is the time it takes for a photogenerated charge carrier to move through the depletion region and into an electrode. Using an average carrier velocity ($<v>$)[17] and assuming uniform photogeneration in the depletion layer, the cut-off frequency can be estimated by equation (3.12) [24], where d_{abs} is the one dimensional width of the depletion region.

$$f_t \simeq \frac{3.5 < v >}{2\pi d_{abs}} \tag{3.12}$$

The combined frequency maximum is described by adding the squared reciprocal values as seen in equation (3.13) which is similar to adding resistances in parallel. The equation greatly depends on the highest frequency. [23]

$$f_{3dB} \simeq \sqrt{\left(\frac{1}{f_{RC}^2} + \frac{1}{f_t^2}\right)^{-1}} \tag{3.13}$$

3.5 Metal-Semiconductor-Metal detectors

Placing a metal in the both ends of a semiconductor yields a symmetrical electric field, given that the semiconductor and metal are both only made of one material, as illustrated on figure 3.10. Incident photons on the semiconductor will excite an electron-hole pair and even though there is a built-in electric field, the potential barrier in both ends trap the electron-hole pair and they will recombine. Thus little photocurrent is observed in the semiconductor. In the case of two different metals it is possible to align the work function of these two to the valence and conduction band of the semiconductor. This yields a low effective Schottky barrier in one end and a high one in the other, causing some current when the electron-hole pair is created. [18, 25]

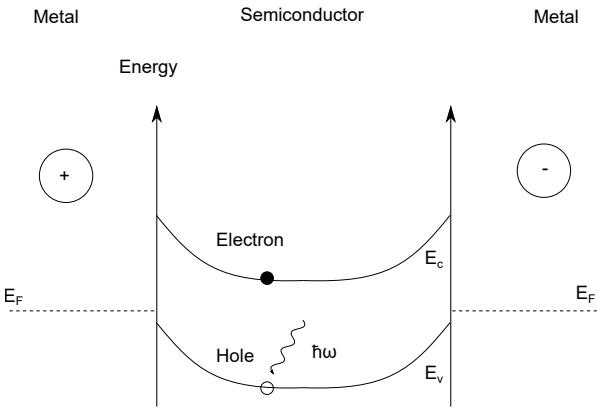

FIGURE 3.10: *MSM detector with zero bias*

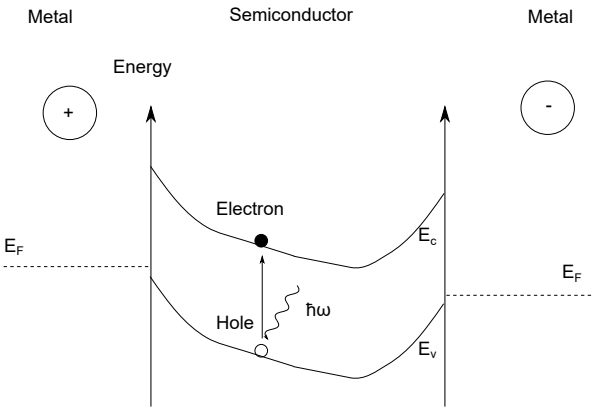

FIGURE 3.11: *MSM detector with small bias*

Applying a small bias to the MSM (metal-semiconductor-metal) configuration causes the bands to shift as seen in figure 3.11. The electric field enables the photon generated electron and hole to very rarely go through the potential barrier, causing a small photocurrent. The majority of electrons are still trapped, and the coulomb attraction between the hole and electron holds the hole back. There is essentially no energy barrier for the hole, but the overall energy of the system would be higher because of the lone electron. Going back to equation (3.6) for the current for a single Schottky barrier, it can be seen that the if $\phi_b > V_a$, the contribution to the current from the exponential functions will be much lower than one. This means there is a small current from the applied bias and an even lower current from the photogenerated electron-hole pair. [18, 25]

Applying a large bias, referred to as the punch through bias, is the operating bias mode of the MSM detector. The applied bias exhibits an electric field large enough to widen the depletion region and compensate the built-in electric field at the opposing Schottky barrier, see figure 3.12. If the applied bias is large enough it can cause the depletion region to go all the way to the opposite electrode; this is called the flatband voltage. The electron and hole respectively will have more energy than the potential from the Schottky barrier and a larger photocurrent is thus observed. [18, 25]

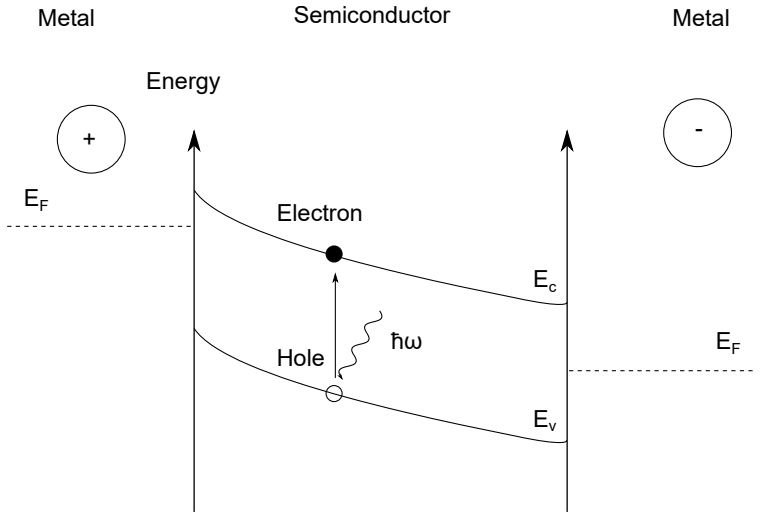

Figure 3.12: *Metal-Semiconductor-Metal detector at a large bias with incoming light which excites an electron hole pair.*

The main advantages of MSM detectors is their high bandwidth and the low dark current. The dark current is small due to the symmetric electric field trap effect described above, whereas many other photodetector types have only one junction. The bandwidth is fast due to the low capacitance in the MSM detector; because there is a low charge build up in Schottky barriers, the bandwidth is normally restricted by carrier transit time. For most semiconductors the effective mass of the hole is higher than that of the electron, which makes this the main restriction on the bandwidth. The primary disadvantage of MSM detectors compared to pn-junction photodetectors is the low responsivity due to the shadowing effect from the electrodes. Because the electrodes are on top of the semiconductor in planar circuits a lot of the incident photons will strike the metal instead of the depletion region, yielding a low quantum efficiency. A secondary disadvantage is the large bias required which make them more power consuming. [23]

The shadowing effect can be minimised by enlarging the space between the electrodes, but this will cause the transit time to be higher. Utilising back illuminated photodetectors can minimise this problem, but then the semiconductor layer has to be thin in order for the generated electron-hole pair pair to be in the depletion region. Again the transit time is increased because the charges are generated far away from the electrodes. [23]

3.5.1 Current-voltage characteristics of MSM configuration

The current-voltage characteristics of the MSM configuration is very dependent on the choice of electrode material and doping of the semiconductor. In figures 3.13 and 3.14, reprinted data from Qi et. al [26], two different characteristics can be observed. In the first figure an asymmetrical curve is exhibited, where the electrode materials in both ends of the configuration are different. In the second figure a symmetric curve is shown where the electrode materials are identical. The primary reason for the appearance of the curves is the Schottky barriers; if the electrode material is the same, the Schottky barrier will be the same. Comparing with figure 3.7 a clear resemblance is seen. Additionally comparing to the band-figures 3.10 and 3.12, the small linear region in the middle can be seen as a small applied voltage and the sharp region as the punch-through bias. The process can be divided into two stages: In the first stage the

voltage is loaded onto the reverse biased Schottky barrier and only a small current is observed due to the large resistance from the barrier. In the second stage the voltage is high enough for the electrons to tunnel through the reverse biased barrier. They are primarily limited by the bulk resistance in the semiconductor and often some contact resistance from a small oxide layer. From this it can be deduced that differentiating the current-voltage curve at the sharp region in stage two, will yield the conductance of the semiconductor while the resistance can be found by taking the reciprocal of this. For the asymmetric curve the Schottky barrier is very low in one end, giving the response on the curve. Note that the figure is taken from data of a study done by Qi et. al. [26] on silicon nanowires, where the heavy doping results in a smaller voltage necessary to tunnel through the reverse biased Schottky barrier. The point of the figure is to be used as a generalisation for the MSM configuration. [27]

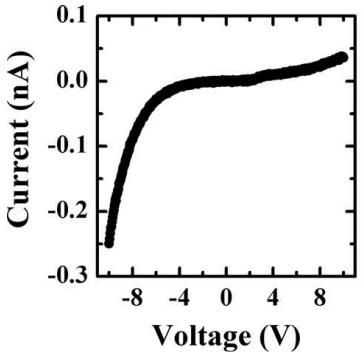

FIGURE 3.13: *Asymmetric curve with 2 different metals and heavily doped silicon. [26]*

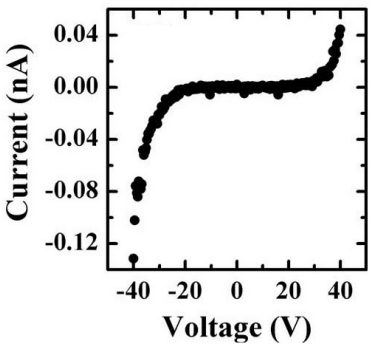

FIGURE 3.14: *Symmetric curve with identical metals with lightly doped silicon. [26]*

3.5.2 Calculation of the cut-off frequency of a carbon nanotube photodetector

The following section is a calculation of a theoretical intrinsic limit to the cut-off frequency of a carbon nanotube photodetector with the same dimensions as the one constructed in the experimental section. Taking equation (3.12) the cut-off frequency for the transit time can be calculated. For a 20 μm gap between the electrodes, the maximum distance the electron will travel is 20 μm. The drift velocity along one axis depends on the electron mobility (μ_e) and electric field (E) seen in equation (3.14). The electric field is assumed to be linearly decaying and the potential has been approximated from the ideal Schottky barrier in equation (3.1). The electron affinity is found to be 2.9 eV from ab initio calculations of a hydrogen passivated, 20 angstrom long (5,5) nanotube, by Buonocore et. al. [28]. The electrode is selected to be chrome ($W = 4.5$ eV), 5 Volts is chosen as the applied voltage and a symmetric electric field between the electrodes is assumed, leading to a 10 μm decay length for a 20 μm depletion region. The mobility has been documented between $10000 - 100000\ cm^2/(V\,s)$ [3, 4], and 1 $m^2/(V\,s)$ is selected. This results in a cut-off frequency at 18.38 GHz.

$$v_{drift} = \mu_e E = 1\ m^2/(V\,s)\frac{(\frac{4.5\ eV - 2.9\ eV}{1.6*10^{-19}\ C} + 5\,V)}{10 * 10^{-6}\ m} = 6.6 * 10^5\ m/s \tag{3.14}$$

$$f_t = \frac{3.5 * 6.6 * 10^5\ m/s}{2\pi * 2 * 10^{-5}} = 1.838 * 10^{10}\ Hz \tag{3.15}$$

Using equation (3.11), the resistance of the nanotubes is taken in parallel to a 50 Ω resistor. The resistor has two main tasks, where the obvious one is to lower the effective resistance of the system. The second task is to have mainly photocurrent going through the photodetector and current from an applied bias to go through the resistor. According to Zhou et. al [29], the resistance of a single carbon nanotube is 36000 Ω which results in an effective resistance of $R_{eff} = (1/50\ \Omega + 1/36000\ \Omega)^{-1} = 49.9\ \Omega$. Others reported the resistance to be a few orders of magnitude higher [30], but the resulting resistance will be similar due to the additional resistor. Taking eg. 100 nanotubes in parallel to the 50 Ω resistor yields an effective resistance of ≈ 44 Ω. The capacitance (C) is approximated as two parallel wires with a radius equal to half the height of the electrodes, $a = 20\ nm$, length $l = 100\ \mu m$ and a distance between the electrodes of $d = 10\ \mu m$. The dielectric constant is chosen to be that of graphene with a relative permittivity of 3.5 [11], assuming a mat of parallel nanotubes cover most of the space between the electrodes. The capacitance is calculated in equation (3.16); an interdigital design of electrodes is taken with 9 fingers from each side, resulting in 17 capacitors in parallel. View figure 6.5 for a top view of such a design. Capacitors in parallel are simply added together. The edge capacitance from the end of the fingers is not included. The cut-off frequency for the RC-time constant can be seen in equation (3.17).

$$C = \frac{\pi \epsilon_{graphene} \epsilon_0 l}{\operatorname{arcosh}(\frac{d}{2a})} = \frac{\pi * 3.5 * 8.854 * 10^{-12} F/m * 10^{-4} m}{\operatorname{arcosh}(\frac{20*10^{-5}m}{2*20*10^{-9}m})} * 17 = 2.396 * 10^{-14} F \tag{3.16}$$

$$f_{RC} = \frac{1}{2\pi * 44\Omega * 2.396 * 10^{-14} F} = 1.51 * 10^{11}\ Hz \tag{3.17}$$

The results from equation (3.17) and (3.15) yield a combined cut-off frequency of 151 GHz from equation (3.13). Compared to a GaAs photodetector ($f_{3dB} = 150$ GHz) [31] the result is close, but far from that of an ultra-fast graphene detector by Xia et. al. [32] who reported an intrinsic bandwidth of more than 600 GHz. The calculation is simplified, but gives an idea of the quantities expected for high frequency photodetectors. However with a smaller separation between the electrodes a similar bandwidth is achievable due to the high electron mobility.

3.6 Carbon nanotube photodetectors

Due to the cylindrical shape of nanotube structures, as well as the unique electronic properties of carbon nanotubes, producing photodetectors based on them has long been the subject of research. Carbon nanotubes have the practical properties of flexibility, high mechanical strength and chemical stability which is good in many environments. However these properties do not matter much for a usable photodetector. What is useful is the tunable band gap with changing chirality. The ability to be active in the infra-red region is especially attractive for carbon nanotubes, as only few semiconductors like that exist. The most common infrared detector, mercury-cadmium-telluride, has a much lower absorption coefficient compared to the single-walled carbon nanotubes. [33]

3.6.1 Carbon nanotube-metal interconnects

Contrary to normal semiconductors, the amount of interface states in carbon nanotube-metal interconnects is low. As such the Fermi level pinning effect is negligible, and the Schottky barrier height will be solely dependent on the work function of the metal. A study done by Leonard et al. [34] with end-connected carbon nanotubes took the interface states into account by adding additional charge at the interface, which gave rise to a dipole layer. Due to the geometry of the carbon nanotubes, the dipole layer is spread out in all directions, causing it to greatly decrease in width to only a few nanometers. The electrons will therefore only see a very thin barrier where they can easily tunnel through, which as stated earlier means that interface states only have a small effect in carbon nanotubes. For side-connected nanotubes, the depletion region is perpendicular to the nanotube main axis. Due to space requirements the bands will thus not align completely and equalize the Fermi levels. Compared to a 3-dimensional bulk material, the surface states, once again modelled as charge, will have to be two orders of magnitude higher to pin the Fermi level and change the Schottky barrier. It is believed that this property of the carbon nanotubes stems from the Van Hove singularities of a 1-d nanostructure, which gives the carbon nanotubes a large density of states for the charges to occupy at the band edge. In conclusion the Schottky barrier height can be controlled by changing the metal which connects to the nanotube. Experimental evidence for this was observed by Z. Chen et al. [35] who also showed that the diameter of the nanotube has a strong influence on the Schottky barrier height, as it drops from 0.7 eV to 0.25 eV on aluminium contacts when the nanotube diameter increases from 0.8 nm to 1.5 nm. The Schottky barrier is of course different for electrons and holes, but has been experimentally determined to be on the scale of 400 meV to a few meV [35, 36]. [37]

3.6.2 Designs of carbon nanotube photodiodes

In order to get photocurrent of a carbon nanotube, a double gate structure can be utilised or a doped carbon nanotube with a single gate. The reason is that the depletion region in carbon nanotubes is very thin (1-3 nm) and thus the creation of an exciton with light wavelength of $\approx 1\ \mu m$ is unlikely. By using the double gate structure seen in figure (3.15) it is possible to electrostatically dope the carbon nanotube into a p- and an n-region, where a long built-in field along the axis of the nanotube can be generated [38]. The built-in field will then be able to split the electron-hole pair and create a photocurrent. Recall from section 3.2 that a photodiode is operated in reverse bias mode with respect to the pn-junction, which is also required here.

Applying a gate potential to the carbon nanotubes causes the electrons and holes respectively to be attracted by the potential. The pn-interface will equilibrate between diffusion and the build-in field from the potential. The single gate structure requires a doped carbon nanotube, where the applied potential creates eg. a pnp-junction, depending on the doping of the carbon nanotube [33]. The reverse direction of bias is undetermined, but the design can be improved by making a barrier free photodiode. This is done by aligning the work functions of the contact materials to the conduction and valence band of the carbon nanotube. Note that both of these designs apply to the semiconducting carbon nanotubes, but only recently was the double gate design applied to a single quasi-metallic nanotube [38].

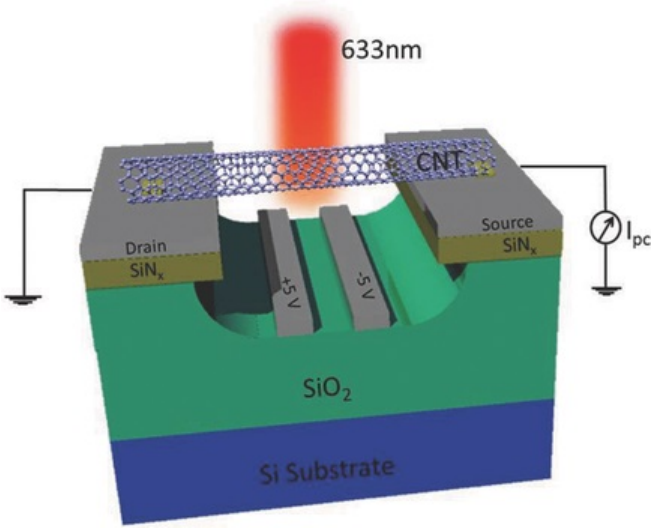

Figure 3.15: *Double gate pn junction on single suspended nanotube. Reprinted from Chang. et. al. [38]*

3.6.3 Brief introduction to excitons

An exciton is a bound state of an electron excited by a photon into the conduction band and a hole is left in the valence band of a semiconductor or an insulator. The term bound is to be understood as bound to each other not a specific space in the lattice. The electron and hole are bound by their mutual Coulomb attraction. For a Frenkel exciton the hole is located at a well defined position in the lattice and the electron can move within a certain distance of the hole. For a Wannier-Mott exciton the hole is able to move around with the electron still linked to it. The exciton is similar to a hydrogen atom with an electron located around a positive core, but the binding energy is much smaller due to the other electrons in the lattice and the typically smaller effective masses of the electron and hole. The binding energy of the exciton, the Coulomb attraction, effectively lowers the band gap of the semiconductor as the binding energy is returned once the excitation has occurred, as seen on figure 3.16. However, for most semiconductors the binding energy is at or below the scale of room temperature $k_bT = 0.26$ meV, and thus the exciton is able to dissociate. For carbon nanotubes the exciton binding energy is much higher, primarily due to the 1D structure, where the exciton is confined and the overlap between electron and hole is increased. In the semiconducting carbon nanotubes, the exciton binding energy is in the range of 200-400 meV.

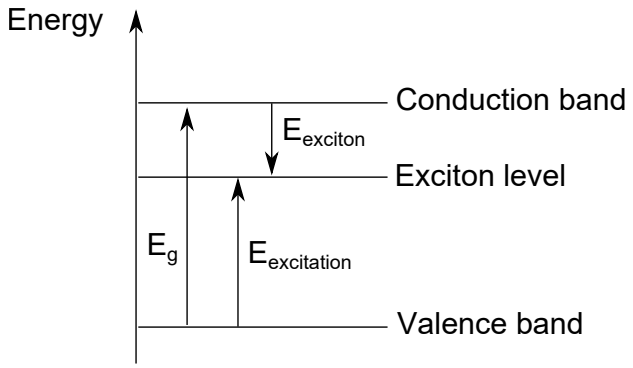

Figure 3.16: *Excitation of a semiconductor or insulator considering the effect of excitons.*

Another important detail for excitons in carbon nanotubes is specific for the quasi-metallic ones. For normal metals the screening of the mutual coulomb interaction by the free carriers in the metal is very effective and hence no excitons have been observed experimentally [39]. The primary reason is that the screening by free carriers in 1D decay slower with distance than in 3D. The other reason is that it is easier to obtain a bound state in a 1D material, as there is only 1 degree of freedom. Excitons in semi-metallic carbon nanotubes were observed experimentally and predicted by F. Wang et al. with a binding energy of 50 meV. [40]

3.6.4 Semiconducting carbon nanotube photodiode

The measured photocurrent of semiconducting carbon nanotubes is higher than the anticipated one due to the high exciton binding energy of $200 - 400$ meV. A lot of energy is required to split the electron and hole apart and turn them into free carriers, which in turn will become photocurrent. As seen on figure 3.17, the electron and hole respectively have to tunnel from the bound state of the exciton into a state in the junction, and then decay into the n- and p-regions. The effective band gap is smaller due to the binding energy of the exciton as shown by the virtual dotted states. Perebeinos et al. [41] proposed the idea of exciton-phonon coupling to dissociate the exciton. Vibrational bands located just around the valence and conduction band are present due to phonons. Some of the generated excitons will be coupled in to these vibrational bands, where the exciton can be dissociated with help from the added energy of the phonon. If the exciton is not dissociated it will recombine and not create photocurrent. The ratio of intensity coupled into the vibrational bands (I_{1v}) compared to the direct band (I_{11}) follow an inverse square root relationship with the diameter of the nanotube, with a max of ($I_{1v}/I_{11} \approx 10\%$) for a 1 nm diameter nanotube. The ratio drops to 7% when the diameter is increased to 2 nm. [41] By considering this mechanism Cheng et al. [38] were able to calculate a photocurrent equal to their experiments, utilising the double gate structure. To ionise the generated excitons which have a binding energy of 400 meV and a diameter of approximately 4 nm, a critical field (F_0) of 100 $V/\mu m$ is required to split all the excitons. If the exciton absorbs an optical phonon of ≈ 200 meV, the critical field is lowered to 50 $V/\mu m$. The phonon assisted photocurrent can be written as in equation (3.18), which essentially is the exciton dissociation rate multiplied by the effective exciton population [42].

$$I_{pc} = eA_{abs}\frac{P_{in}}{E_{ph}}\tau_{ex}\Gamma_0 \tag{3.18}$$

Where the total exciton population is the number of photons absorbed per second determined by the fraction of photons absorbed (A_{abs}), the incident power (P_{in}), the photon energy (E_{ph}) and the exciton lifetime (τ_{ex}). The exciton dissociation rate Γ_0 can be determined from equation (3.19). Lastly the equation is multiplied by the elementary charge e to convert rate to current.

$$\Gamma_0 = \frac{\alpha E_b}{\hbar}\frac{F_0}{F}exp(-\frac{F_0}{F}) \tag{3.19}$$

Where $E_b = 400\ meV$ is the binding energy of the exciton, $\alpha = 4.1$ is a constant and F is the resulting built-in field strength from an applied gate voltage. The resulting photocurrent from equation (3.18) exhibited great agreement with the experimental results, which were on the scale of pico-amperes. Using a double gate voltage of 9 V and -9 V the resulting built-in

field strength is 2.3 $V/\mu m$, which is far from the critical field. When used to ionise the excitons, the field generates a photocurrent on the scale of 10^{-60} A [38], concluding that the dominating mechanism of photocurrent in semiconducting carbon nanotubes is the phonon assisted exciton dissociation and not the regular build in field splitting of the exciton.

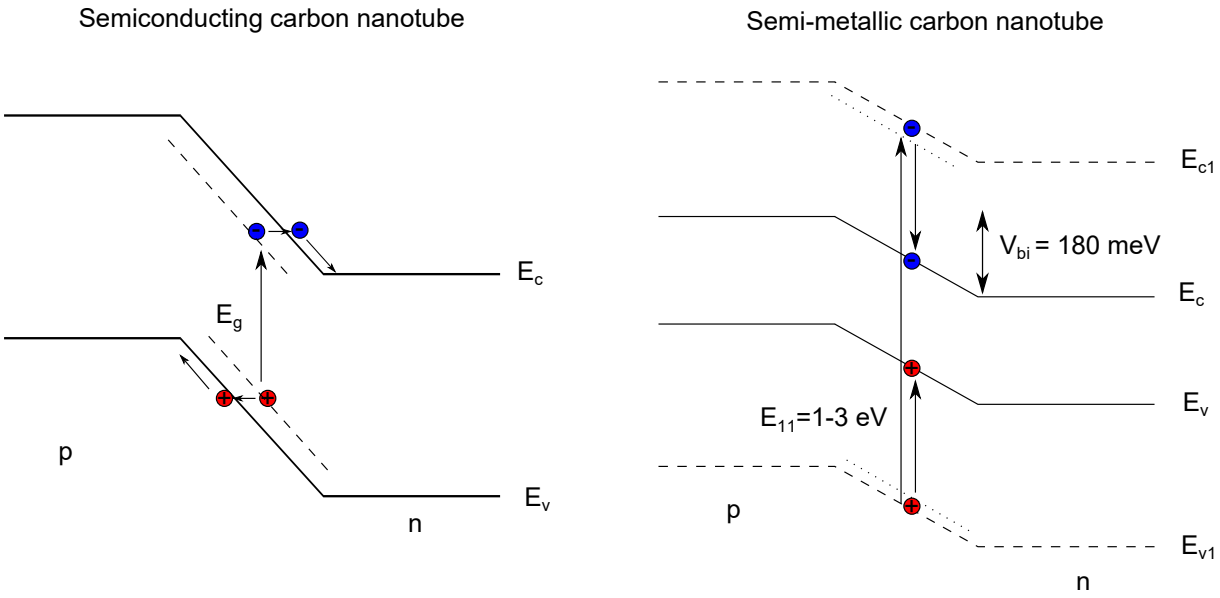

Figure 3.17: *Excitation mechanism in semiconducting and quasi-metallic carbon nanotubes. Inspired by [38].*

3.6.5 Quasi-metallic carbon nanotube photodiode

Considering the quasi-metallic carbon nanotubes it has been shown that they have a small band gap between 50 and 200 meV, where DFT calculations have confirmed band gaps of up to 170 meV. The energy differences are depicted in figure 3.17. The transition energy ($E_{11}^M = 1 - 3eV$ seen in figure 2.13) is larger than for the semiconducting carbon nanotubes. The amount of excitons contributing to the photocurrent per incident photon is 2 orders of magnitude higher than in the semiconducting carbon nanotubes [38], due to the required exciton-phonon coupling in the semiconducting nanotubes. For the semi-metallic nanotubes, the exciton binding energy is much smaller at $\approx$ 50 meV, and there are many available states which the electrons can enter. This makes the electron and hole able to decay to the conduction and valence band edges respectively. The built-in field will cause the electron and hole to split up spatially. The two main mechanisms responsible for quasi-metallic carbon nanotube photocurrent are the photovoltaic effect described above, and the photothermoelectric effect. The photothermoelectric effect is when a photon generates a temperature gradient causing electrons to diffuse from the hot region to the cold and this movement creates a current. For a non-photon generated temperature gradient this effect is called the Seebeck effect. The measured photocurrent (I_{pte}) from the photothermoelectric effect can be estimated by equation (3.20) [41].

$$I_{pte} = \frac{(S_2 - S_1)\Delta T}{R} \tag{3.20}$$

Where ΔT is the temperature gradient, R the resistance and the Seebeck coeficients (S_1, S_2) can be determined by equation (3.21), derived by M. Cutler and N. F. Mott [43].

$$S = \frac{-\pi^2 k_b^2 T}{3e} \frac{1}{G} \frac{dG}{dV_g} \frac{dV_g}{dE} \tag{3.21}$$

Here e is the elementary charge, T the temperature, k_b the Boltzman constant, G the conductance and E the energy. The resulting Seebeck coefficient will be different according to material properties and geometry. In conclusion it was determined that quasi-metallic carbon nanotubes can have a small bandgap and excitonic effects which are properties unique to carbon nanotubes. The photovoltaic effect is dominating for quasi-metallic nanotubes with a band gap above k_bT, while the photothermoelectric effect dominates for quasi-metallic nanotubes with a band gap $\leq k_bT$.

Raman spectroscopy

4

When photons are incident on a surface, several scattering and absorption events can occur. Most of the incident photons are scattered by Rayleigh scattering where the result is a photon with the same energy as the incident. The mechanism behind Raman spectroscopy is the Raman scattering event, wherein the exiting photon either has less or more energy than the incident photon. The first case, where the photon has less energy, is called Stokes scattering, and is much more probable than the case of anti-Stokes scattering, where the exiting photon has more energy. From conservation of energy, the energy lost or gained must come from the crystal. Often researchers use the frequency shift, also called the Raman shift (ω_K), to characterise the material. This is derived in equation (4.1) from the conservation of energy theorem. The s subscript denotes scattered photons, 0 incident photons and K the difference between these. [44]

$$\begin{aligned} E_s - E_0 &= E_K \\ \hbar(\omega_s - \omega_0) &= \hbar\omega_K \\ \omega_s - \omega_0 &= \omega_K \end{aligned} \tag{4.1}$$

From the equation it can be seen that the Raman shift is independent on the light source and as such it is easier to use. Furthermore, as the Stokes and anti-Stokes scattering have the same frequency, the Raman shift of these is equal in value, but with different sign.

The main issue with Raman spectroscopy is that, because it involves the vibrational modes of the crystal, the probability of a Raman scattering event is low compared to a Rayleigh scattering event. The probability of Raman scattering to Rayleigh scattering is on the scale of 1 to $10^6 - 10^{12}$. Furthermore the probability of Stokes to anti-Stokes scattering is proportional to $\exp(\hbar\omega_0/k_bT)$, and since in most systems the incident light is 2 orders of magnitude higher than the thermal energy, the probability of Stokes become much higher. Thus for any practical applications, a high laser intensity is needed and filters are required to quench the signal from Rayleigh scattering. [44]

4.1 Classical theory of light scattering for a molecule

An incident electromagnetic wave with electric field $\vec{E}$ on a material will cause it to become polarised, with a frequency equal to that of the incident field because of the redistribution of electron density, resulting in an induced electrical dipole moment ($\vec{P}$). A polarisability tensor α can be calculated for a material, denoting how easy it is to polarise. This tensor is defined in equation (4.2). [44, 45]

$$\begin{bmatrix} P_x \\ P_y \\ P_z \end{bmatrix} = \begin{bmatrix} \alpha_{xx} & \alpha_{xy} & \alpha_{xz} \\ \alpha_{yx} & \alpha_{yy} & \alpha_{yz} \\ \alpha_{zx} & \alpha_{zy} & \alpha_{zz} \end{bmatrix} \begin{bmatrix} E_x \\ E_y \\ E_z \end{bmatrix} \tag{4.2}$$

The incident electric field is defined as sinosoidal, and can be written as $E_i = E_{0,i}\cos(\omega t)$. Primarily due to thermal motion, each atom in a molecule or solid will vibrate around their equilibrium position with normal coordinates (Q) for a specific direction of vibration. α_{ij}, with ij being dummy coordinates to each entry in the matrix in equation (4.2), can be Taylor expanded around its equilibrium position, yielding equation (4.3). [44]

$$\alpha_{ij} = \alpha_{0,ij} + \sum_k \left(\frac{\partial \alpha_{ij}}{\partial Q_k}\right)_0 Q_k + \frac{1}{2}\sum_{k,l}\left(\frac{\partial^2 \alpha_{ij}}{\partial Q_k \partial Q_l}\right)_0 Q_k Q_l + ... \tag{4.3}$$

Where $\alpha_{0,ij}$ is the polarisability for the molecule at its equilibrium position, and Q_k is a displacement, which varies sinusoidally with time at a frequency ω_{vib}. It is defined as $Q_k = Q_{0,k}\cos(\omega_{vib,k}t)$. Several modes exist, denoted with subscripts k, l etc., and they can also have different vibrational frequencies. Taking only the first derivative of equation (4.3), it can be seen that the polarisability will also have a frequency component, as seen in equation (4.4), where only one component of the matrix equation is taken:

$$P_i(t) = \alpha_{ij}E_{0,i}\cos(\omega t) + \sum_k \left(\frac{\partial \alpha_{ij}}{\partial Q_k}\right)_0 Q_{0,k}\cos(\omega_{vib,k}t)E_{0,i}\cos(\omega t) \tag{4.4}$$

Using the identity $\cos(A)\cos(B) = 1/2\,(\cos(A+B) + \cos(A-B))$, equation (4.4) can be rewritten on the following form:

$$P_i(t) = \alpha_{ij}E_{0,i}\cos(\omega t) + \sum_k \left(\frac{\partial \alpha_{ij}}{\partial Q_k}\right)_0 Q_{0,k}E_{0,i}\frac{1}{2}\Big[\cos((\omega+\omega_{vib,k})t) + \cos((\omega-\omega_{vib,k})t)\Big] \tag{4.5}$$

From this it can be seen that the induced dipole moment will oscillate in many frequencies. Note that in equation (4.5), the first term is the Rayleigh scattering, the second term is the anti-Stokes scattering and the third term is the Stokes scattering. [44]

4.2 Normal modes and Raman activity

A normal mode is a vibrational mode of a molecule, usually called a phonon in the case of crystals. Normal modes of a non centrosymmetric molecule H_2O and a centrosymmetric molecule CO_2 can be seen in figure 4.1. To determine whether a mode is Raman active or not can be seen from the change in polarisabillity. If the change in the middle of the movement is zero then the mode will be inactive; this means the derivative of the polarisabillity at the equilibrium position of the molecule is zero for Raman inactive modes. Relating to the figure, in the middle of the movement for the CO_2 molecule it will reach its equilibrium position and thus this mode is Raman inactive. If the induced dipole moment changes sign through the equilibrium position the vibrational mode can be excited with infrared photons. For centrosymmetric molecules, Raman active modes and infrared active modes are mutually exclusive. [45]

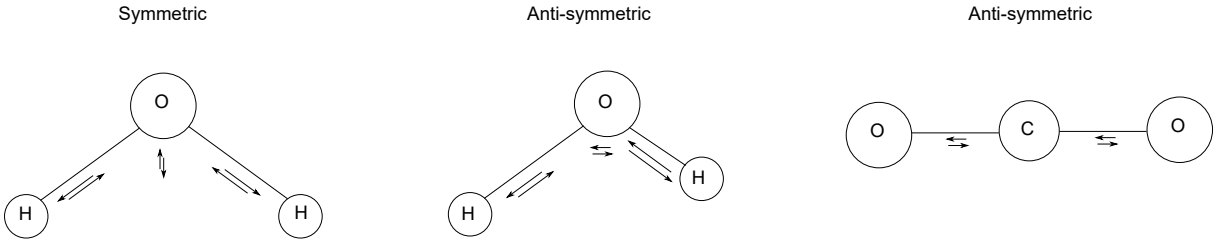

FIGURE 4.1: *Vibrational modes of a H_2O and a CO_2 molecule, where the symmetric stretching mode is Raman active, the anti-symmetric stretch mode and the anti-symmetric stretch mode of CO_2 is Raman inactive.*

4.3 Raman characterization of Carbon Nanotubes

In general there are four prominent Raman signals from carbon nanotubes, which are listed in table 4.1. These are the G- and G'-bands, the D-band and the radial breathing mode (RBM).

Feature	**Frequency (cm^{-1})**	**Cause**
G-band	1550-1605	Optical mode of graphite
RBM	$248/d_t$	Perpendicular radial displacement
D-band	1250-1450	Defect induced
G'-band	2500-2900	Overtone of D-band, diffuse

TABLE 4.1: *Common Raman features of carbon nanotubes, with d_t being the nanotube diameter. [46]*

The G-band is an optical Raman mode between the two carbon atoms, A and B, in the graphene unit cell (see figure 2.4). This band is present in carbon nanotubes as well, however it is not as well defined, due to the different geometry of the nanotubes compared to graphene. In graphene the G-band is always shown as a Lorentzian peak at 1582 cm^{-1}, while in carbon nanotubes it is shown as two peaks, referred to as G+ and G−. While graphene is two dimensional and symmetric, the curvature of the nanotubes as well as confinement of the phonon wave vector around the nanotube, lead to the longitudinal and transverse phonon modes becoming different from each other. The higher of the two G-band peaks (G+) is associated with the longitudinal optical phonon modes, whereas G− is associated with the transverse optical phonon modes. The location of these peaks can be used to characterize the nanotube diameter

and whether it is metallic or semiconducting, among other things. An example of the difference between graphite and carbon nanotubes can be seen on figure 4.2. [47]

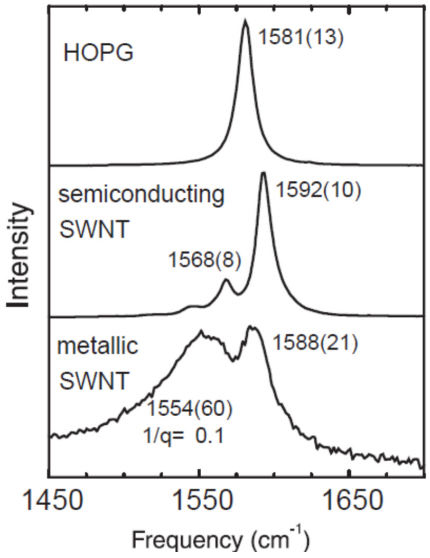

Figure 4.2: *Raman activity of highly organized pyrolytic graphite, semiconducting and metallic carbon nanotubes. Reprinted from Dresselhaus et al. [47]*

Since the G+ peak is a longitudinal optical phonon mode, it will be independant of the nanotube diameter. The G− peak is however dependant on the diameter, as well as whether the nanotube is metallic or semiconducting, as seen on figure 4.2. Neither of them are dependant on the chiral angle, so the G-band Raman peak can only be used to find the diameter of the nanotube, not the chirality. The diameter can be found from equation (4.6).

$$\omega_{G-} = \omega_{G+} - \frac{\varsigma}{d_t^2} \tag{4.6}$$

Where ω_{G-} and ω_{G+} are the frequencies of the G− and G+ bands respectively, d_t is the nanotube diameter and ς is a constant defined as 47.6 nm^2cm^{-1} for semiconducting nanotubes and 79.5 nm^2cm^{-1} for metallic nanotubes. For larger nanotubes the G-band peak will begin to resemble that of graphene. To get the nanotube chirality, the G-band data must be compared with the other Raman features, namely the RBM peak.

The RBM peak is a feature unique to carbon nanotubes, and thus is not found in graphene. It corresponds to a phonon mode around the nanotube, expanding and contracting as if the tube was "breathing". It is usually observed around frequencies ω_{RBM} of 120−350 cm^{-1} for nanotubes in the diameter range of $0.7\ nm \leq d_t \leq 2\ nm$. The diameter itself can be approximated from the frequency through the relation $\omega_{RBM} = A/d_t + B$, with A and B being experimental parameters. As an example, for single-walled nanotubes A=234 cm^{-1} and B=10 cm^{-1}. This method is however only useful for nanotubes with diameters in the specific range; smaller than this and ω_{RBM} becomes dependant on the chirality due to lattice distortions, and larger than this leads to weak Raman signals, bordering on undetectable.

The RBM peak can also be used for characterization of the chiral indices n and m of the nanotubes, though this method depends on finding the transition energy E_{ii} (see chapter 2.5). Through the resonance condition $E_L \approx E_{ii}$, with E_L being the laser energy, E_{ii} can be found with a tunable laser by looking for the energy in which the Raman signal has the highest intensity. With the diameter then known from ω_{RBM}, the chirality can then be found by comparing the two with figure 2.13. Often there will only be one type of nanotube which will be both within the diameter range and have the correct E_{ii}. This technique is well suited for characterising the chirality of single nanotubes, where the laser can be tuned to the correct energy. For multiple nanotubes one would have to tune the laser to the individual E_{ii} and characterize the nanotubes separately.

The last two features are the disorder induced D-band and the G'-band, its second-order overtone. These bands are the result of a resonance process between an electron and a phonon between the π and π^* states. These are once again features often found in graphene and other sp^2 carbons, but also contain some special features when found in nanotubes. They are furthermore highly dispersive, and their excitation frequency is heavily dependant on the laser energy. It originates from an in-plane transverse optic mode at the Brillouin zone boundary of graphene, around the K-point (see figure 2.6). The scattering process resulting in the D-band is as follows: an electron with momentum k absorbs an incoming photon, and thus becomes excited. It is then scattered by emitting a phonon with momentum q, gaining total momentum k+q. Afterwards it will be scattered back to recombine with the hole, returning to momentum k. One of these scattering processes, k$\rightarrow$k+q or k+q$\rightarrow$k, will be inelastic, emitting a phonon, and due to a defect in the graphene the other will be elastic, thus happening without a loss in energy. The G'-band originates from the same process, but does not include elastic scattering from a defect. As such the G'-band still exists in a perfect sheet of graphene, whereas the D-band only exists in graphene with defects or impurities. This means that the D-band intensity can be used as a measure for the amount of defects in a nanotube, usually presented as the ratio of D-band intensity to G-band intensity. While a useful tool for nanotube characterization, a higher D/G ratio does not directly translate into defect amount, eg. nanotubes with a D/G ratio of 5 does not have 5 times as many defects as those with a ratio of 1. Rather the ratio is dependant on the average distance between defects in the nanotubes, as proven by Dresselhaus et al, where it was shown that the highest D/G ratio occurred when the distance between defects were 4 nm. [48]

Production of carbon nanotubes

5

5.1 Chemical vapour deposition of carbon nanotubes

Multiple methods exist to grow carbon nanotubes, but chemical vapour deposition (CVD) stands as a simple and reliable method for growing large quantities of long nanotubes, with lengths ranging from a few micrometers and up to millimetre scale. Given the right conditions, all that is needed for growth is a suitable catalyst material to initiate growth and a carbon source, typically in the form of a hydrocarbon. The technique is advantageous compared to eg. arc-discharge or laser ablation in that it gives both higher yield and purity of nanotubes, while also giving limited control over the morphology.

The general setup required for CVD usually consists of a cylindrical chamber which houses the substrate. The substrate itself has been coated with a catalyst material consisting of metal- or metal oxide nanoparticles. The chamber is kept at high temperature (600-1200 °C), and the sample is exposed to the carbon source for up to an hour, depending on the desired length of the nanotubes. Apart from the carbon feedstock, usually a flow of inert gas (eg. Argon) is present in the chamber, to displace any air inside. During the growth process hydrogen is often added to the chamber, to catch the released oxygen from the sample or oxide nanoparticles. With regards to the carbon source, it can consist of either a solid, liquid or gaseous source. A carbon gas can be directed through the chamber with the argon gas, and a liquid carbon source can be distributed by bubbling the argon gas through it. For a physical carbon source, it should be placed near the center of the chamber, since the high temperature should cause it to diffuse down upon the substrate.

The actual mechanics of carbon nanotube formation are still debated. The most popular theory however, is that the carbon is dissolved in the metal nanoparticles, which should be kept molten during the growth period. When the nanoparticles are saturated, the dissolved carbon begins to precipitate and form the more stable nanotube structure. Depending on the binding strength of the catalyst to the underlying substrate, two different growth patterns are observed. If the interaction is strong, the nanoparticle remains anchored to the substrate, and the nanotube will grow out from the top part of the particle. If the interaction is weak however, the nanotube will be formed below the particle, and lift the entire particle away from the surface, with the nanotube acting as the anchor. These growth mechanics are called base-growth and tip-growth respectively. The size of the nanoparticles also have an influence on the nanotubes, with large particles, tens of nanometres in diameter, usually growing multi-walled carbon nanotubes, and smaller particles, a few nanometres in diameter, usually growing single-walled.[49, 50]

5.1.1 Substrate effects

The choice of substrate to grow the nanotubes on can greatly influence the quality of the final product. While carbon nanotubes have often been grown on a silicon substrate, studies have shown that nanotubes grown on crystalline quartz, cut along certain crystallographic edges, exhibit a high degree of alignment. A study by Kocabas et al [51] proved this, by attempting to grow quartz on both X-, Y- and Z-cut quartz wafers. The nanotubes grown on the X-cut wafers showed no preferred growth direction, while Z-cut seemingly had 3 directions. Y-cut quartz however was shown to only have a single preferred growth direction, and when CVD was performed with flow along this direction, the result was perfectly aligned carbon nanotube arrays with seemingly no overlap. Even when grown perpendicular to the preferred direction, the nanotubes would still try do align themselves after it, resulting in a zigzag pattern of nanotubes trying to place themselves in the preferred growth spots. The precise mechanics of these preferred growth directions are however not fully understood. The most prominent theory seems to be that the tubes either prefer to grow along step edges, or some rectifying anisotropic interaction energies between the surface and nanotubes for certain cuts. These mechanics are however still up for debate. Often, instead of using Y-cut wafers, a special cut called ST-cut will be used instead, yielding a surface close to that of Y-cut, but with included steps along the surface. This cut can be seen in figure 5.1. [51, 52]

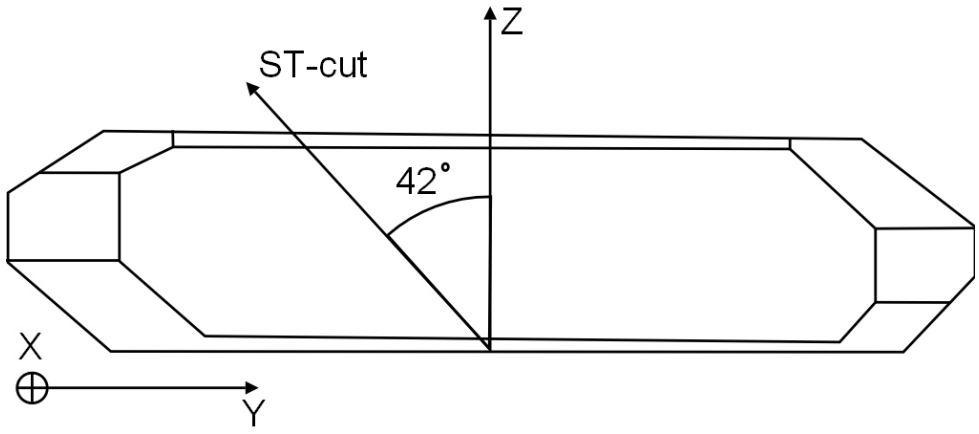

Figure 5.1: *Crystallographic directions of quartz with ST-cut angle indicated. Inspired by figures from MECquartz [53]*

5.1.2 Choice of catalyst material

Experiments by Yuan et al. [52] showed that the choice of catalyst material also influences the quality and alignment of the grown nanotubes on quartz substrates. While classically iron, cobalt or nickel nanoparticles have been used, his group experimented with other materials, including manganese, palladium and platinum nanopaticles. Iron, cobalt and nickel are usually chosen for their high solubility of carbon, however most transition metals often prove decent catalysts for carbon nanotube growth. [49] While noble metals (Cu, Ag, Au, Pd etc.) have a relatively low carbon solubility, they work well as catalysts as long as the nanoparticles are sufficiently small. The size of the nanoparticles are dependant on the growth method and especially the growth temperature, which is usually at several hundred degrees Celsius.

Non-metallic nanoparticles can also be used as catalysts, such as nano diamonds and metal oxides. Nano diamonds are made of carbon, so carbon cannot be dissolved in them; as such the

exact mechanism as to how nanotubes are grown from these is poorly understood, but carbon nanotubes have been grown and characterised regardless. Using oxide nanoparticles as catalysts also proves that certain materials, eg. Si and Ge, which have poor catalytic properties as pure nanoparticles, worked well in their oxide form.

Finally a novel technique was created by Yuan et al. [52] to create metal particles of steel and tungsten carbide suitable for nanotube growth. By using a steel blade and cutting a line on the hard quartz wafer, they found that aligned nanotube arrays could be grown from the metal residue left behind from the blade. This method can as such be used as a simple, if crude patterning process, without the need of high temperatures for nanoparticle growth.

5.2 Arc discharge

Arc discharge was the first method used by Iijima to synthesize nanotubes in 1991, and it has proven a valuable technique in the production of high quality nanotubes. The general setup can be seen on figure 5.2. The process takes place in an enclosed chamber filled with either liquid or gas, which can be ignited into a plasma by a strong electric field between the electrodes. The cathode usually consists of a rod of pure graphite, while the anode is filled with powdered carbon as well as a catalyst material. To grow the nanotubes, the electrodes are brought in contact to form an electrical arc between them, and are then kept a few millimetres apart for the growth process. The resulting plasma reaches temperatures between 4-6000 °C, which causes the carbon and catalyst to sublimate. The gaseous carbon is converted to carbon ions and drift towards the cathode due to a temperature gradient, where it cools down to liquid carbon. This liquid carbon will then crystallize into cylindrical carbon nanotubes, which grow out from the cathode. Depending on the stability of the arc, the quality and purity of these nanotubes may vary greatly. The main problems with this technique is the high temperatures needed to create the carbon nanotubes, as well as the result being a bundle of nanotubes that can be difficult to separate. On the other hand, these high temperatures generally result in nanotubes with fewer structural defects.

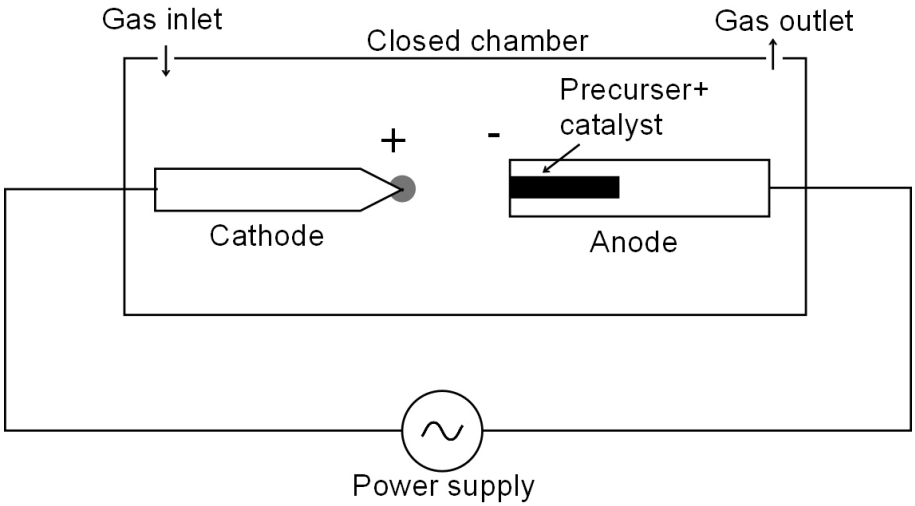

FIGURE 5.2: *Schematic of typical set-up for production of carbon nanotubes through arc discharge.*

There are three ways of operating the setup, depending on the power source used. If the system is run with a DC current, the yield is high due to the continuous stream of electrons hitting the anode at all times. By making the cathode larger than the anode, the cathode will then be cooler, and the resulting temperature gradient means that the hot gaseous carbon will flow towards the cathode. The problem is that the ionized gas is attracted to the negatively charged cathode, where it will hinder the continuous deposition. Alternatively an AC current can be used. Here due to the alternating current, there will be no build-up of carbon on either electrodes, and the carbon gas will simply flow outwards and be deposited on the cold walls of the chamber. The yield will however be lower, since carbon will only be released from a positive cycle. A third method is to use a pulsed current to prevent the build-up of the ionized gas. Here short pulses on the scale of milliseconds are sent from cathode to anode, which will vaporize the carbon in the anode, which will then be deposited on the cathode. Generally this is the most favourable method for arc discharge production of carbon nanotubes.

Generally production of carbon nanotubes through arc discharge will result in multi-walled carbon nanotubes, unless specific conditions are met. Firstly there is the choice of catalyst material; if no catalyst material is used, it will result in multi-walled carbon nanotubes, whereas single-walled carbon nanotubes are usually grown from transition metals like Fe, Ni or Co, which are mixed with graphite in the anode. During the growth the electrodes should furthermore be held at a constant distance to ensure a stable arc. While this method will produce single-walled carbon nanotubes, there will also be produced a significant amount of multi-walled nanotubes and fullerenes. It is possible to refine the production to around 90% single-walled nanotubes, by using an argon/hydrogen atmosphere with an iron catalyst. [50, 54]

5.3 Laser ablation

The principles of laser ablation once again involves the evaporation of a carbon precursor along with a catalyst material, however instead of using a plasma, a pulsed laser is used instead. The setup used can be seen in figure 5.3. A graphite target is placed in a furnace at a high temperature (around 1200 °C) in an inert gas atmosphere. A high intensity laser is then aimed at the graphite target, which is then vapourized. The carbon will then condense on the cooler surfaces of the furnace. To better collect the resulting nanotubes, a water cooled copper rod is inserted near the end of the chamber. Due to this rod being cooler than the rest of the furnace as well as the gas flow towards it, the vaporized carbon will be deposited here in the form of soot containing nanotubes.

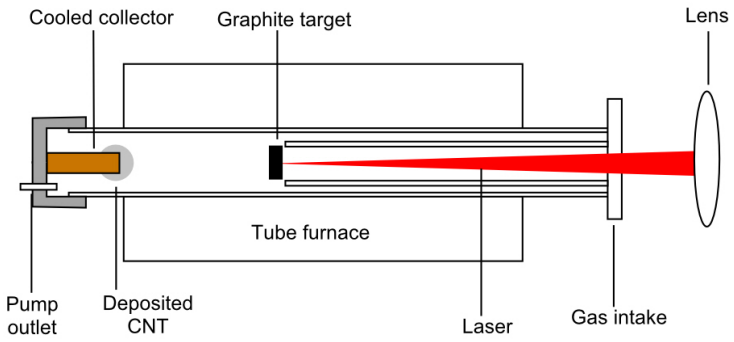

Figure 5.3: *Typical set-up for laser ablation production of carbon nanotubes. Inspired by Chrzanowska et al. [55]*

As with the arc-discharge method, catalyst materials can be added to the graphite target to increase the nanotube growth. This method also produces nanotubes with a relatively high purity (>70%). It does however also have the same problems, with the resulting nanotubes being highly entangled. In addition neither method is very cost effective, with both requiring large amounts of purified graphite as targets, and both requiring large amounts of energy for the nanotube production. As such, neither method is well suited to produce carbon nanotubes on an industrial scale. [50, 56]

6 Experimental

6.1 Production method of aligned carbon nanotubes

The production method was inspired by an article by Zhou et. al. [57]. Two types of wafers were prepared as growth substrates, silicon and ST-cut quartz. The wafers were cleaned with a three part process using ultrasonication in acetone, de-ionized water and ethanol for two minutes in each, and were subsequently dried using nitrogen. After cleaning the wafers they were spin coated at 3000 rpm for 45 seconds with a photoresist containing 5 mmol iron chloride. The wafers were baked at 110 °C for 1 minute to evaporate any water on the wafer and solidify the photoresist. The next step would be the patterning process, if the wafers required patterning, and here two different methods were used. The first was a simple mask with macroscopic lines; this pattern was only used as a proof of concept, to see if nanotubes would be left to grow only in the non-developed areas, since this method was a lot quicker than the alternative. The wafers were then exposed to UV light for 90 seconds, after which they could be developed. The second method was the direct-write method, which will be described later in chapter 6.2. An alternative method was later utilised, involving dissolving the iron chloride in pure ethanol instead, and either spin- or dip-coating the wafers with the solution. While no patterning could be made with this method, it proved a good alternative to the resist-based method.

The wafer is then inserted into a preheated carbolite furnace oven at 720 °C. This step is done to evaporate the photoresist, and create iron oxide nanoparticles. The iron chloride reacts with oxygen in the air and makes Fe_xO_x nanoparticles. The quartz wafers were inserted during the heating of the oven as they would otherwise crack due to rapid thermal expansion.

For the growth of carbon nanotubes with CVD, the wafer was placed inside of a 1.5 inch diameter tube furnace. The chamber was purged with argon to remove any oxygen in the chamber, followed by a 500 sccm argon flow for the growth. The exit of the furnace was water cooled to avoid any high temperature gas escaping. The furnace was then heated to 920 °C and 84 sccm hydrogen flow was introduced to remove any excess oxygen while turning the iron oxide nanoparticles into pure iron nanoparticles. Then a methane flow was introduced to act as a carbon source for the nanotubes. After growth had ended, the methane flow was shut down and a small hydrogen flow was left along with the argon flow while the furnace cooled down. After the furnace had cooled down below 500 °C, the hydrogen flow was turned off and the argon flow was reduced. When the wafer was taken out a lot of black soot could be seen in the middle of the glass tube where the wafer was placed. A small difference in the reflectance could be seen with the naked eye in agreement with the developed pattern.

Materials

- Silicon wafers - Crystalline, [100] direction
- Quartz wafers - Crystalline, ST-cut
- Photoresist - Shipley 1813 positive resist
- Iron(|||) chloride - Anhydrous
- Developer - Microposit developer Ma-D 331
- Argon gas tank
- Methane gas tank
- Hydrogen gas tank
- 99 % Ethanol
- Acetone
- Deionized water

Equipment

- Electrical carbolite oven - Eurotherm CSF 1200
- Pipe furnace
- Mass flow meter
- Spin coater - WS-65-23NPP/C2/IND
- Prebaking oven - Präzitherm type 2860 EB
- Ultrasonic bath - Powersonic from Martin Walter

6.2 Direct write system

Multiple parts of the production routine requires the use of photolithography, both for growth of the iron oxide nanoparticles, and for placing metal contacts at the ends of the nanotubes. Though this could be accomplished using masks, the method used was instead to rely on a direct write system using a 400 nm UV laser. The general setup can be seen on figure 6.1.

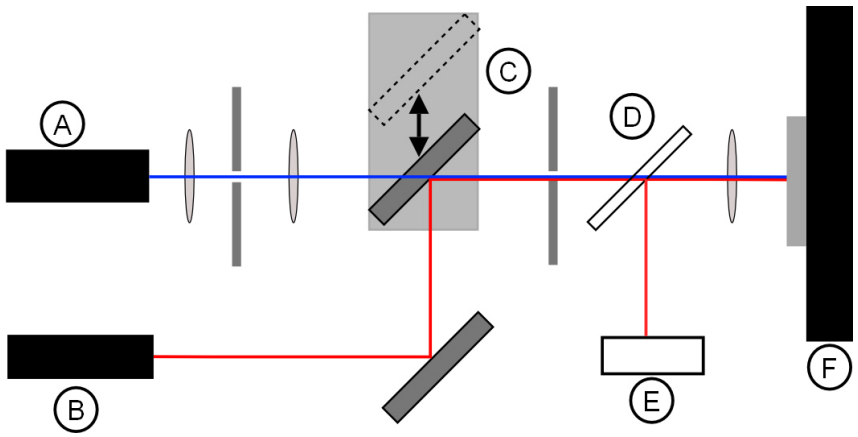

Figure 6.1: *Direct write setup. A) New Focus Model 3941 400 nm laser. B) JDS Uniphase Model 1125 633 nm laser. C) Adjustable mirror, to regulate whether red or blue laser hit the sample. D) Removable beam-splitter that can be inserted to reflect backscattered light from the laser onto E) a simple beam blocker inserted to see that the reflected light is still in focus. F) Sample mounted on remote controlled xy-stage*

Two different lasers are used in this setup, a red 633 *nm* laser and a blue 400 *nm* UV laser. The UV laser is used to expose the photoresist, which the red laser cannot; this makes the red laser ideal for focusing. Since the sample is not necessarily planar when mounted, the tilt of the

holder can be adjusted to ensure that the laser is in focus everywhere on the sample. The setup has been calibrated so that if the red laser is in focus on the sample the UV laser will also be. To ensure that the laser is focused, the backscattered light can be reflected onto another target using the beam-splitter; if the laser is focused on the alternative target, it will also be focused on the sample. For the actual writing process, the adjustable mirror is slid aside to make way for the UV laser. Where on the sample the UV laser hits can then be controlled through the xy-stage. Both the blue laser and the xy-stage can be controlled from a nearby pc using an Arduino program, and a program was written in Matlab to produce schematics for the writes; this program is included on the disc.

Since at least two separate writes had to be done on each sample (one for iron oxide nanoparticles and one for contacts), and since the sample could not be placed in the exact same position every write, a method was needed for aligning the sample. As such three spots were written on the surface with known position in the defined coordinate system; after coating with chrome, these could then be found with the xy-stage. By knowing their initial coordinates in regards to the defined coordinate system, and finding their new coordinates at the next writing process, the points in the subsequent write could then be rotated and shifted to fit the new position of the sample. These spots would then be written on each sample first, leading to three writes in total for every photodetector.

6.2.1 Matlab code for direct write setup

The stage control program operates based on coordinates that can be fed in from a .lit file; a Matlab program was written to generate these coordinate systems. For every point to be written, four numbers were fed in: the x and y-coordinate of the given point, as well as the shake time (how long the stage takes to verify its position at every point) and the exposure time, both in microseconds. Regarding the x- and y-coordinates, it was found that the distance between two points (eg. x and x+1) was on the scale of 1/6.5 μm; this was taken into account when defining the structure. Dimensions of every part of the structure are defined in μm, and are then scaled up with 6.5 to match with reality. Precision down to 1/6 μm could however not be achieved, since the spot size of the used laser was on the scale of 3 μm.

Furthermore the program needed functionality to allow for multiple writes on the same sample. This was achieved by including three calibration points, which could then be found during subsequent writing processes. The main structure, as well as the three calibration spots, are all defined with regards to their "south-eastern" most coordinate, and the program was set up in a way that allowed for the rotation and displacement of all coordinates, as long as the coordinates of two alignment spots were known. The points used for alignment are P_1 and P_2, as seen on figure 6.2.

P's are coordinates, V's are vectors, O is the origin which all points are defined with relation to, and subscript r denotes coordinates and vectors in the rotated coordinate system. The coordinates for P_1, P_2, P_3 and O are known beforehand. When performing the second write, the coordinates for P_{1r} and P_{2r} are found manually, and can be inserted into the program. Since they are each large squares, the coordinate used is the one for the "south-eastern" corner. P_{3r} is found by rotating V_{12r} clockwise 90°. From this the rotation of the new coordinate system can be found from the angle θ between V_{12} and V_{12r}. The vector V_{Or} is then found by rotating V_O by θ. With V_{Or} the origin O_r can be found in the new coordinate system. The distance between O and O_r is then calculated as the general displacement of all coordinates. As for the rotation of

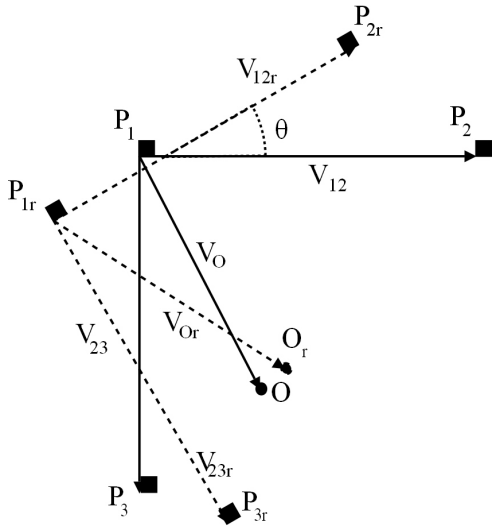

Figure 6.2: *Coordinate systems used for alignment process. Dashed lines and subscript r are used to denote coordinates and vectors in the rotated coordinate system.*

the coordinates, this is handled through finding the slope (a_{xcal} and a_{ycal}) of the lines between P_{1r} and P_{2r}, and P_{1r} and P_{3r}. To transform a coordinate from the original coordinate system to the rotated one, the following transformation is made. Primed coordinates are coordinates in the rotated coordinate system.

$$a_{ycal} = \frac{y(P_{2r}) - y(P_{1r})}{x(P_{2r}) - x(P_{1r})}$$
$$y' = a_{ycal}x + y \tag{6.1}$$
$$a_{xcal} = \frac{y(P_{3r}) - y(P_{1r})}{x(P_{3r}) - x(P_{1r})}$$
$$x' = a_{xcal}y + x \tag{6.2}$$

This method is fundamentally just a linear regression. Finally the distance between any given point in either the x or y direction must be modified with the following factors:

$$dist_x = \frac{x(P_{3r}) - x(P_{1r})}{x(P_3) - x(P_1)} \tag{6.3}$$
$$dist_y = \frac{y(P_{2r}) - y(P_{1r})}{y(P_2) - y(P_1)} \tag{6.4}$$

Using these four factors it is then possible to rotate the coordinate systems in Matlab to fit with the altered position of the sample. Figure 6.4 shows an example of a rotated coordinate system, with the spots from the original coordinate system included in blue. The new .lit file can then be loaded into the program prior to the write process.

Using this method the size of entire structure remains the same, while the structure as a whole is displaced and rotated. With proper alignment, this method makes it possible to write multiple times on the same wafer with micrometre precision.

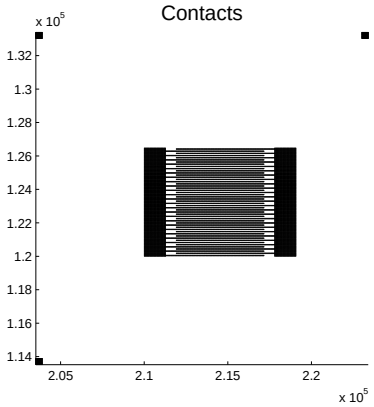

FIGURE 6.3: *Normal coordinate system*

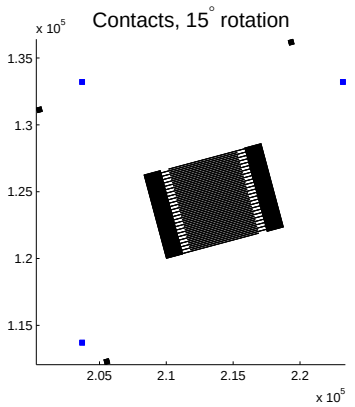

FIGURE 6.4: *Rotated coordinate system.*

6.3 Exfoliation and debundling of carbon nanotubes

Carbon nanotubes are very hydrophobic, hence they bundle up when dissolved in water. As such a method was needed to separate them and deposit them on a substrate. The method used for this was modelled after the suggested parameters from Sigma Aldrich [58].

A stock solution of 2 mg/ml sodium cholate hydrate in water was prepared and 1-2 mg of carbon nanotubes are prepared per 7 ml of sodium cholate solution. An alternate stock solution of 2 mg/ml Triton X-100 and 1-2 mg of carbon nanotubes was also prepared for comparison. Both sodium cholate and Triton X-100 are surfactants, meaning that they have a hydrophobic end which binds to the nanotubes, and a hydrophilic end that binds with the water. The diluted nanotube solution was ultrasonicated for 1 hour, where after the solution turned from a transparent liquid with small black flakes into a semi-uniform black solution. It was then centrifuged at 14000 g for 30 minutes, and the supernatant is extracted cautiously to avoid the bundles, which cluster up in the bottom after centrifugation.

6.3.1 Deposition of exfoliated nanotubes on substrates

After exfoliating the nanotubes, a few droplets are pipetted onto a clean quartz or silicon wafer, and heated in an oven with ambient atmosphere to 300 °C for 30 minutes to remove water and evaporate any excess Triton X-100 according to data from Mitsuda et. al. [59]. For the sodium cholate solution, the samples were annealed at 250 °C for 1 hour as mentioned by Sim et. al. [60]. For all of these measurements the carbon nanotubes from mkNANO with 98% purity has been used.

For the current-voltage measurements, chrome or aluminium contacts were patterned with the direct write system, and sputter coated to a thickness of 40 nm. The separation between the electrodes was varied between 15 μm and 20 μm. On figure 6.5 the patterned interdigital electrodes with carbon nanotubes on top can be seen. The nanotubes were deposited on the contact according to the same annealing method mentioned above. The photocurrent mechanics of this design with an MSM configuration is described in chapter 3.5. A cross sectional view can be seen in figure 6.6 where the lines on top illustrate a random mat of carbon nanotubes.

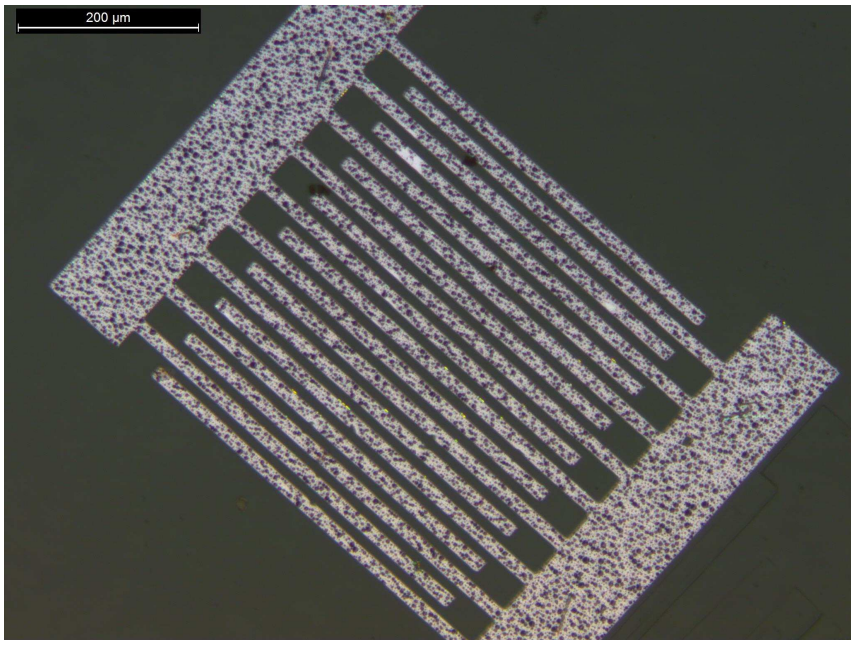

Figure 6.5: *Overview of a sample to be used as a photodetector with 20 µm separation and aluminium electrodes with carbon nanotubes clustered together ontop.*

6.3.2 Gated carbon nanotube photodetectors

A silion wafer with a 600-700 nm thermally grown SiO_2 layer on top is utilised for the gated photodetector design. First a small layer is polished off the bottom to remove the oxide layer and create electrical contact to the silicon. Similarly to the previous design, interdigital electrodes are patterned and coated with a 40 nm layer of aluminium. The photocurrent mechanics of this design are described in chapter 3.6.2 and a cross-sectional view can be seen in figure 6.7, where the gate potential is applied to the bottom side of the silicon wafer.

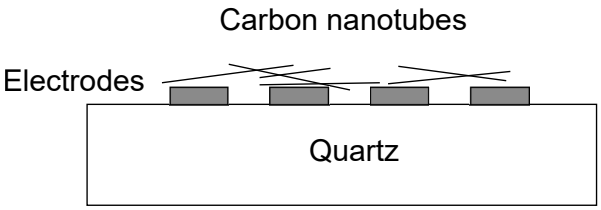

Figure 6.6: *Cross sectional view of MSM photodetector.*

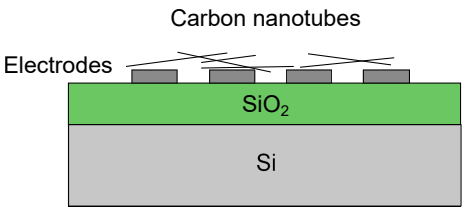

Figure 6.7: *Cross sectional view of gated photodetector.*

Materials

- Sodium cholate hydrate
- Triton X-100
- Deionised water
- Single-walled carbon nanotubes, Cheap tubes inc. >90 wt% purity
- Single-walled carbon nanotubes, mkNANO >98 % purity
- Silicon wafers - Crystalline, [100] direction
- Quartz wafers - Crystalline, ST-cut

Equipment

- Scales, Ohaus discovery
- Ultrasonic bath, Branson 2510
- Centrifuge, Eppendorf centrifuge 5804 R
- Absorbance spectrometer, WWR international UV 1
- Pipette, Eppendorf research 1000 μL
- Quartz cuvette
- Sputter coater, Scientific vacuum systems
- Developer - Microposit developer Ma-D 331

6.4 Characterization methods

6.4.1 Scanning electron microscopy

Scanning electron microscopy (SEM) measurements were performed with either an Zeiss EVO 60 SEM or a Zeiss 1540 XB SEM, depending on the quality of the required images. For samples with a silicon substrate, the samples could be inserted normally, but since quartz does not conduct electricity, they had to be coated with a conductive material. A thin gold film at 10-15 nm was chosen for this purpose. The surface of the wafer was connected to the sample holder with copper tape to lead charges away.

6.4.2 Raman setup and measurements

The samples were prepared as described in chapter 6.3.1 for the purchased carbon nanotubes and in chapter 6.1 for the produced carbon nanotubes. An argon-ion laser was used and filters were inserted in order to single out the 484 nm (2.56 eV) line, as this line had a high intensity. The laser beam was focused onto the sample with an optical microscope with an 100x objective. For the measurements of the RBM-modes, which are located between 100-350 cm^{-1}, a cut-off filter Notch 488 nm had to be removed. This unfortunately resulted in some signal from the laser. The power from the laser was not consistent, so the sampling time was changed between 120 to 180 seconds to get a proper signal. The detector has a few pixel errors which result in spikes of single data points, and should not be regarded as a peak from the sample.

6.4.3 Absorbance spectra

The experimental absorbance spectra were performed with the pipetted solution and for most of the samples they were not diluted further, as an absorbance below 1 was observed for the samples. The sodium cholate stock solution was used as the reference. All absorbance spectra were measured from solutions with carbon nanotubes from Cheap tubes inc. To find the peaks, a 5th order polynomial fit is withdrawn from the data; this was chosen because a 5th order polynomial is chosen because it does not create additional peaks.

6.4.4 Atomic force microscopy measurements and image correction

All atomic force microscopy (AFM) data were taken in semicontact mode with a NT-MDT AFM. All images have a polynomial background withdrawn in the vertical and horizontal direction unless stated otherwise. Most of the polynomials are first order, but for large images (length and width $>10\ \mu m$) a second order polynomial better erases the background, as local hills may be present. The images have den undergone median line correction, to ensure that any error that may arise from line shifts are corrected.

6.4.5 Current-voltage measurements

Once the carbon nanotubes have been deposited on the electrodes. A four point probe technique is used, where the voltage and current probes were attached onto the electrodes by looking through a microscope. Very little current is going through the voltage probes and thus the measurement is more accurate. The positive and negative probe were connected oppositely to each other, on different bases of the interdigital electrodes as seen in figure 6.8. Note that the blue circle indicates blue laser light used for measuring the photocurrent of the MSM photodetector design. An ampere meter is connected in series to a current source and the current is varied between -100 to +100 nA, for weakly conductive samples and up to $\pm$ 100 μA for highly conductive samples. In order to have the voltage probes to give a stable readout. On some of the measurements a small deviation can be observed when beginning measurements, because the equipment need to stabilise. The resistance of the non-linear measurements was determined as described in chapter 3.5.1, by taking the reciprocal of the slope in the high voltage region.

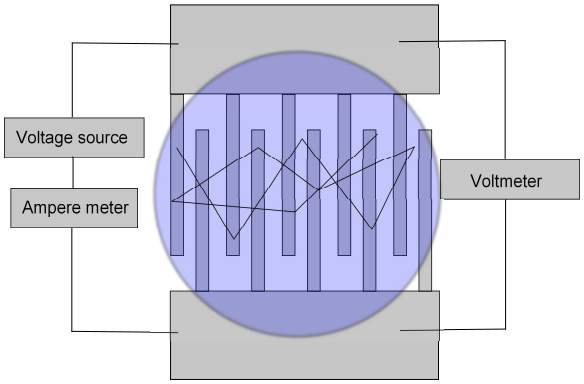

Figure 6.8: *Top view of the schematics for current-voltage curves.*

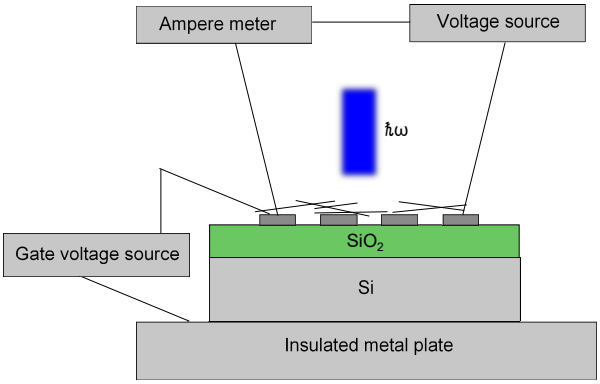

Figure 6.9: *Cross sectional view of method for measuring photocurrent.*

6.4.6 Photocurrent measurements

For the photocurrent measurements a collimated laser beam is sent through an optical fiber cable into an optical microscope with an objective to focus the beam onto the sample. The spot size is approximately 0.5x0.5 mm^2, which covers most of the contacts. For the MSM photodetector design two tungsten probes are connected to a voltage source, with a voltmeter in parallel and an ampere meter in series, to measure the current and subsequently the photocurrent. Two voltage probes are connected to the sample to ensure that the applied voltage is correct. The applied voltage was tested in a range from -9$-$0 V.

For the gated design of photodetectors a similar method is used, seen in figure 6.9. Note that only the gated detector's photocurrent is measured in this way. The voltage probes are

swapped to gate voltage applied to a insulated metal plate in contact with the bottom of the silicon wafer, and with the other end connected to the the positive side of the applied bias. This is done to ensure that an electric field is applied from beneath the carbon nanotubes mat. Again the applied voltage is tested in the range -9−0 V, with a gate voltage ranging from -30 to +30 V.

Equipment

- Laser 451 nm, blue, 20 mW
- Laser 531 nm, green, 20 mW
- Keithley 6487 picoammeter/voltage source
- Keithley 6221 DC and AC current source
- Keithley 6517A electrometer/high resistance meter
- Keithley 2182A nanovoltmeter
- Four point probe station in Faraday cage with attached microscope

6.4.7 Electrical breakdown of quasi-metallic carbon nanotubes

In order to improve the photocurrent, a process named electrical breakdown to remove the quasi-metallic carbon nanotubes was proposed by Zeng et. al. [33]. The removal process involves incinerating the quasi-metallic tubes though Joule heating. The idea is that most of the current is running through the quasi-metallic tubes, leading to them being heated and incinerated before the semiconducting nanotubes. As single carbon nanotubes are not detectable with an optical microscope, the current was upped in magnitude until either the resistance changed or large red spots appeared in the optical microscope. The four point probe station described above was utilised for this purpose.

7 Results

7.1 Characterization of quartz surfaces

The surface of ST-cut quartz has been described in literature as having a rectifying effect on nanotubes grown on it. To get an idea on the topography of the surface and possibly see the reasons for this mechanism, clean quartz wafers were examined with AFM and Raman spectroscopy. Figures 7.1 and 7.2 show the topography of a clean ST-cut quartz wafer before and after annealing at 900 °C in air for 12 hours. Both surfaces contain valleys with depths of 1-1.5 nm in the same direction. The Root-Mean-Square (RMS) surface roughness for the clean sample is 0.668 nm and 0.811 nm after annealing.

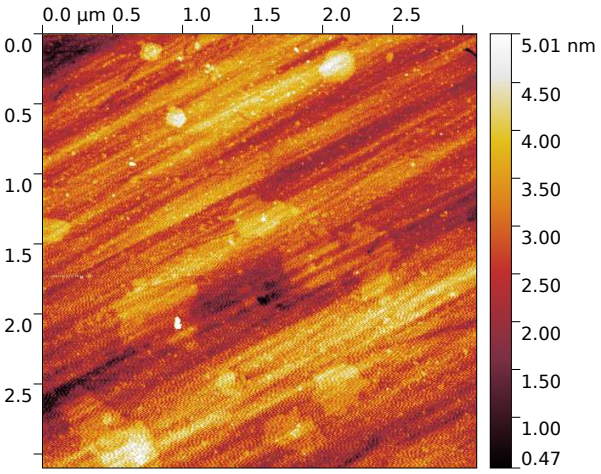

FIGURE 7.1: *AFM-topography of ST-cut quartz wafer.*

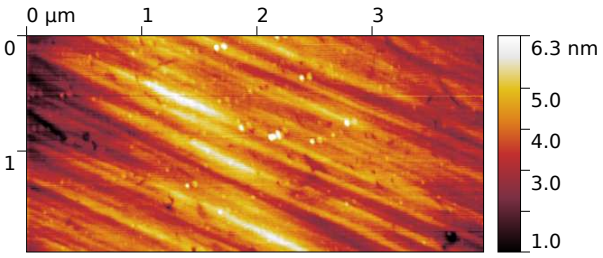

FIGURE 7.2: *AFM-topography of ST-cut quartz wafer annealed for 10 hours.*

The clean quartz wafers were furthermore studied with Raman spectroscopy, and the resulting spectra can be seen on figure 7.3. Note that the slope of the data is due to the frequencies approaching the laser line. Four features are visible in the spectrum, a large peak at 465 cm^{-1}, two smaller peaks at 205 cm^{-1} and 358 cm^{-1}, and a slight peak at 256 cm^{-1}. The peaks at 465 cm^{-1} and 256 cm^{-1} indicate α-quartz and the peak at 205 cm^{-1} is from a cut-off filter close to the laser line which was deduced as it follows the grating.

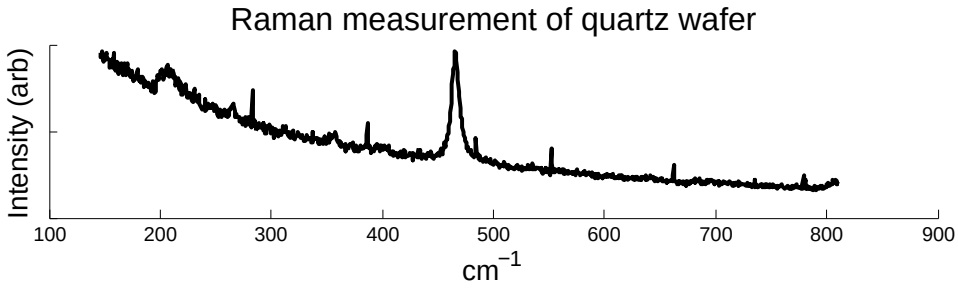

Figure 7.3: *Raman spectra of a clean unannealed quartz wafer. Slope of the data is due to the frequency approaching the laser line of the setup.*

7.2 Characterisation of nanoparticle growth

A few different methods were used to produce iron nanoparticles on either quartz or silicon substrates. The samples were subsequently examined using AFM, to get a measure of their size. All samples were measured before nanotube growth, and as such the nanoparticles are made of iron oxide.

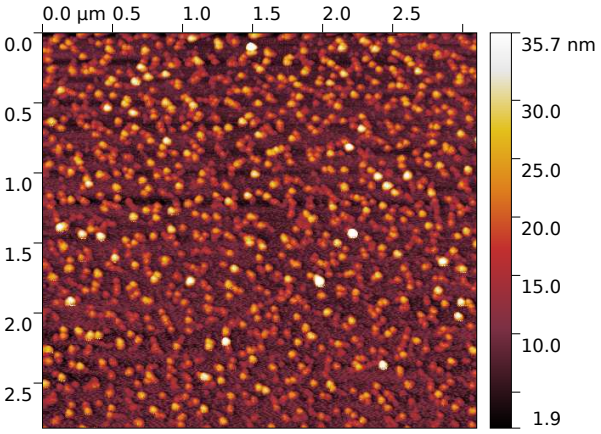

Figure 7.4: *AFM-image of FeO nanoparticles, heated at 700 °C.*

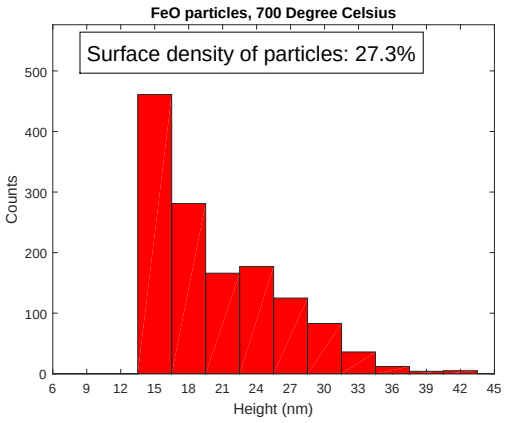

Figure 7.5: *Histogram of particle sizes, calculated surface density.*

Figure 7.4 shows an AFM-image of the ironoxide nanoparticles used to catalyse the growth of carbon nanotubes. As seen on the image the surface density is quite high, and from the particle analysis seen in figure 7.5, the main particle size is registered at 15-20 nm, with a few very large particles strewn in. All of the particles appear circular in shape.

Figure 7.6 shows the border between an area with nanoparticles grown from the FeCl/photoresist solution, and an area where the resist was exposed and removed. The particles have been grown at 700 °C. It can be clearly seen that the nanoparticles surface density is a lot higher in the area with the photoresist than in the exposed area, proving that the photoresist solution is a good method for selective growth of nanoparticles.

Since the nanoparticle size can have an influence on the quality and type of nanotubes grown from them, multiple experiments were made to see whether different growth parameters would have an influence on the resulting nanoparticles. The results from these tests can be seen in table 7.1. All tests were made with the FeCl/photoresist solution.

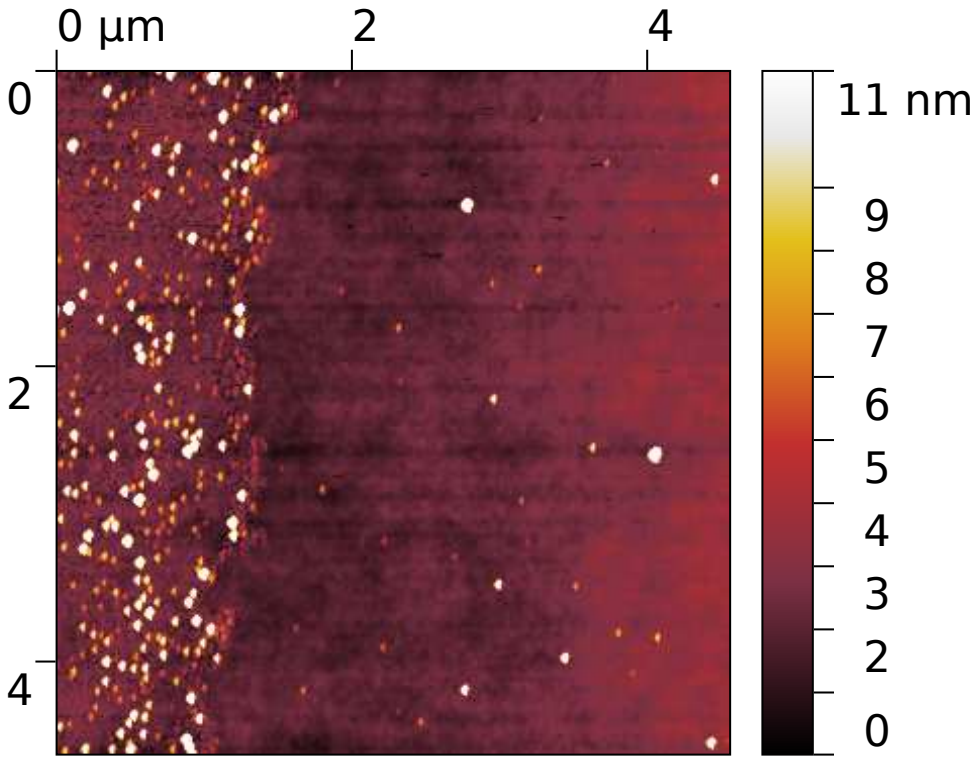

FIGURE 7.6: *AFM image of the boundary from developed area to the non developed area. Note that the white particles may be larger than 11 nm.*

Sample	Dominant particle size
Low density area, 700 °C	5 nm
High density area, 700 °C	12 nm
500 °C	18 nm
600 °C	6 nm
700 °C	15 nm
800 °C	6 nm
1000 °C	21 nm

TABLE 7.1: *Table of dominant particle size from nanoparticle growth experiments.*

7.3 Carbon nanotube growth

Multiple experiments were made to grow carbon nanotubes with chemical vapour deposition, with varying parameters. The parameters for all growth experiments can be seen in table 7.2.

Batch	Substrate	Temperature	Growth	CH_4 flow	Notes
B1	Si	≈900 °C	30 min	400 sccm	
B2	Si	≈900 °C	30 min	400 sccm	
B3	Si	920 °C	30 min	400 sccm	
B4	Si/Quartz	920 °C	60 min	400 sccm	
B6	Quartz	920 °C	60 min	400 sccm	
B7	Quartz	1000 °C	60 min	400 sccm	
B8	Si	600-1000 °C	60 min	400 sccm	Varying temp
B9	Quartz	1000 °C	60 min	300 sccm	Nanoparticle size test
B10	Quartz	600-1000 °C	60 min	300 sccm	Diff. oven positions
B11	Quartz	1000 °C	60 min	300 sccm	Annealed
B12	Quartz	1000 °C	60 min	300 sccm	
B13	Quartz	600-1000 °C	60 min	300 sccm	Dip-coat, varying temp
B14	Quartz	600-1000 °C	60 min	300 sccm	Spin-coat, anneal
B15	Si/Quartz	750 °C	60 min	400 sccm	Dip-coat, anneal

Table 7.2: *Parameters used for carbon nanotube growth. Experiments above the line were made with nanotubes grown from the FeCl/photoresist solution, and experiments under the line with the FeCl/ethanol solution.*

The purpose of the first four batches was to determine whether the nanoparticles grown from the 1 mM FeCl/photoresist solution could be used to grow nanotubes, as well as to test out the growth method. This method of growing nanoparticles proved to have some effect, as the carbon had been visibly deposited selectively at the places that nanoparticles had been created as seen on figure 7.7.

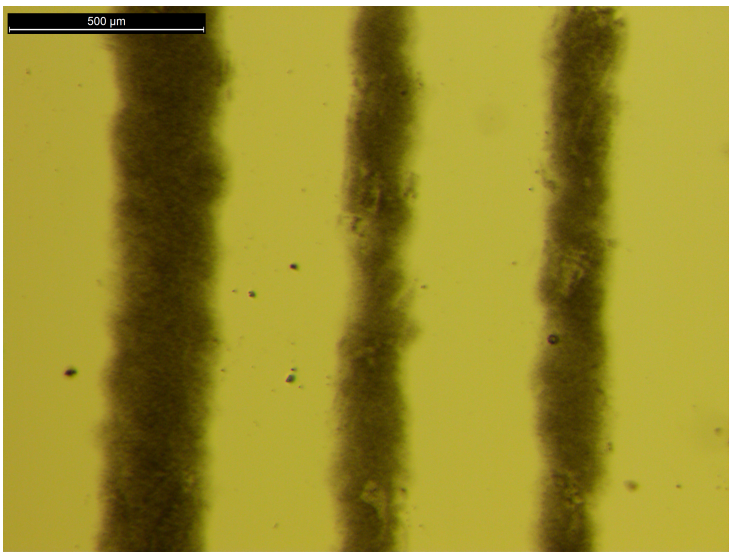

Figure 7.7: *Microscope image of deposited carbon on created lines of iron nanoparticles on a Si substrate.*

Some areas were visibly darkened after the growth, which was taken as a sign of carbon deposition, and subsequent EDX measurements revealed high quantities of carbon on the surface. No nanotubes were found in measurements with AFM, SEM or Raman spectroscopy. More experiments were made on quartz, but no nanotubes could be found. Batch 8 was made in order to test the effect of temperature on the growth process, and silicon was used to get better images. The wafers were placed at different positions throughout the tube furnace, and a temperature gradient from 650 to 1000 °C was recorded from the tube edge to the center. This batch yielded a multitude of nanotubes centered around single particles on the surface, as seen on figures 7.8 and 7.9.

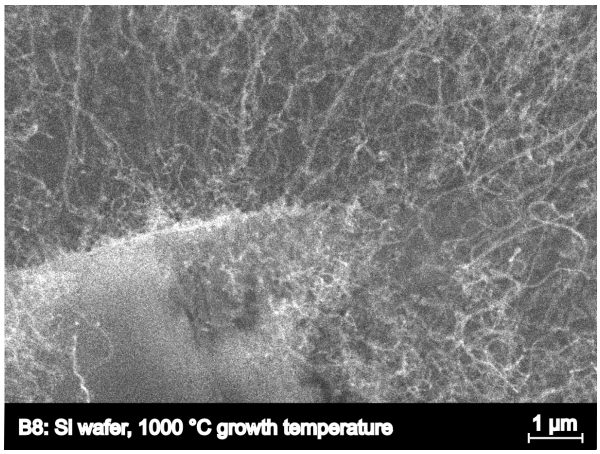

FIGURE 7.8

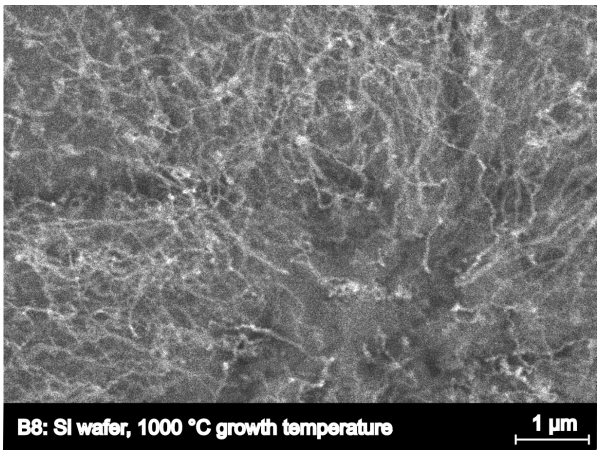

FIGURE 7.9

The nanotubes seen on figures 7.8 and 7.9 were from the same sample placed near the center of the oven, where the temperature was expected to reach the peak value of 1000 °C. These nanotubes all grew from the same large particle, however this particle turned out a lot larger than the average of around 10-15 *nm* in diameter found during AFM measurements, so whether it is an extremely large iron particle or merely dust or debris on the surface remains unknown. The nanotube diameter measured at around 50 *nm*. This sample was examined using Raman spectroscopy, which yielded the spectra seen in figure 7.10.

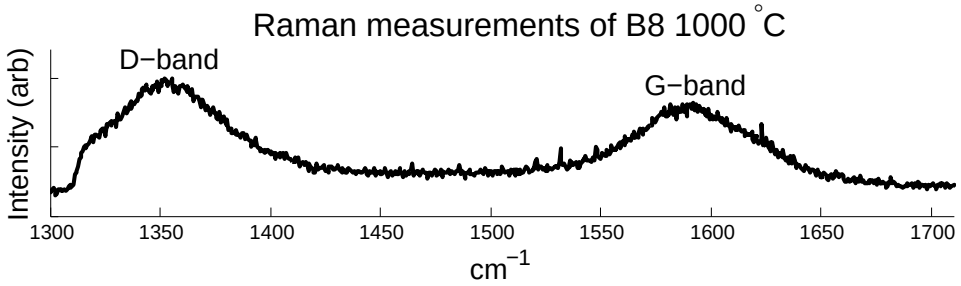

FIGURE 7.10: *Raman measurements on a B8 sample grown at 1000 °C.*

Two features were observed on the Raman spectra, the G-band at 1590 cm^{-1} and the D-band at 1350 cm^{-1}. No RBM were discovered, and the range in which the G'-band should be was not measured.

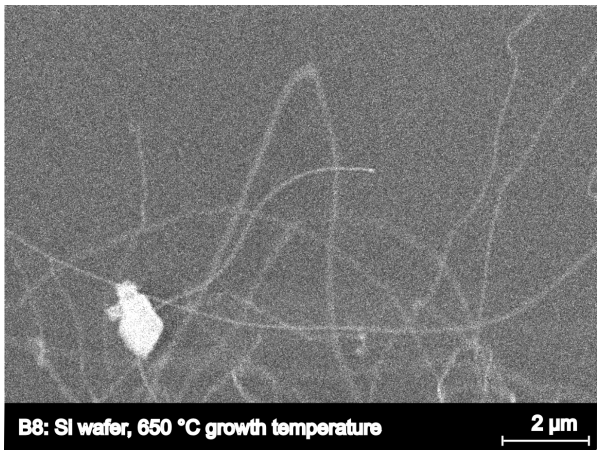

Figure 7.11

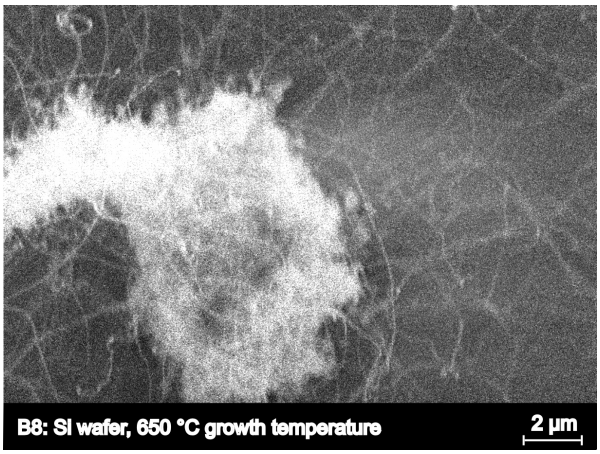

Figure 7.12

A different sample from batch 8 was placed closer to the edge of the tube furnace, which puts the growth temperature at around 650 °C. Nanotubes were again found around large specks on the surface, albeit at a lower density, as seen on figures 7.11 and 7.12. Measurements in the SEM placed these at around 100 nm in diameter, which corresponds with the lower temperature having a tendency to grow multi-walled carbon nanotubes.

Batch 9 was to test the size dependance of nanoparticles on temperature during the growth (see table 7.1), but no nanotubes were found on them in subsequent measurements. As such an experiment similar to batch 8 was done with different nanotube growth temperatures, only with quartz as the substrate instead of silicon, resulting in the samples from B10. Curiously nanotubes were only found on the samples which had been close to the edge of the tube furnace, and thus had a lower growth temperature. Their diameters measured at around 70 nm, however since the quartz wafers had to be coated with gold to image them in the SEM, this measurement might be imprecise. A few subsequent batches were grown with nanotubes in the same position. For batch 11 and onwards the quartz wafers were annealed in hope that this would help with the surface alignment of the nanotubes described in literature [52]. Furthermore a line pattern was written with the direct write system on the wafers, to have areas without nanotubes for easier viewing with AFM. The results from batch 11 can be seen on figures 7.13 and 7.14.

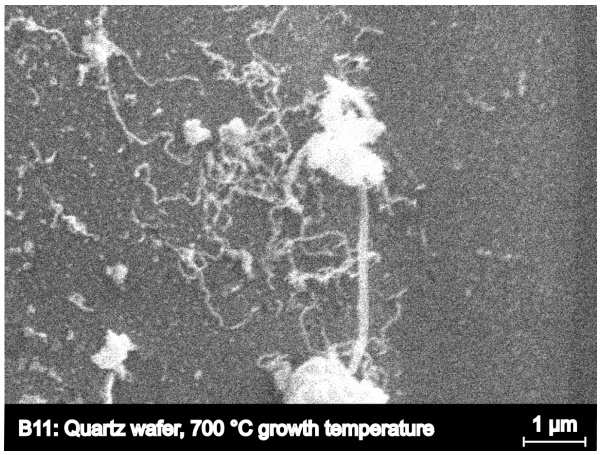

Figure 7.13

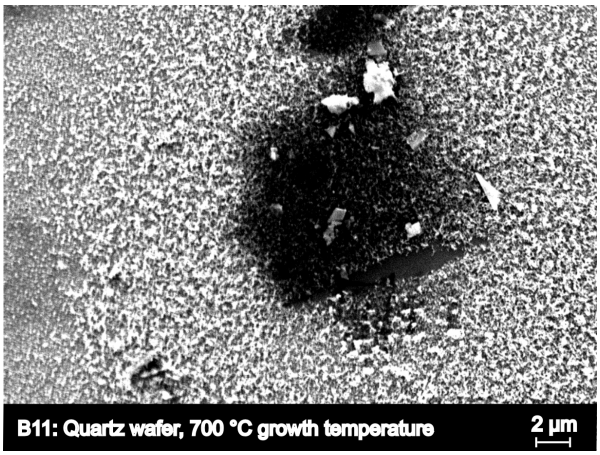

Figure 7.14

The nanotubes found on batch 11 were only found in a few places, and were not of high quality. Figure 7.13 shows multiple shorter nanotubes next to two grains on the surface. The other growth site found, seen in figure 7.14 shows another variation with a multitude of short nanotubes centered around a few larger grains and an unidentified dark spot on the surface. Neither of these configurations would prove effective as a photodetector. No Raman data were extracted from this sample as they were coated with gold. B12 was grown with mostly the same parameters, and the Raman data from this sample can be seen in figure 7.15. Again only the D-band and G-band were observed at 1350 cm^{-1} and 1600 cm^{-1} respectively. The G-band is slightly more pronounced here than for B8, however the D-band is still roughly the same size. No RBM peaks were observed anywhere on the sample.

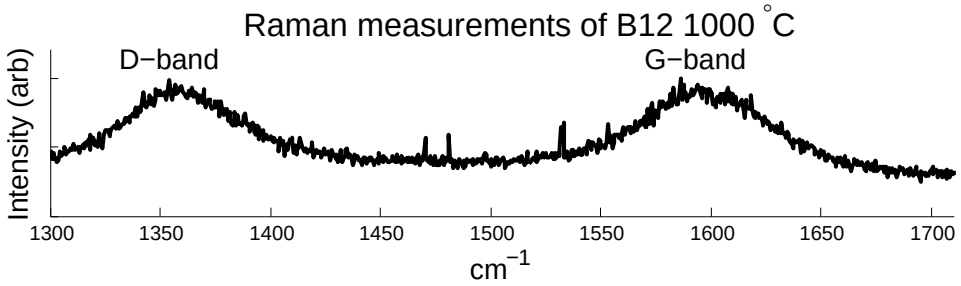

FIGURE 7.15: *Raman measurements on a B12 sample grown at 1000 °C.*

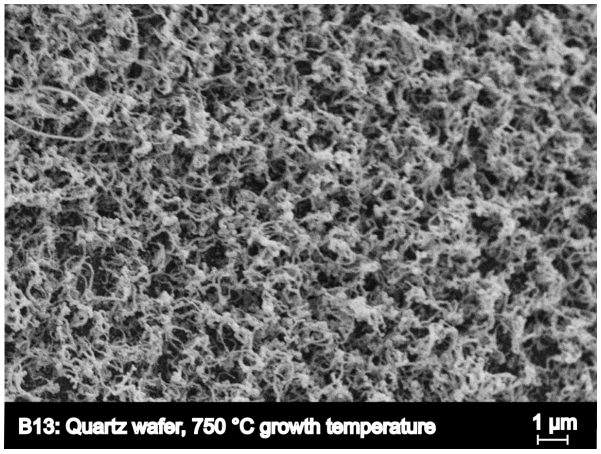

FIGURE 7.16

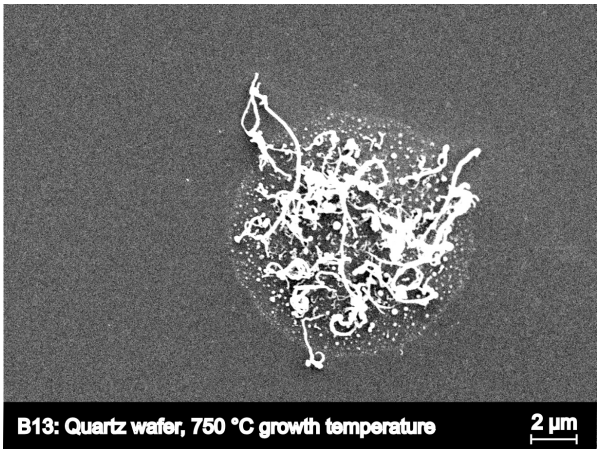

FIGURE 7.17

After limited success with growing nanotubes with the original FeCl/photoresist solution, experiments were made with an 1 mM FeCl in ethanol solution. While this method would limit the ability to control the nanotube growth sites, it should up the quantity of grown nanotubes. Batch 13 was the first batch grown with the new nanoparticle solution, and as such they were grown at different oven positions, resulting in differing temperatures between the samples. Almost no nanotubes were found on the outermost sample around 600 °C, but the samples further in at around 750 and 850 °C were abundant with nanotubes. Figures 7.16 and 7.17 show the sample grown at 750 °C. On figure 7.16 it can be seen that the new nanoparticles have grown into a forest of tangled nanotubes of indeterminate length, with diameters at around 80 *nm*. The other site shown in figure 7.17 has larger nanotubes, with diameters in the range of hundreds of nanometres. Similar trends were seen on the sample grown at 850 °C.

B14 was also performed with the FeCl/ethanol solution, but had it spin-coated on instead of dip-coated. The resulting nanotubes can be seen in figure 7.18. Note that the nanotubes were only found on a small section of one of the samples after applying the gold coating. As usually seen, these nanotubes showed no preference in their growth direction, but would instead be bundled up as normally observed. Contrary to the B13 samples, these nanotubes appear to be much longer, but their diameter is still around 130-200 nm when observed in the SEM. Raman spectroscopy was also attempted, yielding the spectrum shown in figure 7.19. Here the G'-band was measured, being positioned at 2720 cm^{-1}, along with the D-band at 1355 cm^{-1} and the G-band at 1600 cm^{-1}. No RBM peaks were measured on this sample.

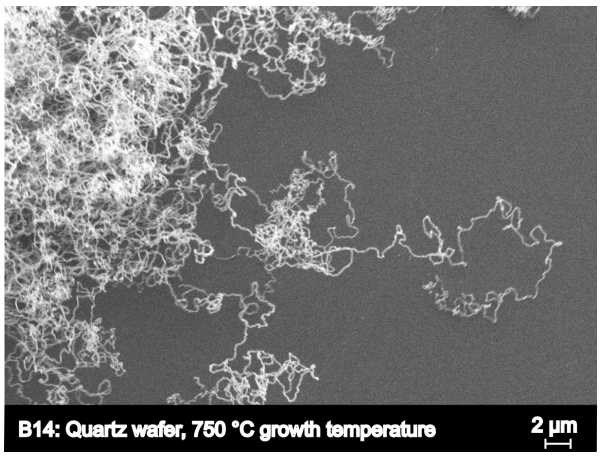

Figure 7.18

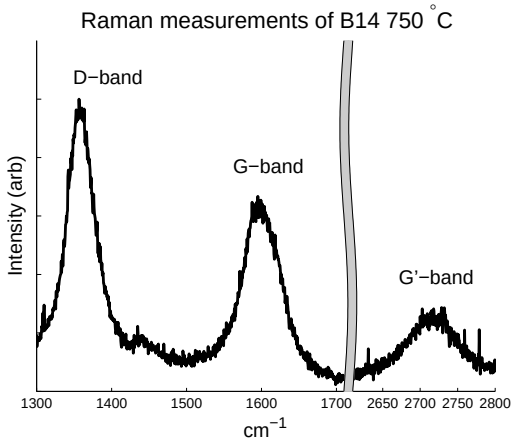

Figure 7.19

The last batch B15 was once again grown through dip-coating with the FeCl/ethanol solution, but instead of growing the nanoparticles at 700 °C, the ethanol was simply allowed to evaporate, and the samples were inserted for nanotube growth as-is. The nanotube growth was completed with standard parameters, and the resulting nanotubes can be seen in figures 7.20 and 7.21. While most of the nanotubes do not become very long, a few statistical outliers can be seen, as illustrated in figure 7.20. While the coverage of nanotubes in this growth experiment was a lot better than previous experiments, the resulting nanotubes are still much too short to have any practical value.

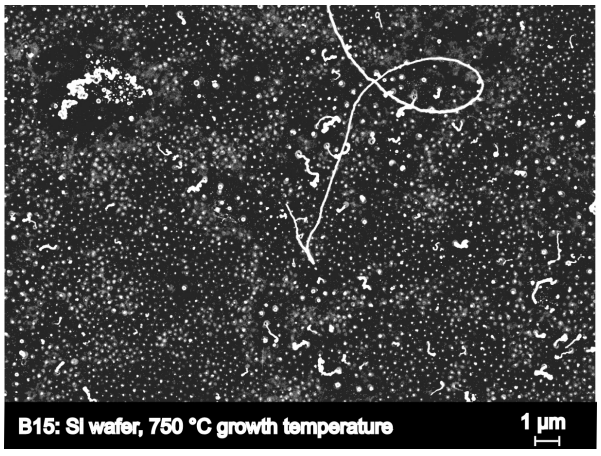

Figure 7.20

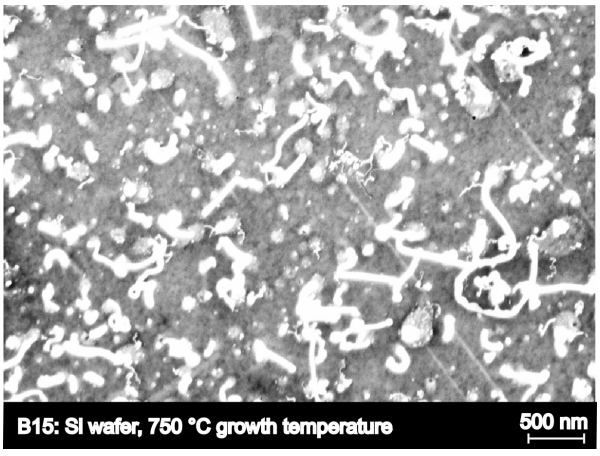

Figure 7.21

7.4 Characterization of bought nanotubes

The nanotubes bought from mkNANO were also examined with SEM, AFM, absorbance and Raman spectroscopy, with the goal of comparing them to the ones grown through experiments. After an extensive exfoliation process using sodium cholate or Triton X-100, the nanotubes were deposited upon a quartz substrate and examined with AFM. The result can be seen in figure 7.22. While the nanotubes are distorted from artefacts from the cantilever, they can be seen to lie relatively straight on the surface, as well as being mostly separated from each other. Their diameters are found from the height of the features to be around 6 nm. Their lengths vary greatly, from the shortest being just a few hundred nanometres, and the longest measuring around 20 μm. The phase image in figure 7.23 reveal that the nanotubes are enveloped in another material, most likely the surfactant, as seen on the white areas surrounding the nanotubes.

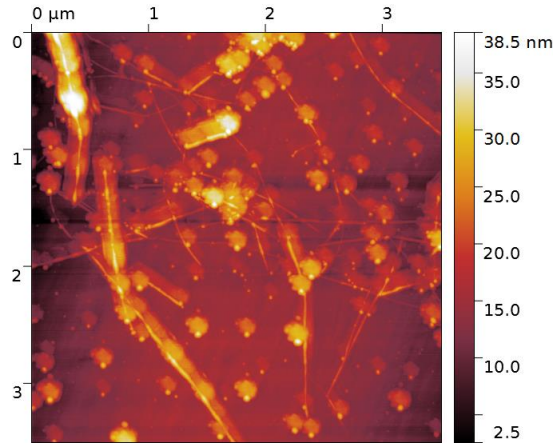

FIGURE 7.22: *AFM topography of purchased, carbon nanotubes.*

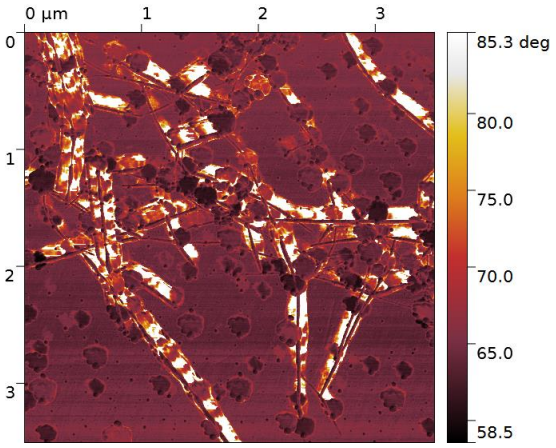

FIGURE 7.23: *AFM phase image of purchased, carbon nanotubes.*

Subsequently the nanotubes were put on a silicon substrate and examined with SEM, yielding figures 7.24 and 7.25. Both samples had nanotubes exfoliated with Triton X-100 solution. The nanotubes appear reasonably separated, however the large amount still leads to them piling on top of each other. While the length is difficult to discern from the pictures, single nanotubes can be measured at several microns, while the diameter is consistently measured at 15-20 nm. This is inconsistent with the AFM measurements, however since the AFM is better at measuring topography, the height from those measurements should be used.

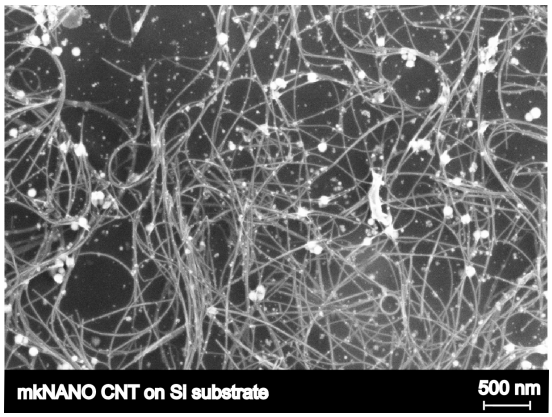

FIGURE 7.24

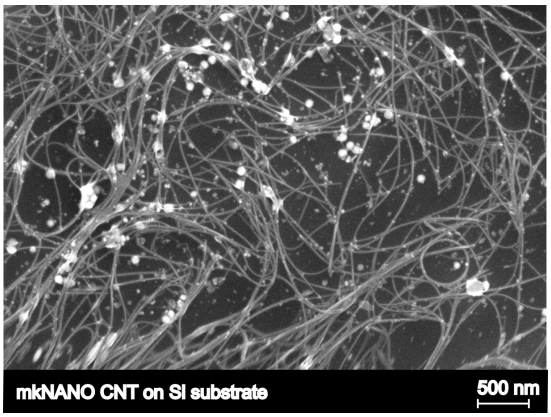

FIGURE 7.25

Samples were also examined with Raman spectroscopy, yielding the spectra shown in figure 7.26, specifically of carbon nanotubes on a quartz substrate. Here the G-band dominates both the D- and G'-band, which indicates that the nanotubes have a low amount of defects when compared to the ones grown through CVD. No RBM-peaks were observed. Similar results were gotten from later measurements using a silicon substrate instead.

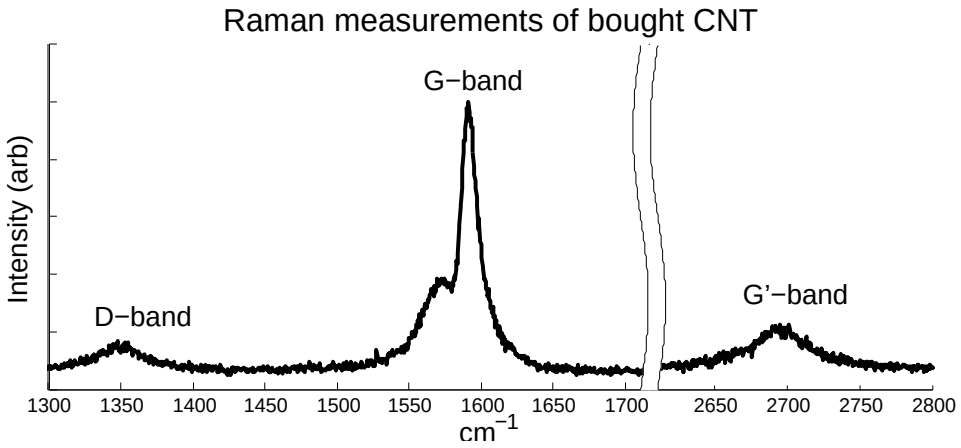

Figure 7.26: *Raman spectroscopy of carbon nanotubes on a quartz substrate.*

The measurement for the absorbance spectrum was obtained. As can be seen on the data in figure 7.27, there are no clear peaks and a lot more absorption in the UV-area. This background absorbance is due to π-plasmons and the presence of graphene which is not filtered out with this technique [61]. To find the peaks, a 5th order polynomial fit is subtracted from the data to better show the peaks. A 5th order polynomial is chosen because it does not cloud the peaks, although because the nanotubes have many different (n,m)-values, the data are rather inconclusive and the peaks are hard to see.

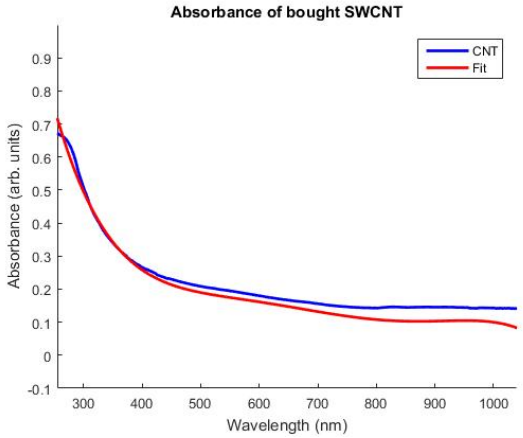

Figure 7.27: *Measured absorbance*

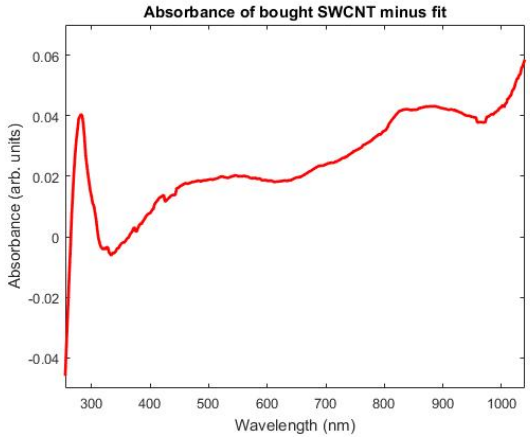

Figure 7.28: *Measured absorbance with fit withdrawn*

7.5 Electrical characterisation of carbon nanotubes

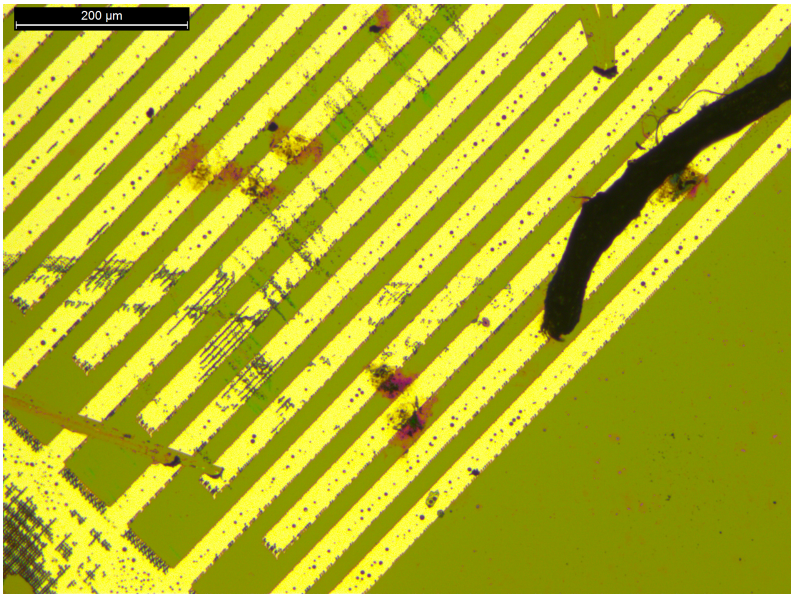

FIGURE 7.29: *20 μm separation on aluminium after the breakdown process with a big black cylindrical structure and red spots from the process.*

The samples were prepared as described in chapter 6.3 and a cross-sectional view of the sample can be seen in figure 6.6. A few of the samples had large agglomerates of carbon nanotubes as can be in figure 7.29. The measurements were taken with a four point probe system inside a Faraday cage. Table 7.3 shows the resistance of all the samples along with references to the relevant current-voltage curves. The first type of samples have two different linear regions, the theory behind which is described in chapter 3.5.1. Measurements on this type of sample also show hysteresis, where going back and forth in current does not yield the same result. This was deemed to be a capacitative effect and thus different scan speeds and discharge measurements were performed to quantify the capacitance. On figures 7.30 and 7.31 the hysteresis effect can be observed for the higher maximum current measurement. On figure 7.35 a discharging measurement with an exponential tail can be observed. The second type of samples have a linear current-voltage relationship, but also large nanotube agglomerates on top as that seen in figure 7.29. These samples exhibited an increasing resistance after every subsequent measurement, as seen in figure 7.34. Additional measurements can be seen in appendix C. No photocurrent was observed on any of the samples and thus no data is shown.

Sample	Resistance	Dark current	Figure
Chrome, 20 μm	$8.1 * 10^6\ \Omega$	$1.1 * 10^{-10}\ A$	7.34
Chrome, 15 μm	$8.3 * 10^6\ \Omega$	$0\ A$	7.30, 7.31
Aluminium, 20 μm, a	$1.0 * 10^7\ \Omega$	$1.3 * 10^{-12}\ A$	7.32
Aluminium, 20 μm, b	$2.3 * 10^8\ \Omega$	$3.1 * 10^{-10}\ A$	7.33

TABLE 7.3: *Table of resistances and darkcurrent*

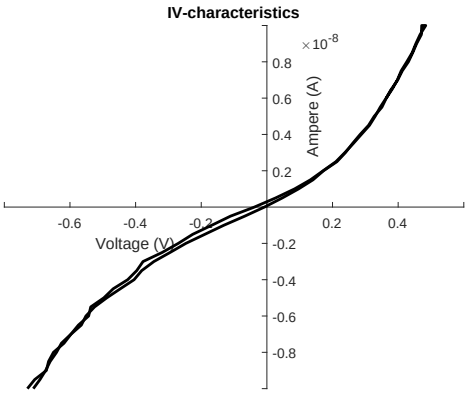

Figure 7.30: *15 μm separation on chrome and 10 nA maximum current.*

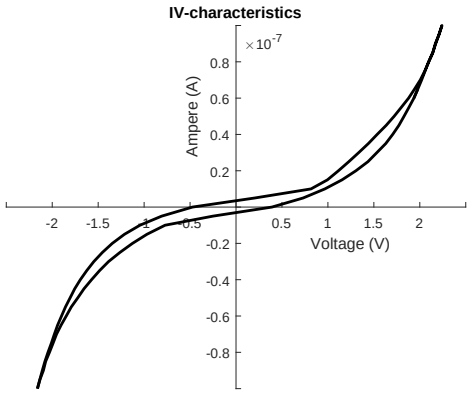

Figure 7.31: *15 μm separation on chrome and 100 nA maximum current.*

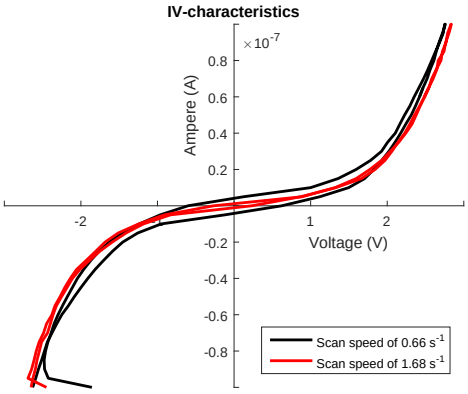

Figure 7.32: *20 μm separation on aluminium, a and 100 nA maximum current.*

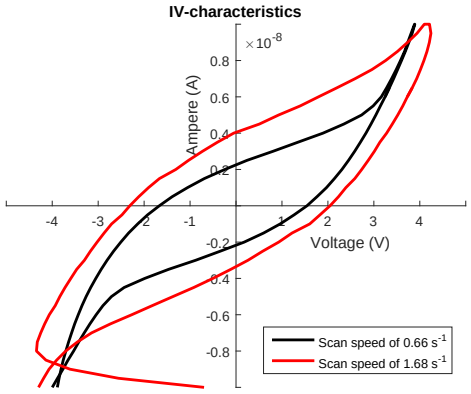

Figure 7.33: *20 μm separation on aluminium, b and 10 nA maximum current.*

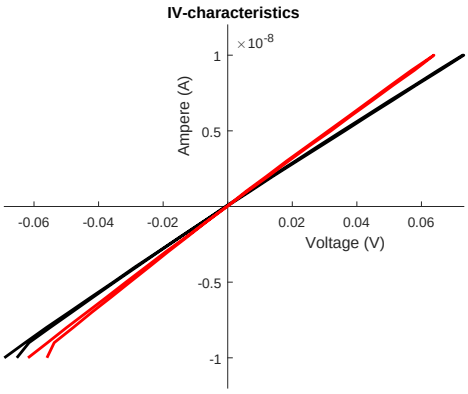

Figure 7.34: *20 μm separation on chrome and 10 nA maximum current.*

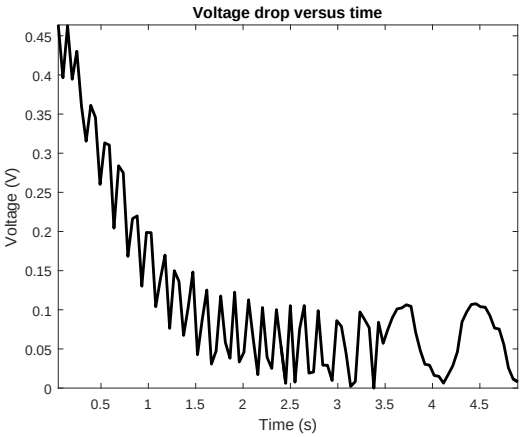

Figure 7.35: *15 μm separation on chrome voltage drop after 200 nA*

8 Discussion

8.1 Nanotube characterization

Two types of nanotubes were examined, those grown using chemical vapour deposition and those bought from mkNANO. Since most of the experiments regarding nanotubes deal with the growth process, many of the individual growth steps have been examined. This section deals with the effects of the different growth parameters, as well as the characterization of the two nanotube types.

8.1.1 Effect of substrate surface

Two types of substrates were used for growth, silicon and quartz. The silicon[100] had a thin natural oxide layer. These were not examined much during the process, as their role was to give better imaging with the SEM. The alternate substrate was ST-cut quartz, which has been described as having a rectifying effect on grown carbon nanotubes, which should result in them growing in aligned arrays. This effect was not seen experimentally during this project, leading to further examination of the quartz surface.

The quartz wafers were examined with Raman spectroscopy, as shown in figure 7.3. Comparisons with data by Krishnamurti [62] determined that the wafers were made of α-quartz from the peaks at 456 cm^{-1} and 265 cm^{-1}. The peaks were sharp, with a full width half maximum of 12.9 cm^{-1}, indicating a good periodic structure, without too many imperfections. Looking at figures 7.1 and 7.2 steps of a few nanometers can be seen, which are much higher than atomic steps. This could be due to polishing cuts or a stepped surface from the ST-cut quartz wafer. A few small particles can be seen on the surface. These are determined to be agglomerates of quartz, since there is no change in color on the phase image. The agglomerates are larger before annealing, likely due to diffusion on the surface. Regarding the growth of aligned carbon nanotubes, there is no indication on any of the images that the carbon nanotubes follow the ST-cut/gas flow direction. It is believed that either the nanotubes do not grow as anticipated as most are multi-walled, or the surface should have been polished more, or treated further to yield the anticipated effect.

8.1.2 Nanoparticle size analysis

The surface density of particles was calculated with two different methods both utilising the software Gwyddion. Here a threshold height can be defined, and all larger features above it can be counted as particles. In the first method (S.D. (1)), the surface density of particles is found

by summing up the surface area of all nanoparticles, and dividing with the scan area, as seen in equation (8.1). Here N is the number of particles and A_p the surface area of each particle, while w and l are the width and length of the image. The data is collected from the AFM image and not an average from the whole wafer, hence some statistical outliers may occur.

$$\text{S. D. (1)} = \frac{\sum_{i=1}^{N} A_{p,i}}{w\ l} \tag{8.1}$$

The second method (S.D.(2)) also estimated the surface density of particles by taking the histograms for height, but the assumption that all the particles are spherical is made. This is done to avoid the additional width of the AFM cantilever on each particle. Utilising the height (h_p) as the diameter of each particle and approximating their surface area as a circle allows for the calculation of the total surface area as seen in equation (8.2).

$$\text{S. D. (2)} = \frac{\sum_{i=1}^{N} \left(\frac{h_{p,i}}{2}\right)^2 \pi}{w\ l} \tag{8.2}$$

An average diameter/height (d/h) ratio has been found by assuming circular particles for the surface area data to find the diameter of each particle. The diameter of each particle is divided by its corresponding height and the results are then averaged. This leads to an average aspect ratio for the particles. The width and height of the image is the same for both the total width and the total height.

Sample	S. D. (1)	S. D. (2)	Dominant particle size	d/h ratio
Low density area, 700 °C	0.4%	-	5 nm	-
High density area, 700 °C	5.6%	-	12 nm	-
500 °C	43.4%	6.53%	18 nm	1.9:1
600 °C	27.7%	1.44%	6 nm	3.7:1
700 °C	27.3%	5.75%	15 nm	1.7:1
800 °C	29.1%	0.47%	6 nm	7.8:1
1000 °C	17.3%	0.64%	21 nm	4.5:1

Table 8.1: *Table of surface densities of particles (S. D.) with two methods described in section 6.4.4, dominant particle size and diameter/height ratio.*

As seen in table 8.1 neither the dominant particle size, nor the surface density of particles follow a particular trend for an increased growth temperature, beside the surface density calculated with (S.D.(2)), which indicates a decrease with increased temperature. While the melting temperature for iron oxide is 1566 °C [63], most materials with dimensions on the nanoscale have a reduced melting temperature [64]. The iron oxide could therefore have melted off and caused the reduction of particle density.

The problem with having a high particle density is the difficulty in detecting the carbon nanotubes with AFM after growth. The problem with too low density is not growing enough carbon nanotubes. For the two methods of determining the particle surface density, the second one yields a result closer to the actual coverage, but it does not give a result which can be used to determine whether or not it is possible to detect carbon nanotubes after growth with the AFM.

The diameter/height ratio exhibits a tendency towards flattening of the particles with increasing temperature. It is assumed the iron oxide diffuses on the surface and gathers in particles, but due to gravity the particles cannot keep their spherical shape and will flatten as more material is gathered.

Zhou et. al. [57] used a similar growth method at 700 °C for the iron oxide nanoparticles and obtained average diameter of 6 nm. The distribution in this thesis was larger and with a few statistical outliers more than thrice the size of the others. Ordinarily a larger temperature would result in larger particles due to the increase in diffusion length, meaning more material can gather at one location. The data was too inconsistent to draw a conclusion. Unless the wafer and the material deposited on to it can make a chemical bond, all particles will try to gather in spherical shapes to minimise their surface area and gain the lowest possible energy. [21]

8.1.3 Characterization of bought and grown nanotubes

Starting with the SEM images, an immediate difference in nanotube quality is seen when comparing the images of grown and bought nanotubes in chapters 7.3 and 7.4 respectively. Rarely were the grown nanotubes long enough to be used as photodetectors, and of the two batches that actually produced long nanotubes, they either grew from large impurities on the surface as in batch 8, or they grew in huge tangled "forests" of nanotubes. In either of the two cases, while it could be seen macroscopically that carbon was being deposited only on the desired growth sites, nanotubes would grow close together at seemingly random locations on the samples, with overall coverage being low. The nanotube diameter was also recorded anywhere between 50 to 500 nm, which is far beyond what is normally expected from single- or even multi-walled carbon nanotubes. SEM images are however a less than ideal way of determining the thickness of carbon nanotubes, as they will often appear distorted and wider than in reality [65]. This is supported by the SEM images of the bought nanotubes, which were measured to be around 15-20 nm in diameter. Their actual diameter is closer to 6 nm, according to AFM measurements. While the SEM has a tendency to exaggerate the nanotube diameter, the large diameter observed for the grown nanotubes do indicate that they are either heavily bundled together in rope-like structures, or are heavily multi-walled. No AFM measurements were ever successful in finding the diameter of the grown nanotubes, so this could not be verified.

The bought nanotubes were found with AFM, as shown in chapter 7.4. The same bundling from the SEM pictures was also found here, along with evidence of surfactants connected to the nanotubes. The difference in phase seen in figure 7.23 demonstrate a change in material; because of the difference in material stiffness, the cantilever will change phase with respect to its driving oscillation [66]. This is evident in the brighter areas surrounding the nanotubes. The nanotube height was measured at 5 nm, seemingly pinning it as multi-walled, however as the Triton X-100 molecules are still attached, this number could be misleading.

The length of the attached Triton X-100 is difficult to determine, but it can be approximated. A study by Robson and Dennis [67] showed that statistically the Triton X-100 molecules have an average of 9.5 oxyethylene groups. These have a length of 3.4 nm in the fully extended zig-zag conformation, but only 1.6 nm for a random coil structure, plus an added octylphenyl group of around 1 nm. Subtracting the size of the Triton X-100 molecules leaves the diameter of the nanotubes in range of 0.5-2.4 nm, opening the possibility that they are single-walled.

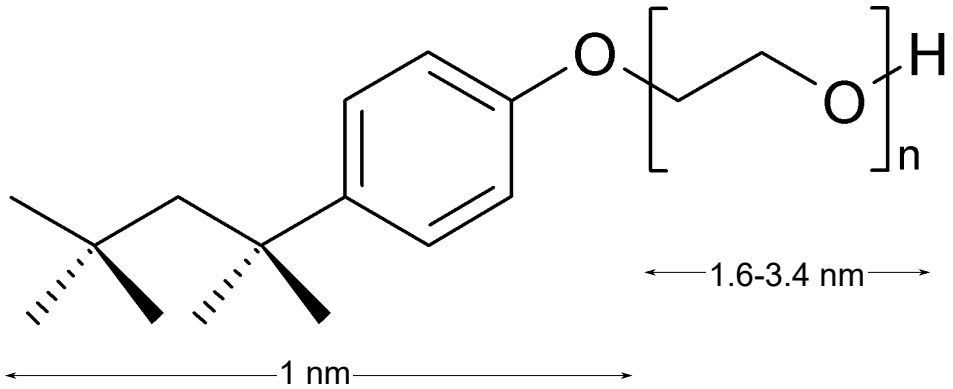

Figure 8.1: *Triton x-100 molecule, with n denoting the amount of oxyethylene groups.*

Raman spectroscopy proved that the grown nanotubes had a high amount of defects, and none of the nanotube-specific RBM peaks were observed, not even for the samples with bought nanotubes. As nanotubes were observed on multiple samples using other methods, while still not showing any RBM peaks in Raman spectroscopy, something must have been interfering with the measurements. There can be multiple reasons behind this interference. For the produced nanotubes, it may be that the nanotubes are too short to be registered, or that they have not been hit with the laser, due to them growing in small, scattered clusters. More likely, due to their large diameter when observed in SEM, the nanotubes that were grown could be multi-walled. For the bought nanotubes it may be that they are still enveloped in surfactant, which could interfere with the radial breathing modes of the nanotubes. Otherwise they could simply still be bundled together from a failed exfoliation, though figures 7.24 and 7.25 show the nanotubes as relatively separate, but still connected. Comparatively, the absorbance spectrum in figure 7.27 showed some weak peaks, which indicate that the carbon nanotubes are still bundled. When the carbon nanotubes have contact to each other they change material properties and cannot be measured accurately any more.

Since the RBM peaks could not be used for nanotube characterization, the other features should be compared instead. Looking at figure 7.19 for the batch 14 of grown carbon nanotubes and comparing them to the bought nanotubes in figure 7.26, there are some immediate differences. Firstly there is the shape of the G-band. The bought nanotubes show the characteristic split peak shown by Dresselhaus et al. [47] in figure 4.2. The shape of the peaks, with one peak being significantly lower than the other, shows that the bought nanotubes are predominantly semiconducting and single-walled. This makes sense as 2/3 of randomly grown carbon nanotubes would be semiconducting. For the produced nanotubes however, only a single peak is present in the Raman data, and it is a lot broader. These characteristics would mean that these nanotubes are mostly multi-walled nanotubes, due to the slightly asymmetric line shape, and the smeared-out peak due to the many different nanotube diameters. The D-band peak also reveal that the the grown nanotubes contained more defects than the bought, as seen from the D/G ratio. For the grown nanotubes, the D-band has mostly the same intensity as the G-band, whereas the D-band is much smaller for the bought nanotubes. Furthermore, using equation (4.6), the diameter of the bought nanotubes can be estimated from the locations of the two peaks in the G-band. These were measured at about 1573 cm^{-1} for the G− band, and 1592 cm^{-1} for the G+ band. Since the shape of the G-band indicates that the nanotubes are mostly semiconducting, the constant ε was set to 47.7 nm^2cm^{-1}, leading to a nanotube diameter

of 1.5-1.6 *nm*. This seem to support the estimated nanotube diameter when subtracting the surfactant from the surface. Any possible graphene peaks would be shadowed from the nanotube peaks.

In summary the SEM images of the CVD grown nanotubes, mostly showed them as being too short or irregular, having poor surface coverage and not following the quartz crystal direction. Furthermore Raman spectroscopy revealed them as being mostly multi-walled, and containing many defects, further diminishing their usefulness. The nanotubes bought from mkNANO were proven to be single-walled through Raman spectroscopy. While their diameter was measured as being too large with AFM unless the surfactant molecules are subtracted. The result from Raman spectroscopy proved that their diameter is indeed in the single-walled regime. Raman spectroscopy furthermore showed them as having far fewer defects, leading to them being more suited as components in a photodetector.

8.1.4 Evaluation of the growth process

While the process of growing carbon nanotubes seems simple in literature, it was never successful with the methods used in this report. The nanotubes were produced in multiple growth experiments, but they never had the length or quality needed to be used in a photodetector.

One aspect of the growth process that proved problematic was the size of the nanoparticles. Optimally, for growth of single-walled carbon nanotubes, the nanoparticles should not be larger than a few nanometres in diameter. As seen in table 8.1, while nanoparticle synthesis temperatures did produce particles with a diameter around 5 *nm*, these results were hardly consistent overall. Only iron nanoparticles were used as catalysts, whether from a photoresist or an ethanol solution, and while both appeared to catalyse carbon deposition on the surface, neither could consistently grow nanotubes.

Another problem may have been the growth temperature. Since this was inconsistent throughout the tube furnace, the nanotubes may not have had a sufficiently high temperature of formation. Many of the samples which sprouted nanotubes were however placed near the edge of the tube furnace where the temperature was lower. This may indicate that the nanotubes could only be found because they were multi-walled due to the low growth temperature. Since imaging of the produced nanotubes consistently was a problem during the project, it may be that single-walled nanotubes could have sprouted on some samples near the center of the tube furnace at a higher temperature, and that they were simply not detected. Many of the substrates were also made of quartz, meaning that they had to be coated with 10-15 *nm* gold for any images of the surface to be seen. This gold coating could then have obscured the grown nanotubes due to its surface roughness.

8.2 Discussion of current-voltage curves

From the graphs (eg. figure 7.31) it can be seen that the first type of current-voltage curves has a symmetrical 2 stage curve. This is due to a symmetrical Schottky barrier in both ends of the nanotube interconnecting to the metal electrodes. The first linear region at low voltage is the resistance of the reverse Schottky barrier, also seen in figure 3.14 with a symmetrical Schottky barrier and chapter 3.5.1 for the theory. After the reverse biased barrier, is passed, the current will enter a new region. Here the applied voltage is high enough to tunnel through the barrier. This was also shown by Qi et. al. [26], where a similar MSM-structure was created.

Getting an ohmic contact is difficult when the contact area size is small in all dimensions, as is the case for nanowires. The contact resistance is not taken into consideration however, and has to be added. Comparing the resistances seen in table 7.3 to data from Qi et. al. [26], his group measured a resistance 3 orders of magnitude higher, but the added resistance was attributed to contact resistance at the electrodes. While silicon and carbon nanotubes are two very different materials, the results from this thesis are still comparable to theirs, due to contact resistance being mostly eliminated when using a four point probe system. Zhao et. al. [30] measured resistances in the range of $10^7 - 10^8$ for one single-walled carbon nanotube. This is in agreement with the resistance from the measurements in table 7.3, though the resistance is expected to go down when having many carbon nanotubes in parallel. The resistance of the samples coated with chrome are lower compared to those coated with aluminium. This could be attributed to the amount of nanotubes between the electrodes or the fact that a small oxide layer is grown on top of the electrodes. Aluminium oxide has a resistivity of 10^{14} Ωcm [68] against that of chrome oxide with 10^8 Ωcm [69]. The reference sample with aluminium contacts and no carbon nanotubes on top does not conduct any current at 20 V bias, indicating the deposition of carbon nanotubes has an influence on the electrical properties of the photodiodes.

Comparing the bias voltage of the measurements in figure 7.32 to that of Qi et. al. [26] in figure 3.14 for the symmetrical nanowire design, it is immediately seen that the amount of applied voltage needed to tunnel through the reverse biased Schottky diode is lower for the samples done for this thesis. This is in good agreement with the theory described in chapter 3.6.1, where the Schottky barrier width was found to be thin for a metal-carbon nanotube interconnect.

A graph exhibiting a symmetrical response means there is no doping. Most of the curves were symmetrical except a sample with chrome and 20 μm separation seen on figure C.4. This sample exhibits a slight n-type behaviour, as the voltage required to reach the same current is lower in the positive end. Furthermore the low on-off ratio indicates that quasi-metallic carbon nanotubes are present. Semiconducting carbon nanotubes cannot conduct more than a specific dark current until a certain voltage, depending on temperature and doping [70].

Regarding the process of electric breakdown on the quasi-metallic carbon nanotubes, the chrome electrodes seemed to yield before the nanotubes, as the resistance remained similar, while the electrodes became black. For the aluminium electrodes the resistance increased from $2.3 * 10^4\,\Omega$ to $3.2 * 10^4\,\Omega$ after a visual confirmation of incineration of the nanotubes, seen as red spots between the contacts (see figure 7.29). During the process a current-voltage relationship was taken before the sample was allowed to cool down, which can be seen in figure C.2. The conductance increased with temperature, which is a property unique to semiconductors.

Sample	Resistance	Capacitance (1)	Capacitance (2) at 0.5 V
Chrome, 15 μm	$8.1 * 10^6\ \Omega$	$2.4 * 10^{-8}$ F	$6.5 * 10^{-8}$ F
Chrome, 20 μm	$7.1 * 10^6\ \Omega$	-	-
Aluminium, 20 μm	$2.3 * 10^8\ \Omega$	$3.2 * 10^{-11}$ F	$1.2 * 10^{-8}$ F

Table 8.2: *Table of capacitances and resistances*

Two different methods were used to calculate the capacitance from the measurements. The first method uses the discharge over time, while the second method uses different scan speeds to obtain different hysteresis curves in the current-voltage measurements. Both methods are described in appendix E. Both methods showed great correspondence between each other on the

chrome electrodes, but were far from each other on the aluminium electrodes. Both methods yield a result that is several orders of magnitude higher than the theoretically calculated result in chapter 3.5.2 however. The theoretical result is from a simplified model and does not account for edge-capacitance. Igreja and Dias [71] made a model for interdigital electrodes, which had great agreement with their experimental results and a capacitance on the scale of picofarad. They had an electrode height on the μm scale, compared to the electrodes of this thesis at 40 nm, but with a larger separation. Thus the expected capacitance of the electrodes for this thesis should be on the scale of a few picofarad. Here the first method used on figure C.1, has a result on the correct scale. The second method on the same sample however is still in the nanofarad range. Another consideration is that the charge build up could be on the nanotubes, which are in close proximity to each other, making the capacitance higher. The encapsulating molecules could act as a dielectric between two oppositely charged carbon nanotubes.

8.3 Two designs of carbon nanotube photodetectors

8.3.1 MSM photodetector

The design of the MSM detector is described in chapter 6.3.1, and the current-voltage curves for these samples are depicted in chapter 7.5. No photocurrent higher than the noise on the ampere meter was obtained. In chapter 3.6.1 it was determined that the Schottky barrier width was small for the carbon nanotube metal interconnect, and thus the depletion region, where the device would be able to split the exciton, is on the scale of a few nanometers. This leads to poor efficiency, as the probability of absorbing 450 nm light at such a specific location is very small. Another important aspect is the needed punch-through bias to obtain a photocurrent for the MSM configuration; when the bias is high the noise is also amplified, so any potential photocurrent would become undetectable.

Using equation (3.13) for the combined cut-off frequency with the values from table 8.2 gives a result of $4.90 * 10^4$ Hz for the chrome electrodes with 15 μm separation and $9.95 * 10^7$ Hz for the aluminium electrodes. The values are small compared to that calculated in chapter 3.5.2, which is attributed to the high capacitance. The dark current is used to calculate the Schottky barrier using equation (D.1), but otherwise it can be used to determine the signal to noise ratio of a photodetector. From the equation the Schottky barriers were in the range of 200-300 eV, which is higher than the anticipated value of around 1.6 eV. This difference is attributed to the tunnelling current and the difficulty in finding the actual electrical cross-section.

8.3.2 Gated photodetector

The primary difference between the two designs is the added gate voltage, which causes an electric field to electrostatically dope a region on the nanotube to give a pnp-junction. By introducing a gate voltage a much larger depletion region is possible. Despite this, the gated photodetector did not yield any measurable photocurrent. A list of possible reasons are described here, prioritising the most significant first.

Firstly the current-voltage graphs exhibited a linear relationship, with much lower resistance compared to the MSM detector, making the noise in the current much larger with an applied bias. Secondly the Triton X-100 molecules surrounding the carbon nanotubes change their properties, which could inhibit their ability to absorb light.

Another possibility is that the field from the applied gate voltage covers the whole wafer and is thus not directed at the middle of the nanotubes. The pnp-junction could be at the very edge of the nanotube altering the depletion width, or the field could be too unfocused to electrostatically dope the carbon nanotubes. A fourth possibility is that the field has difficulties passing through the natural oxide layer at the bottom of the samples. The gate voltage was tested to be in accordance as to what was applied within 1 V, from the probe to the base which the sample is attached to. Finally, the excitation laser has a high energy (2.75 eV) compared to the bandgap of the semiconducting carbon nanotubes ($\approx$1.1 eV). This lowers the possibility of absorption. The excitation wavelength is in accordance with the excitation of quasi-metallic carbon nanotubes (1-3 eV) [38].

8.4 Perspective

After working and trying to understand carbon nanotubes as a material for photodetectors, a few considerations can be made. With respect to using carbon nanotubes as a high bandwidth photodetector for eg. optical communication, it was determined that if the MSM configuration could be improved it would be usable. The band gap can be controlled by picking nanotubes with the proper chirality (n,m), as seen on figure 2.13, and tuned to the optical wavelength. The issue of the short depletion region can be solved by applying a negative bias and having an ohmic contact in the other end. Another method would be to find a carbon nanotube with a smaller intrinsic carrier concentration, which is also dependent on the (n,m) values, as lower carrier concentration results in a larger depletion layer width. If the gated design has to used to get a photocurrent, the only advantage of carbon nanotubes is the high electron mobility. Otherwise graphene, which is easier to work with and has a similar electron mobility, can be used instead [32].

Considering the other properties such as flexibility, chemical stability and mechanical strength. Carbon nanotube based photodetectors can be used in harsh environments, and as such are still worth putting more research into.

9 Conclusion

During this project carbon nanotubes were grown and photodetectors were constructed. The nanotubes never reached the required quality to be used in any devices, leading to the use of bought nanotubes instead for the photodetectors. Extensive experiments into the exfoliation of these nanotubes were made, to separate them from each other and deposit them on contacts. This second configuration proved able to conduct electricity, but did not produce any photocurrent no matter the light source.

While the nanotubes were grown with parameters consistent with most of the available literature, no method used ever produced useful nanotubes. Whether the surface would be covered in catalyst nanoparticles or only have them at specific growth sites, the resulting nanotubes would either not grow at all or sprout in seemingly random locations on the surface. The size of the grown nanotubes also proved to be multi-walled, with diameters consistently above 50 nm, according to SEM measurements. The grown nanotubes also did not follow the cut of the crystal substrates as stated in literature, but would instead be randomly oriented on the surface, regardless of substrate orientation relative to the gas flow during growth. Neither of the two solutions used to grow catalytic nanoparticles had any effect on the final result. What was shown to be possible however was the patterning method used for specifying the growth sites of catalytic nanoparticles. Multiple AFM images showed that there would be a clear boundary between the areas where particles were grown from photoresist, and areas where the resist had been removed, with a lot more nanoparticles observed on the former. CVD growth also showed that more carbon was deposited in the areas with nanoparticles. As such, this method showed promise with regards to growth of carbon nanotubes at specified growth sites, if the nanoparticles could be improved for better nanotube catalysis.

Through the use of a direct-write system, a photodetector design made with chrome or aluminium contacts was made. Two kinds of photodetectors, one made on top of an oxidized silicon wafer, employing a gate-voltage for electrostatic doping of the nanotubes, and one made on a quartz substrate without the gate voltage. Without grown nanotubes to use, nanotubes were bought from mkNANO, which were exfoliated and deposited on the sample. Neither of these designs produced any detectable photocurrent, regardless of the light source used to induce it. Through further examination of the two designs an irregular current-voltage relationship was found, which was ascribed to the metal-semiconductor-metal configuration. The configuration can be described by thermionic-field emission theory. The current-voltage curves exhibited hysteresis, which indicates capacitance and this was examined with a voltage drop and method similar to cyclic voltammetry.

Bibliography

[1] Sumio Ijima. Helical microtumicro of graphitic carbon. *Nature*, Vol. 354:56–58, November 1991.

[2] Chenyu Wei, Kyeongjae Cho, and Deepak Srivastava. Tensile strength of carbon nanotubes under realistic temperature and strain rate. *Phys. Rev. B.*, Vol. 67:115407–p. 1–6, 2003.

[3] Seunghun Hong and Sung Myung. A flexible approach to mobility. *Nature*, Vol. 2:207–208, 2007.

[4] T. Durkop, S. A. Getty, Enrique Cobas, and M. S. Fuhrer. Extraordinary mobility in semiconducting carbon nanotubes. *Nano Letters*, Vol. 4(No. 1):35–39, 2003.

[5] Jianwei Che, Tahir Cagin, and William A. Goddard. Thermal conductivity of carbon nanotubes. *Nanotechnology*, Vol. 11:65–69, 2000.

[6] C. Torres-Torres, N. Peréa-López, H. Martínez-Gutiérrez, M. Trejo-Valdez, J. Ortíz-López, and M. Terrones. Optoelectronic modulation by multi-wall carbon nanotubes. *IOP science*, Vol. 24:p. 1–6, 2013.

[7] Amanda S. Barnard. Modelling of the reactivity and stability of carbon nanotubes environmentally relevant conditions. *Physical chemistry chemical physics*, Vol. 14(No. 29):10080–10093, 2012.

[8] Michael F. L. De Volder, Sameh H. Tawfick, Ray H. Baughman, and A. John Hart. Carbon nanotubes: Present and future commercial applications. *Sciene magazine*, Vol. 339:535–539, 2013.

[9] Stefan Frank, Philippe Poncharal, Z. L. Wang, and Walt A. de Heer. Carbon nanotube quantum resistors. *Science Translational Medicine*, 1998.

[10] Philippe Poncharal, Claire Berger, Yan Yi, ZL Wang, and Walt A de Heer. Room temperature ballistic conduction in carbon nanotubes. *Journal of Physical Chemistry*, 2002.

[11] R. Saito, G. Dresselhaus, and M.S. Dresselhaus. *Physical Properties of Carbon Nanotubes.* Imperial College Press, 1998.

[12] M. A. Omar. *Elementary Solid State physics:Principles and applications.* Addison Wesley Longman, 1975.

[13] Thomas G. Pedersen. Lectures in nanoelectronics. Fall semester 2015.

[14] Thomas G. Pedersen. *Electric, Optical and Magnetic properties of nanostructures.* 2015. Lecture notes.

[15] Jeroen W. G. Wildöer, Liesbeth C. Venema, Andrew G. Rinzler, Richard E. Smalley, and Cees Dekker. Electronic structure of atomically resolved carbon nanotubes. *Nature*, Vol. 391:p. 59–61, 1998.

[16] Taishi Takenobu, Takumi Takano, Masashi Shiraishi, Yousuke Murakami Masafumi Ata, Hiromichi Kataura, Yohji Achiba, and Yoshihiro Iwasa. Stable and controlled amphoteric doping by encapsulation of organic molecules inside carbon nanotubes. *Nature materials*, Vol. 2:p. 683–688, 2003.

[17] Donald A. Neamen. *Semiconductor Physics and devices.* McGraw Hill, 4 th. edition, 2012.

[18] University of South Carolina. Lecture on schottky barriers. `http://www.ee.sc.edu/personal/faculty/simin/ELCT566/19%20Schottky%20Photodiodes.pdf`, 29-04-2016.

[19] Harald Ibach. *Physics of surfaces and interfaces.* Springer, 2006.

[20] Volker Heine. Theory of surface states. *Physical review*, Vol. 138(No. 6a):a1689–a1696, 1965.

[21] Hans Luth. *Solid surfaces, interfaces and thin films.* Springer, 5th edition edition.

[22] Frederick Guthrie. On a relation between heat and static electricity. *Philosophical magazine and journal of science*, 1873.

[23] D. B. Payne et al. *Fibre optic communication - key devices.* Springer, 2012.

[24] Kazutoshi Kato, Susumu Hata, Kenji Kawano, and Atsuo Kozen. Design of ultrawide-band, high-sensitivity p-i-n protodetectors. *IEICE TRANSACTIONS on Electronics*, Vol.E76-C(No. 2):p. 214–221, 1993.

[25] C. Moglestue, J. Rosenzweig, J. Kuhl, M. Klingenstein, M. Lambsdorff, A. Axmann, Jo. Schneider, and A. Hülsmann. Picosecond pulse response characteristics of gaas metal-semiconductor-metal photodetectors. *Journal of Applied Physics*, Vol. 70(No. 2435), 1991. doi: 10.1063/1.349395.

[26] Yangyang Qi, Zhen Wang, Mingliang Zhang, Xiaodong Wang, An Ji, and Fuhua Yang. Electron transport characteristics of silicon nanowires by metal-assisted chemical etching. *AIP advances*, Vol. 4(No. 031307):1–6, 2014. doi: 10.1063/1.4866578.

[27] Zhiyong Zhang, Kun Yao, Yang Liu, Chuanhong Jin, Xuelei Liang, Qing Chen, and Lian-Mao Peng. Quantitative analysis of current–voltage characteristics of semiconducting nanowires: Decoupling of contact effects. *Advanced functional materials*, Vol. 17:p. 2478–2489, 2007. DOI: 10.1002/adfm.200600475.

[28] F. Buonocore, F. Trani, D. Ninno, A. Di Matteo, G. Cantele, and G. Iadonisi. Ab initio calculations of electron affinity and ionization potential of carbon nanotubes. *IOPscience*, Vol. 19:1–6, 2008.

[29] Chongwu Zhou, Jing Kong, and Hongjie Dai. Intrinsic electrical properties of individual single-walled carbon nanotubes with small band gaps. *Physical Review Letters*, Vol. 84(No. 24):p. 5604–5607, 2000.

[30] Bo Zhao, Hongxia Qi, and Dong Xu. Resistance measurement of isolated single-walled carbon nanotubes. *Elsevier measurement*, Vol. 45:p. 1297–1300, 2012.

[31] John Wilson and John Hawkes. *Optoelectronics an introduction.* Prentice Hall Europe, 1998.

[32] Fengnian Xia, Thomas Mueller, Yu ming Lin, Alberto Valdes-Garcia, and Phaedon Avouris. Ultrafast graphene photodetector. *NATURE NANOTECHNOLOGY*, Vol. 4:p. 839–843, 2009. DOI: 10.1038/NNANO.2009.292.

[33] Qingsheng Zeng, Sheng Wang, Leijing Yang, Zhenxing Wang, Tian Pei, Zhiyong Zhang, Lian-Mao Peng, Weiwei Zhou, Jie Liu, Weiya Zhou, and Sishen Xie. Carbon nanotube arrays based high-performance infrared photodetector. *Optical materials express*, Vol. 2(No. 6):p. 839–848, 2012.

[34] Francois Leonard and A. Alec Talin. Size-dependent effects on electrical contacts to nanotubes and nanowires. *Phys. Rev. Letters*, pages p. 026804–1 to 026804–4, 2006. DOI: 10.1103/PhysRevLett.97.026804.

[35] Zhihong Chen, Joerg Appenzeller, Joachim Knoch, Yu ming Lin, and Phaedon Avouris. The role of metal - nanotube contact inthe performance of carbon nanotube field-effect transistors. *Nano Letters*, Vol. 5(No. 7):p. 1497–1502, 2005.

[36] R. Martel, V. Derycke, C. Lavoie, J. Appenzeller, K. K. Chan, J. Tersoff, and Ph. Avouris. Ambipolar electrical transport in semiconducting single-wall carbon nanotubes. *Phys. Rev. Letters*, Vol. 87(No. 25):p. 256805–1 to 256805–4, 2001.

[37] Johannes Scensson and Eleanor E. B. Campbell. Schottky barriers in carbon nanotube-metal contacts. *Journal of applied physics*, 2011. doi: 10.1063/1.3664139.

[38] Shun-Wen Chang, Jubin Hazra, Moh Amer, Rehan Kapadia, and Stephen B. Cronin. A comparison of photocurrent mechanisms in quasi-metallic and semiconducting carbon nanotube pn-junctions. *ACS nano*, Vol. 12(No. 5):p. 11551–11556, 2015.

[39] Neil W. Ashcroft and N. David Mermin. *Solid state Physics.* Holy, Rineheart and Winston, 1976.

[40] Feng Wang, David J. Cho, Brian Kessler, Jack Deslippe, P. James Schuck, Steven G. Louie, Alex Ze, Tony F. Heinz, and Y. Ron Shen. Observation of excitons in one-dimensional metallic single-walled carbon nanotubes. *PHYSICAL REVIEW LETTERS*, Vol. 99:p. 227401–1 to 4, 2007. DOI: 10.1103/PhysRevLett.99.227401.

[41] Vasili Perebeinos, J. Tersoff, and Phaedon Avouris. Effect of exciton-phonon coupling in the calculated optical absorption of carbon nanotubes. *Physical Review Letters*, pages p. 027402–1 to 027402–4, 2005.

[42] Vasili Perebeinos and Phaedon Avouris. Exciton ionization, franz-keldysh, and stark effects in carbon nanotubes. *Nano Letters*, Vol. 7(No. 3):p. 609–613, 2007.

[43] Melvin Cutler and N. F. Mott. Observation of anderson localization in an electron gas. *Physical review*, Vol. 181(No. 3):p. 1336–1340, 1969.

[44] Shu-Lin Zhang. *Raman spectroscopy and its application in nanostructures.* Wiley, second edition edition, 2012.

[45] Boston university. Lecture on raman spectroscopy.

[46] M.S. Dresselhaus, G. Dresselhaus, A. Jorio, A.G. Souza Filho, and R. Saito. Raman spectroscopy on isolated single wall carbon nanotubes. *Carbon*, 2002.

[47] M.S. Dresselhaus, G. Dresselhaus, R. Saito, and A. Jorio. Raman spectroscopy of carbon nanotubes. *Physics Reports*, 409:47–99, October 2005.

[48] Mildred S. Dresselhaus, Ado Jorio, Mario Hofmann, Gene Dresselhaus, and Riichiro Saito. Perspectives on carbon nanotubes and graphene raman spectroscopy. Nano Letters, unpublished.

[49] Mukul Kumar and Yoshinori Ando. Chemical vapor deposition of carbon nanotubes: A review on growth mechanism and mass production. *Journal of Nanoscience and Nanotechnology*, 2010.

[50] Jan Prasek, Jana Drbohlavova, Jana Chomoucka, Jaromir Hubalek, Ondrej Jasek, Vojtech Adam, and Rene Kizek. Methods for carbon nanotubes synthesis—review. *Journal of Materials Chemistry*, 2011.

[51] Coskun Kocabas, Seong Jun Kang, Taner Ozel, Moonsub Shim, and John A. Rogers. Improved synthesis of aligned arrays of single-walled carbon nanotubes and their implementation in thin film type transistors. *Journal of Physical Chemistry*, 2007.

[52] Dongning Yuan, Lei Ding, Haibin Chu, Yiyu Feng, Thomas P. McNicholas, and Jie Liu. Horizontally aligned single-walled carbon nanotube on quartz from a large variety of metal catalysts. *NANO LETTERS*, 2008.

[53] MEC Quartz Crystal. Technical information. `http://www.mecquartz.com/html/info.html`. Version: 11-16-2016.

[54] Neha Arora and N.N. Sharma. Arc discharge synthesis of carbon nanotubes: Comprehensive review. *Diamond & Related Materials*, 2014.

[55] Justyna Chrzanowska, Jacek Hoffman, Artur Malolepszy, Marta Mazurkiewicz, Tomasz A. Kowalewski, Zygmunt Szymanski, , and Leszek Stobinski. Synthesis of carbon nanotubes by the laser ablation method: Effect of laser wavelength. *Physica Status Solidi B: Basic Solid State Physics*, 2015.

[56] Muhammad Musaddique, Ali Rafique, and Javed Iqbal. Production of carbon nanotubes by different routes — a review. *Journal of Encapsulation and Adsorption Sciences*, 2011.

[57] Weiwei Zhou, Christopher Rutherglen, and Peter J. Burke. Wafer scale synthesis of dense aligned arrays of single-walled carbon nanotubes. *Nano Res*, Vol. 1:p. 158–165, 2008. DOI: 10.1007/s12274-008-8012-9.

[58] Sigma Aldrich. *Single-Walled Carbon Nanotubes: Exfoliation and Debundling Procedure.*

[59] Kenro Mitsuda, Hiroshi Kimura, and Toshiaki Murahashi. Evaporation and decomposition of triton x-100 under various gases and temperatures. *Journal of material science*, Vol. 24:p. 413–419, 1989.

[60] Yumin Sim, June Park, Yu Jin Kim, Maeng-Je Seong, and Seunghun Hong. Synthesis of graphene layers using graphite dispersion in aqueous surfactant solutions. *Journal of the Korean physical society*, Vol. 58(No. 4):938–942, 2011.

[61] Nitish Nair, Monica L. Usrey, Woo-Jae Kim, Richard D. Braatz, and Michael S. Strano. Estimation of the (n,m) concentration distribution of single-walled carbon nanotubes from photoabsorption spectra. *Analytical Chemistry*, Vol. 78(No. 22):7689–7696, 2006.

[62] D. Krishnamurti. The raman spectrum of quartz and its interpretation. 1958. Memoir No. 108 from the Raman Research Institute communicated by Sir C. V. Raman.

[63] Kurt Lesker company. Safety data sheet iron oxide (fe2o3) pieces. Technical report.

[64] Aiqin Jiang, Neha Awasthi, Aleksey N. Kolmogorov, Wahyu Setyawan, Anders Börjesson, Kim Bolton, Avetik R. Harutyunyan, and Stefano Curtarolo. Theoretical study of the thermal behavior of free and alumina-supported fe-c nanoparticles. *PHYSICAL REVIEW B*, Vol. 75(No. 205426):p. 1–11, 2007. DOI: 10.1103/PhysRevB.75.205426.

[65] Anjam Khursheed. *Scanning electron microscope optics and spectrometers*. World scientific, 2011.

[66] Peter Eaton and Paul West. *Atomic force microscopy*. Oxford University Press, 2010.

[67] Robert J. Robson and Edward A. Dennls. The size, shape, and hydration of nonionic surfactant micelles. triton x-100. *The Journal of Physical Chemistry*, Vol. 8 1(No. 11):p. 1075–1078, 1977.

[68] Accuratus. Aluminum oxide, al2o3 ceramic properties. `http://accuratus.com/alumox.html`. Version: 14-06-2016.

[69] R. C. Ku and W. L. Winterbottom. Electrical conductivity in sputter-deposited chromium oxide coatings. *Thin Solid Films*, Vol. 127:p. 241–256, 1985.

[70] Shuangxi Xie, Niandong Jiao, Steve Tung, and Lianqing Liu. Fabrication of swcnt-graphene field-effect transistors. *Micromachines*, Vol. 6:p. 1317–1330, 2015. doi:10.3390/mi6091317.

[71] Rui Igreja and C.J. Dias. Analytical evaluation of the interdigital electrodes capacitance for a multi-layered structure. *Elsevier sensors and actuators*, Vol. 112:p. 291–301, 2004.

[72] John R. Reitz, Frederick J. Milford, and Robert W. Christy. *Foundations of Electromagnetic Theory*. Pearson, fourth edition edition, 2009.

Derivation of diffusion current

A

The ambipolar transport equation is stated in equation (A.2). Taking the steady-state case in the p-region, the equation can be simplified to a differential equation only in space, but with a homogeneous and a particular solution.

$$D_n \frac{\partial^2(\delta n_p)}{\partial x^2} + G_L - \frac{\delta n_p}{\tau_{n0}} = \frac{\partial(\delta_{np})}{\partial t} \tag{A.1}$$

Divided by D_n, this can be rearranged to:

$$\frac{\partial^2(\delta n_p)}{\partial x^2} - \frac{\delta n_p}{L_n^2} = -\frac{G_L}{D_n} \tag{A.2}$$

Where $L_n^2 = D_n \tau_{n0}$ is the diffusion length, but also a convenient notation. There is a lot of different symbols and most are well known, but to make it clear, they are recited below in short form: D_n=Diffusion constant for electrons, δn_p= Concentration of excess electron minority carriers in the p-region and τ_{n0}= Lifetime of electrons before recombination.

The homogeneous part of the differential equation is stated in equation (A.3) and has solutions of $\delta n_p = A\exp(-x/L_n) + B\exp(x/L_n)$. It is required that δn_p does not go to infinity and thus $B = 0$.

$$\frac{\partial^2(\delta n_{ph})}{\partial x^2} - \frac{\delta n_{ph}}{L_n^2} = 0 \tag{A.3}$$

The particular part is found from the constant terms as seen below.

$$\frac{\delta n_{pp}}{L_n^2} = -\frac{G_L}{D_n} \rightarrow \delta n_{pp} = G_L \tau_{n0} \tag{A.4}$$

Combining the two equations yields $\delta n_p = A\exp(-x/L_n) + G_L\tau_{n0}$. The electron concentration at the boundary to the p-region is zero when the junction is reversed biased. Due to the applied electric field shoving an excess amount of holes which recombine with the minority

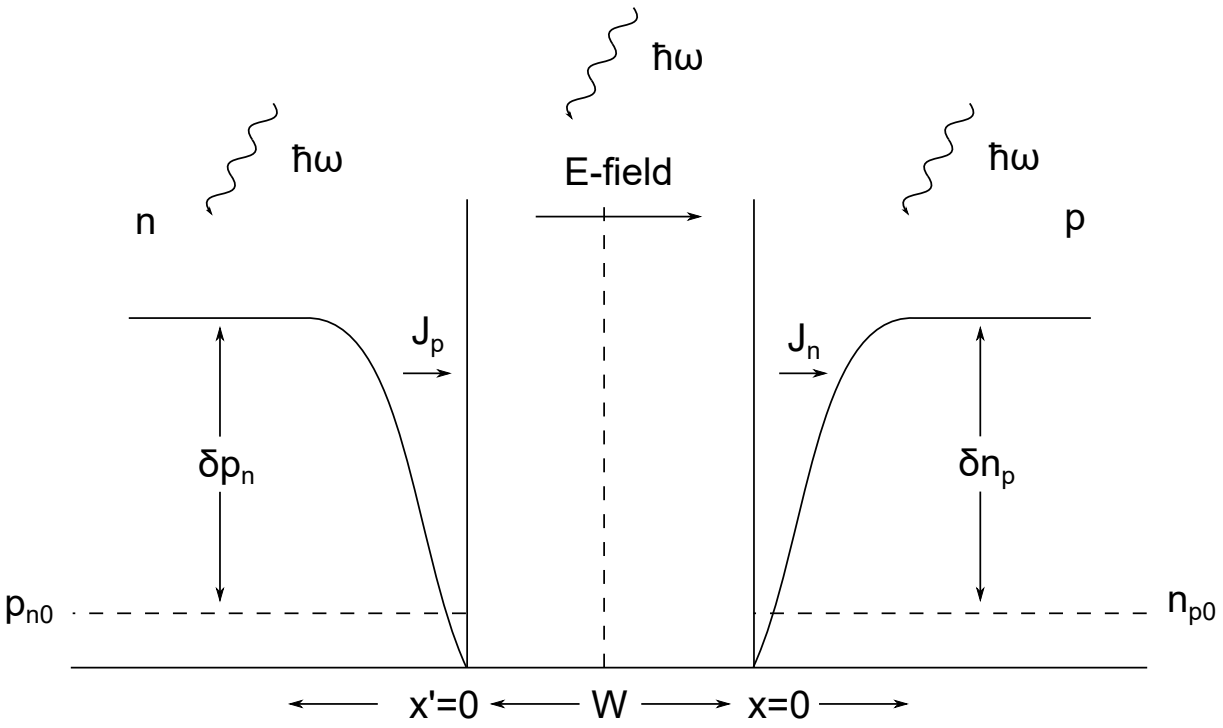

Figure A.1: *A p-n junction photodetector operated at reverse bias with spacecharge layer (W) and the density of excess minority carriers as a function of space up the vertical axis, shown for n and p region respectively.*

carrier electrons in the p-region (see figure A.1). This means the boundary condition that $\delta n_p(x = 0) = -n_{p0}$ must be valid. Thus the amount of excess electrons can be found from equation (A.5).

$$\delta n_p = G_l \tau_{n0} - (G_L \tau_{n0} + n_{p0}) \exp(-x/L_n) \tag{A.5}$$

Similarly the excess minority carrier concentration can be found in the n-region, which yields $\delta p_n = G_L \tau_{p0} - (G_L \tau_{p0} + p_{n0}) \exp(-x'/L_p)$, note that the x'-direction is opposite to the x-direction as seen on the figure A.1.

The current density for the steady state case of electrons at the interface can be found from inserting equation (A.5) into the ambipolar transport equation (A.2) yielding (A.6):

$$J_n = eD_n \frac{d(\delta n_p)}{dx} = eD_n \frac{d}{dx}[G_L \tau_{n0} - (G_L \tau_{n0} + n_{p0}) \exp(-x/L_n)] = \frac{eD_n}{L_n}(G_L \tau_{n0} + n_{p0}) \tag{A.6}$$

Which can be simplified to $J_n = eG_L L_n + eD_n n_{p0}/L_n$ for the p-region and $J_p = eG_L L_p + eD_p p_{n0}/L_p$ for the n-region. This is collectedly called the diffusion current, however the first term in each of the equation is the photocurrent density and the last term is the ideal reverse saturation current from the minority carriers.

The total photocurrent density is stated below, including the photocurrent from equation (3.8). Note that the reverse saturation currents are usually several orders of magnitude lower than the photocurrent.

$$J_L = eG_L W + eG_L L_n + eG_L L_p \tag{A.7}$$

The photocurrent in such a device is slow due to the fact that it stems from diffusion of minority carriers into the space charge layer. It is assumed that there is no tunnelling. Thus the equations only works for a relatively long photodiode, meaning that the doping is low to make the depletion width W long.

Derivation of thermionic emission theory

B

To find the current from the semiconductor to the metal, an integration over all electrons with velocities at or above the conduction band is done in equation (B.1). Assuming a Boltzmann distribution of electron velocities and all of the added energy will result in additional kinetic energy to the electron.

$$J_{sc\to m} = e\int_{-\infty}^{\infty} v_x \frac{dn}{dE}\, dE \tag{B.1}$$

The electron density in an energy interval is found from the density of states ($g_c(E)$) and the Fermi-Dirac function($f(E)$), as seen in equation (B.2).

$$\frac{dn}{dE} = g_c(E)f(E) = \frac{4\pi(2m^*)^{3/2}}{h^3}\sqrt{E-E_c}\exp\left(\frac{-E+E_F}{k_bT}\right) \tag{B.2}$$

Where m^* is the effective mass defined as $m^* = m_{eff}m_0$, e the elementary charge and k_bT the thermal energy. The identity between the energy and velocity is also needed, and is calculated in equation (B.3).

$$\sqrt{E-E_c} = v\sqrt{\frac{m^*}{2}} \tag{B.3}$$

The energy difference is the energy in addition to the conduction band. The resulting infinitesimal energy element is as seen equation (B.4).

$$dE = m^* v\, dv \tag{B.4}$$

Combining equations (B.2) and (B.4) results in equation (B.5). The E in the exponential function is split into E_c and the velocity term as seen in equation (B.3).

$$\frac{dn}{dE}dE = 2\left(\frac{m^*}{h}\right)^3 \exp\left(\frac{-E_c(x=\infty)+E_f}{k_bT}\right)\exp\left(\frac{-m^*v^2}{2k_bT}\right)4\pi v^2 dv \tag{B.5}$$

The next step is to put everything into the integral and replace $v^2 = v_x^2 + v_y^2 + v_z^2$ and the infinitesimal velocity element $4\pi v^2 dv = dv_x + dv_y + dv_z$. $4v^2\pi$ vanishes due to the Jacobian

determinant. This yields the integral seen in equation (B.6), where the two lines are multiplied together. Note that the integral is evaluated at the barrier interface and thus the value for $E_c(x=0)$ is needed.

$$\begin{aligned} J_{interface} =& 2\left(\frac{m^*}{h}\right)^3 \exp\left(\frac{-E_c(x=0)+E_f}{k_bT}\right) \int_{-\infty}^{\infty} \exp\left(\frac{-m^*v_y^2}{2k_bT}\right)\, dv_y \int_{-\infty}^{\infty} \exp\left(\frac{-m^*v_z^2}{2k_bT}\right)\, dv_z \\ & \int_{v_{min}}^{\infty} ev_x \exp\left(\frac{-m^*v_x^2}{2k_bT}\right)\, dv_x \\ =& 2e\left(\frac{m^*}{h}\right)^3 \left(\frac{2k_bT}{m^*}\right) \left(\frac{-E_c(x=0)+E_f}{k_bT}\right) \exp\left(\frac{-m^*v_{min}^2}{2k_bT}\right) \frac{k_bT}{m^*} \end{aligned} \tag{B.6}$$

Here v_{min} is the minimum velocity to pass the potential across the n-type region, $m^*v_{min}^2/2 = e\phi_n$. The current contributions from the velocities in the y and z directions will be equal as seen in equation (B.7), and the exponential function will be zero for the infinity limit, yielding no contribution from that.

$$\int_{-\infty}^{\infty} \exp\left(\frac{-m^*v_y^2}{2k_bT}\right)\, dv_y = \int_{-\infty}^{\infty} \exp\left(\frac{-m^*v_z^2}{2k_bT}\right)\, dv_z = \sqrt{\frac{2\pi k_bT}{m^*}} \tag{B.7}$$

The Richardson constant is a collection of constant terms in the equation, but is different with respect to the effective electron mass of the specific semiconductor, stated below in equation (B.8).

$$A^* = \frac{4\pi m^* k_b}{h^3} \tag{B.8}$$

Now taking $\phi_n = \phi_i - V_a = \phi_b + (E_c(x=\infty) - E_F)/e - V_a$, the current from the metal to the semiconductor can be written as in equation (B.9).

$$J = A^*T^2 \exp\left(\frac{-\phi_b}{k_bT}\right) \left[exp\left(\frac{V_a}{k_bT}\right) - 1\right] \tag{B.9}$$

This equation is similar to the standard diode equation and varies exponentially with the applied voltage and the height of the Schottky barrier. The -1 term is added for the current flowing in the other direction than the applied bias. Doing the same calculations again, but setting $V_a = 0$, will still be dependent on the barrier height and yield a -1 to make sure the current goes to zero when there is no applied bias, assuming that the effective mass does not change over the barrier.

Additional current-voltage data

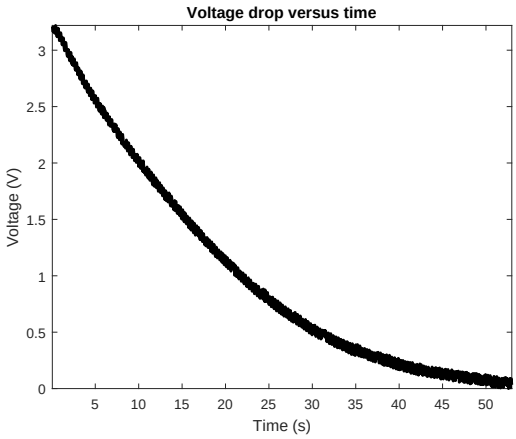

FIGURE C.1: *20 μm separation, aluminium. Disharge after 200 nA.*

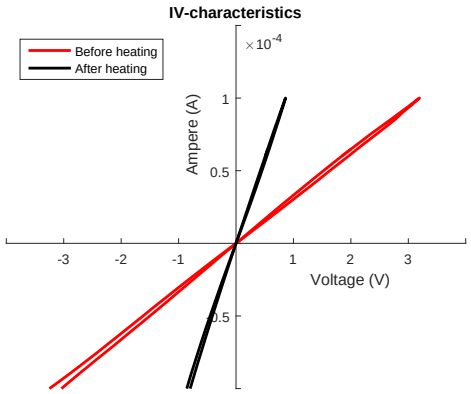

FIGURE C.2: *20 μm separation on aluminium, before and after heating.*

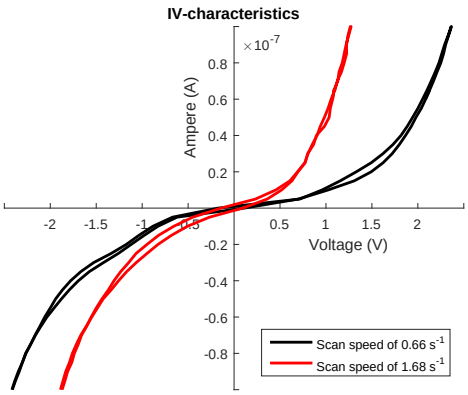

FIGURE C.3: *15 μm separation on chrome. 100 nA maximum current.*

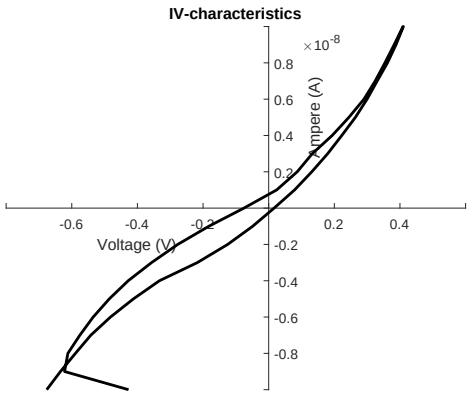

FIGURE C.4: *20 μm separation on chrome. 10 nA maximum current*

Schottky barrier height from current-voltage curve

D

Several methods exist to find the height of a Schottky barrier, where many of them require some theoretical modelling to fit certain parameters and advanced measuring equipment. However a few method involves only the current-voltage curve.

First method

Assuming all the current going though is thermionic current and thus no tunnelling current, which is a good approximation for Schottky barriers with a wide depletion region, the equation for thermionic current can be used. This is seen in equation (3.6). The equation can be modified to give equation (D.1). If voltage is set to zero, and the electrical area, temperature and the Richardson constant are known, the barrier height can be found. Knowing the exact electrical area is very difficult however, and thus this is not a very accurate technique.

$$\phi_B = -\frac{\log[\frac{I_{dark}/area}{T^2 A^*(1-\exp(-qV_a/k_BT))}]}{k_BT} \tag{D.1}$$

Second method

The second method involves the same approximations as the earlier one, but involves an Arhenius plot to find the barrier. The saturation current can be written as in equation (D.2) by again modifying the equation for thermionic current, where the voltage is again set as zero.

$$\log(\frac{I_{Sat}}{T^2}) = \log(areaA^*) - \frac{q\phi_B}{k_BT} \tag{D.2}$$

By plotting $\log(I_{sat}/T^2)$ up the y-axis and $1/T$ on the x-axis while measuring I_{sat} at different temperatures, an Arhenius plot can be made. At the intersection with the y-axis or at $T \to \infty$, $\log(areaA^*)$ can be found and thus this technique does not require the knowledge of the electrical area or the Richardson constant. The slope of the curve on the Arhenius plot is then equal to $-q\phi_B/k_B$. The difficulty of this technique is to measure at enough temperatures to get the exact curve of the Arhenius plot.

Capacitance

E

For this thesis two different methods have been used to determine the capacitance of the samples described in section 6.3.

The first method

The four point probe system previously described, is used to put a constant current through the sample for eg. 60 seconds. After this it is turned off while the voltage is measured. A build-up of voltage can be seen in the first seconds and then a voltage drop is seen when the current is turned off. As the equipment needs to stabilise, the discharge has been used to determine the capacitance from equation (E.1). [72]

$$V(t) = V_0 \exp(-\frac{t}{RC}) \tag{E.1}$$

Where R is the resistance, t the time, V the voltage and C the capacitance. Specifically once the resistance is known, the capacitance is found by taking an exponential fit. The coefficient inside the exponent is then divided by the resistance.

The second method

The second method uses the IV-curves along with a timer to determine the capacitance. This method is known as cyclic voltametry by physical chemists. By changing the scanning speed, a difference in hysteresis can be seen on the curves. The idea is to calculate the capacitance with a different method to verify the first result. The formula can be seen in equation (E.2). The technique with withdrawing the two measurements from each other is that the capacitance is dependent on scan speed and direction of the bias voltage while the resistance is not. Numerical differentiation is used to calculate dV/dt and the current is interpolated at specific voltages that correspond with dV/dt. [72]

$$C = \frac{I_a - I_b}{\frac{dV_a}{dt} - \frac{dV_b}{dt}} \tag{E.2}$$